STUDY OF ULTRAFAST HOT-ELECTRON DYNAMICS IN SILICON USING TIME-RESOLVED PHOTOEMISSION

by

Seongtae Jeong

Memorandum No. UCB/ERL M97/94

18 December 1997

STUDY OF ULTRAFAST HOT-ELECTRON DYNAMICS IN SILICON USING TIME-RESOLVED PHOTOEMISSION

by

Seongtae Jeong

Memorandum No. UCB/ERL M97/94

18 December 1997

ELECTRONICS RESEARCH LABORATORY

College of Engineering
University of California, Berkeley
94720

Abstract

Study of Ultrafast Hot-Electron Dynamics in Silicon
using Time-resolved Photoemission

by

Seongtae Jeong

Doctor of Philosophy in Physics

University of California, Berkeley

Professor Jeffrey Bokor, Co-chair

Professor Daniel S. Chemla, Co-chair

A direct time domain study of hot electron dynamics on the Si(100)2x1 surface is performed using time-resolved two photon photoemission based on a pulsed Ti:sapphire laser system. Experimental issues such as the third harmonic generation and space charge broadening are carefully evaluated. Experimental results on various clean silicon samples are presented. The method to determine the position of the band edge states using multiphoton photoemission spectrum is discussed. The nature of the observed states is investigated by varying doping concentration, surface domain structure and sample temperature.

The electron population near the surface and the shape of the electron energy distribution are found to change on a very fast time scale. A nonthermal distribution is observed near T = 0.0 psec and its subsequent thermalization toward a Maxwell-Boltzmann distribution is observed. As a quantitative measure of the electron energy distribution, the electron temperature is extracted. The electron temperature changes on a

time scale of 0.4 psec and it also depends on the pump beam fluence. A theoretical model incorporating two-photon absorption is set-up to extract carrier transport parameters.

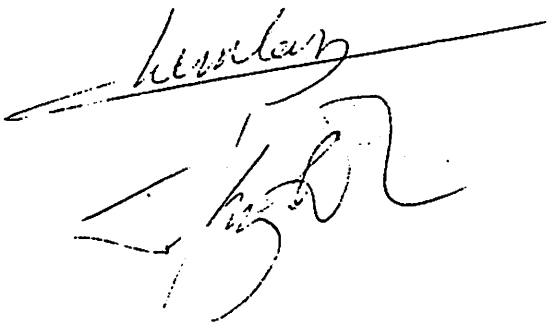

Table of Contents

Chapter 1. Introduction

Chapter 2. Experimental Set-up

2.1 Lasers and optics system

2.2 Vacuum chamber

2.3 Electron spectrometer

2.4 Sample preparation

Chapter 3. Harmonic generation and Space charge effect

3.1 Harmonic generator

3.2 Space charge effect

Chapter 4. Experimental Results

4.1 Ultrafast carrier energy relaxation processes in silicon after pulsed laser excitation

4.2 Studies of the Si(100) surface electronic structure

4.3 Position of the bulk band edge.

4.4 Pump-and-probe time-resolved spectrum

4.5 Spectrum from a single domain Si surface

4.6 Spectrum from a heavily doped n-type sample

4.7 Substrate temperature dependence

4.8 Electron temperature

4.9 Various pump beam intensity spectrum

4.10 Theoretical model

Chapter 5. Conclusion

References

Appendix

A.1 Estimate of the front surface temperature due to the accumulation of the heat

A.2. Calculation of the potential energy of an electron cloud of a thin-disk shape

List of Figures

Fig. 2-1 Laser system schematic

Fig. 2-2 Optics layout before the vacuum chamber

Fig. 2-3 Timing between the pump and probe by cross-correlation

Fig. 2-4 Schematic of the vacuum system. (a) Top View (b) Side View

Fig. 2-5 Electron detector schematic

Fig. 2-6 Schematic of the timing electronics

Fig. 2-7 Sample time-of-flight spectrum

Fig. 2-8 Photon peak spread

Fig. 3-1 Schematic of the harmonic generator

Fig. 3-2 (a) The second harmonic beam and the fundamental beam at the end of the crystal.

(b) The input pulse at the start of the crystal.

Fig. 3-3 Integrated energy of the third harmonic beam as a function of the temporal separation between the fundamental beam and the second harmonic beam at the entrance of the crystal.

Fig. 3-4 Spatial and kinetic energy distribution of electrons at the start of the simulation.

Fig. 3-5 Spatial and kinetic energy distribution of electrons at the end of the simulation

Fig. 4-1 Surface reconstruction of the Si(100) surface

Fig. 4-2 Surface Brillouin zone of the Si(100)2x1 surface

Fig. 4-3 Step structure of the Si(100) surface

Fig. 4-4 Kinetic energy of photoemitted electrons

Fig. 4-5 Probe only spectra

Fig. 4-6 Time-resolved spectra

Fig. 4-7 Difference Spectra

Fig. 4-8 Bulk bandstructure of silicon

Fig. 4-9 Yield vs time delay

Fig. 4-10 Symmetry property in photoemission

Fig. 4-11 (a) Spectra with 266 nm only from n+ sample with two different laser intensity

(b) Optimum exponent at each energy position

Fig. 4-12 (a) One photon photoemission coefficient

(b) two photon photoemission coefficient

Fig. 4-13 Time-resolved spectra from n+ sample.

Fig. 4-14 Spectrum at two different temperature

Fig. 4-15 Magnitude of the two-color signal

Fig. 4-16 Electronic distribution function above the conduction band minimum

Fig. 4-17 Electron temperature as a function of delay time.

Fig. 4-18 (a) Electron distribution at T = 0.0 psec with four different pump fluence

(b) Optimum exponent at each energy position

Fig. 4-19 Electron temperature at different pump fluence

Fig. 4-20 Calculated electron temperature

List of Tables

Table 2-1 Sample specifications

Table 3-1 Indices of refraction of BBO crystals at 800, 400, 266 and 200 nm

Table 3-2 Indices of refraction and group velocities of 800, 400 and 266 nm

Table 3-3 Change in the electronic kinetic energy distribution as a function of the radius of the electron cloud.

Acknowledgments

By the time I have finished this thesis, I realized that I have so many people to thank for their contributions. First, I would like to express my deepest thankfulness to my advisor, Professor Jeffrey Bokor for his academic, financial and moral support throughout my graduate study at Berkeley. This thesis would not be possible without his technical help and guidance. I also would like to appreciate the great collaboration with Professor Helmut Zacharias at University of Münster, Germany. It was such a good experience to have an opportunity to work with him and learn from him for six months. I cannot say enough words of gratitude to my colleagues in the laboratory: Dr. Edward Budiarto and Dr. Joo-hiuk Son. I also would like to thank the sponsor of my thesis project, Joint Servies Electronics Program which sponsored this project for more than three years.

I also would like to appreciate contributions from a great number of people both in Korea and in America. First, I would like to thank for my mother, Oksun Ahn, my sisters, Miyoung Jeong and Sunyoung Jeong, and my wife Kyongha Lee for their moral support. I also would like to mention the name of my father, Kapjin Jeong who died seventeen years ago. Encouragement from Mr. Sung-hwan Han, Woi-sun Lee, my high school teacher Byong-do Seo and my cousin Hyoung-Im Jeong are greatly appreciated. Financial supports from Korea Foundation for Advanced Studies, Hanmaeum Foundation and Hakwon Foundation have been essential to my higher education. Finally, by mentioning their names I would like to thank all of the people who made my graduate life more pleasant and endurable: Therese Schroeder, Dr. Doseok Kim, Wonran Cho, Dr. Hyun-Joon Shin, and Dr. Chul-Hyun Kim.

Chapter 1. Introduction

The study of carrier transport properties of semiconductors and their heterostructures is an important area of research since they are the key parameters in understanding the performance of microelectronic devices. Because silicon has been the material of choice for large-scale integrated electronic devices for the past three decades, the transport properties of silicon have been studied by various methods. When the carrier energy distribution is not far from equilibrium with the lattice, the carrier energy distribution can be reasonably represented by a Maxwell-Boltzmann distribution and the carrier transport can be described by a set of coupled linear differential equations containing macroscopic material parameters such as mobility and diffusion coefficient (drift-diffusion equations). For most of the conventional electronic devices, the drift-diffusion equation approach is valid and experimental studies of transport parameters have been performed through dc transport measurements such as I-V characteristics of a device.

When the carrier energy distribution is displaced far from equilibrium due to a strong temporal or spatial transient of the electric field or due to the ultrafast generation of carriers with ultrafast pulsed laser illumination, the situation changes significantly. The electron energy distribution is characterized by electron temperatures much higher than that of the lattice and sometimes it cannot be described by a Maxwell-Boltzmann distribution. Under these conditions, there is a new class of physical phenomena associated with high-temperature electrons or nonthermalized electrons, which is referred

to as "hot electron phenomena" [1]. These hot electron phenomena should be taken into account for a proper understanding of modern electronic devices [2]. For example, as the channel length of the metal-oxide-semiconductor field effect transistor (MOSFET) is scaled to an ever-smaller dimension and its operating speed becomes faster, the electric field inside the channel becomes higher and its spatial or temporal gradient becomes more severe and complicated. Electrons in the channel do not have enough time to lose their energy to the lattice when the channel length is comparable to the electron-phonon mean free path. The carrier energy distribution inside the channel might not be in equilibrium with the lattice at room temperature. Well-known examples of hot electron phenomena are the threshold voltage shift and hot electron induced interface states [3]. When the carrier energy distribution inside the channel of a MOSFET is hot or nonthermal, the high kinetic energy electrons can surmount the Si-SiO_2 interface barrier and can be injected into the oxide. These electrons can be trapped inside the oxide, creating an oxide damage or they can be collected as part of the gate current. Some of the energetic electrons can induce damages in the Si-SiO_2 interface by creating silicon dangling bonds after breaking some of the weak Si-H bonds at the interface. This is particularly severe around the drain region of a device where the electric field is greatest. The consequence of these phenomena are the change in the threshold voltage of the device and an increased interface scattering that leads to a lower mobility. They are important device reliability and performance issues. To incorporate hot electron phenomena properly into a device simulation, a microscopic understanding of energy relaxation of the carriers and the carrier energy distribution inside the device is essential.

Another area for which hot electron dynamics research can help to provide vital pieces of information is the study of ultrafast surface chemistry occurring on semiconductor surfaces. The desorption of molecular species due to the presence of hot carriers was experimentally demonstrated on metals by several groups [4], [5]. Also a theoretical framework based on the model called "*D*esorption *I*nduced *M*ultiple *E*lectronic *T*ransitions (DIMET)" has been developed. In this model, a hot electron energy distribution is established inside the solid by an intense ultrafast laser pulse. Through the energy transfer from hot electrons to a foreign atom on the solid surface, the foreign atom undergoes multiple electronic transitions, converting the electronic energy into an atomic vibration. When the vibrational energy is greater than the dissociation energy of the adsorbate, the foreign atom is desorbed from the solid surface. Trappe *et al.*[6] showed that hot-electron induced desorption is also possible on semiconductor surfaces. They used time-of-flight mass spectroscopy and optical postionization technique to detect neutral atoms desorbed from a GaAs surface after excitation with 17 psec, 266 nm laser pulses. The maximum substrate temperature was estimated to be 1000 K, well below the melting threshold of GaAs. The desorption yield showed a nonlinear dependence on the laser fluence, which is expected for a DIMET process. Tien [7] *et al.* presented experimental evidence that hot electron induced desorption plays an important role in the stiction reduction of microelectromechanical systems irradiated with ultrashort laser pulses. Because hot electron induced desorption involves multiple electronic transitions whose probability depends nonlinearly on the number of high kinetic energy carriers, the knowledge of the carrier energy distribution and its evolution inside the

material on an ultrashort time scale plays a key role in understanding the microscopic mechanism of the desorption process.

The necessity of studying the evolution of the carrier energy distribution calls for a direct time domain study of the carrier energy distribution and carrier energy relaxation process, while conventional dc transport measurements usually probe the moments of the carrier energy distribution inside the solid. Because most of the carrier energy relaxation processes, for example, electron-phonon scattering, occur on a subpicosecond time scale, conventional electronic measurements do not have enough bandwidth to track down these fast events in real time. Fortunately, the advent of ultrafast lasers has allowed various ultrafast processes in condensed matter systems to be studied on time scales as short as a few femtoseconds. Most of the ultrafast phenomena studies are based on the technique referred to as "pump-and-probe spectroscopy." In this technique, a relatively intense pulsed laser beam (pump) irradiates the sample under investigation and another laser pulse probes the changes induced by the pump beam. It can be considered as an optical sampling technique to detect very fast phenomena using a slow detector. Various experimental schemes based on the pump-and-probe technique have been applied to the studies of the carrier dynamics in III-V semiconductors such as GaAs and their heterostructures [8]. In contrast, the direct time domain study of the ultrafast carrier dynamics in silicon has been far less active than that of III-V compound semiconductors. This is because silicon is an indirect bandgap material. In an indirect bandgap material such as silicon, the fundamental optical transition involves phonon for crystal momentum conservation. The momentum conserving phonon makes it hard to

interpret experimental results of conventional ultrafast optical pump-and-probe techniques such as transient reflectivity and transient transmission.

Time-resolved multiphoton photoemission spectroscopy has a potential to become a particularly effective tool in overcoming the difficulty related to the momentum-conserving phonons. Using photoemission spectroscopy, one can probe the electronic energy distribution inside the sample more directly than any other technique. Therefore, there is little ambiguity in identifying the energy position of the initial states. Furthermore, the angle-resolved detection capability of photoemission spectroscopy can be used to probe different parts of the Brillouin zone [9].The photoemission is also surface-sensitive because of the short inelastic mean free path of electrons at low kinetic energy [10] (~ 5 nm at 5 eV) and because of the short absorption depth of the UV light [11] (5 nm at 4.66 eV). The surface sensitivity of photoemission spectroscopy can be a valuable tool for studying physics or carrier dynamics near the surface where the presence of the bandgap states plays an important role [12]. However, the surface sensitivity can present experimental difficulties when the probing of bulk properties is desired. Because the photoemission spectrum is affected by surface preparation methods and surface cleanliness on an atomic scale, careful effort is needed for sample preparation and the experiment has to be carried out in an ultrahigh vacuum environment.

Despite these difficulties, there are quite a few studies of ultrafast carrier dynamics in silicon using multiphoton photoemission spectroscopy with various pulsed laser systems. Experiments that measured the photoelectric current as a function of the laser intensity showed that the electronic temperatures can be well above the lattice

temperature for nanosecond pulse excitations [13]. Leung and van Driel [14] used harmonics of a 25 nsec 1.06 micron laser beam to show that the thermionic emission process dominates at longer wavelength (1.06 , 0.53 micron) illumination and the multiphoton photoemission dominates at shorter wavelength (0.35 , 0.267 micron) illumination. In their study, Richardson-Dushman equation for thermionic emission was applied to extract the electron temperature, and it was shown that the electron temperature is several hundred degrees higher than the lattice temperature even with nanosecond laser pulse illumination. Long *et al.* [15] studied the photoemitted electronic energy distribution from a clean Si(111) surface with laser beams of 2.33 eV or 4.66 eV photon energy with temporal durations of tens of nanoseconds. The study on a Si(111)2x1 surface performed by Halas *et al.*[16] showed that the dynamic surface charging plays an important role in the carrier dynamics near the surface. A comprehensive study on various silicon surfaces by Rowe *et al.*[17] showed that the electron energy relaxation inside the surface band occurs on a time scale shorter than 3 psec, which was their laser pulsewidth-limited temporal resolution. The study performed by Goldman *et al.* with a 4 eV probe and a 2 eV pump beam showed that the electron temperature inside the conduction band changes from 1500 K to 800 K in less than 60 fsec after an optical excitation [18].

A brief mention has to be made about alternative optical methods to study ultrafast carrier dynamics in silicon. Since early 1980's, the transient reflectivity technique has been used to study melting and recrystallization of silicon crystal lattice after an intense femtosecond laser pulse excitation. Shank [19] showed that above the melting

threshold of the crystalline silicon, melting can be quite well explained by a thermal model in which the energy of the electron-hole plasma is transferred to the lattice, causing melting of the surface layer. Also the surface second harmonic generation has been successful to probe the surface electron dynamics on silicon surfaces [20], [21]. Because the second harmonic generation technique probes the change in the transition probability due to the change in the electronic distribution function, it gives useful insights into the ultrafast carrier dynamics on the surface. In their time-resolved second harmonic study on a Si(111)7x7 surface, Mauerer *et al* [21] showed that the electrons excited into the metallic surface band relax on a time scale of 1 psec.

It is noteworthy that multiphoton photoemission spectroscopy has also been successfully applied to a variety of metals [22] and as well as semiconductors such as Ge[23], GaAs [24], InP [9]. The image potential states close to the metal surface have been successfully studied [25] and the lifetime of the excitation near the Fermi level of a metal has been measured and compared with the Fermi liquid theory [26].

In this thesis, the ultrafast carrier dynamics on a silicon surface are studied on a subpicosecond time scale using time-resolved two photon photoemission spectroscopy. In chapter 2, a detailed description of the experimental set-up is given ; lasers, optics, vacuum chamber, electron spectrometer and timing electronics. Working principles and operational procedures of each of the major experimental components are presented. Chapter 3 deals with experimental concerns which are common to time-resolved photoemission spectroscopy using a visible pump and an ultraviolet probe. Presented is the design of the harmonic generator for generating harmonic beams of the input laser

beam through a nonlinear process with high efficiency while minimizing the pulse broadening. The space charge broadening of the energy spectrum of the photoemitted electrons is reviewed and a criteria for assessing its significance on the experimental data is presented from a simple electrostatic argument. In chapter 4, the actual experimental data are presented. The technique to identify the band edge states is discussed. The time-resolved spectra are presented and the nature of the states observed in the experiments is identified. Various processes involving linear optical absorption, nonlinear optical absorption, surface recombination and a coupling between the surface state and the bulk states are shown to coexist on an ultrafast time scale. It is shown how the carrier distribution evolves from the initial nonthermal distribution to a thermal distribution. The fluence dependence of the electron energy distribution is discussed. A theoretical attempt is made to extract useful dynamical parameters such as the electron energy relaxation time.

Chapter 2. Experimental Set-up

In this chapter, the experimental set-up is reviewed. The experimental set-up consists of the laser system, optics, vacuum chamber and data acquisition electronics. The working principles of the laser system are briefly reviewed and the optics layout for transporting the beam to the sample in a vacuum chamber is described in detail. The maintenance and operational procedures are described for the vacuum chamber and its accessory equipment such as the electron spectrometer. The description of the timing electronics is followed by the preparation method of the sample for an actual experiment.

2.1 Lasers and optics system.

The laser system used in the experiment is a commercial Ti:sapphire regenerative amplifier system based on chirped-pulse amplification (CPA-1000 from Clark MXR, Inc.) [27], [28]. The schematic of the laser system is shown in Fig 2.1. The Ti:sapphire oscillator (Clark-MXR ,NJA-4) is pumped by an argon ion laser (Spectra-Physics Beamlok 2060) with a pumping power of 4.5 W. The self-modelocked oscillator[29] output consists of trains of sub-100 fsec optical pulses at of 800 nm. Successive pulses are 10 nsec apart from one another. The average output of the oscillator is 300 mW in a modelocked operation, which corresponds to a pulse energy of 3 nJ per pulse. The oscillator pulses are fed into the pulse stretcher (Clark-MXR, PS-1000). Through the stretcher, each of the individual pulses is given a linear temporal chirp and it is stretched to a pulse longer than 100 psec by a combination of a grating and

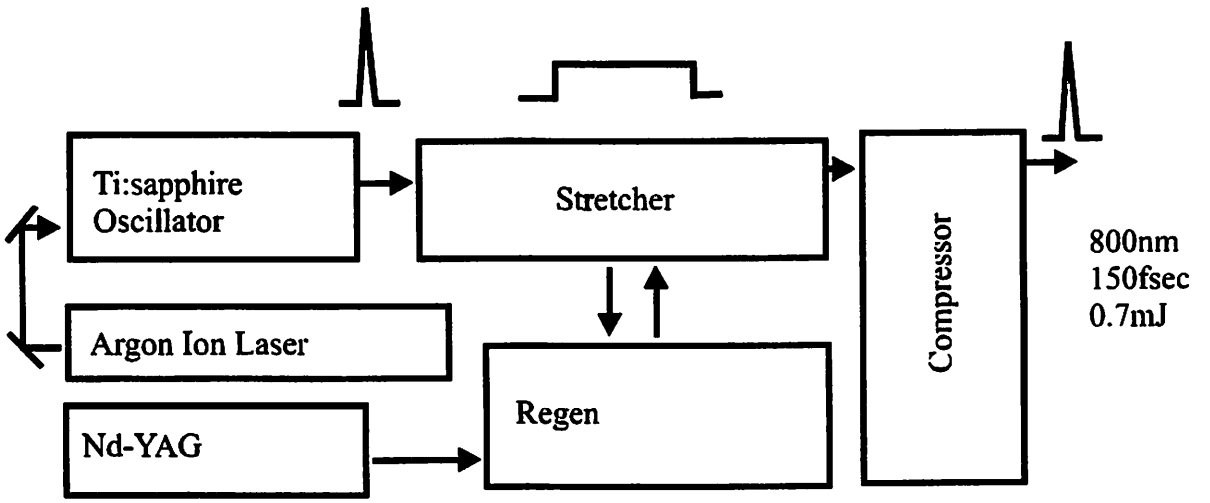

Fig 2-1. Laser system schematic

reflectors. The temporal stretching by a linear chirp constitutes the core technique of the chirped pulse amplification. It is essential to avoid any pulse distortion due to the intensity dependent nonlinear refractive index of the lasing medium in the amplifier or optical damage due to the high peak power of an optical pulse. After passing through the stretcher, optical pulses are injected into the regenerative amplifier. The regenerative amplifier is pumped by a frequency doubled Q-switched Nd:YAG laser (Clark-MXR, ORC-1000) operating with 8 W average power at 532 nm. Inside the regenerative amplifier, one out of every 100,000 pulses is picked up by the Pockels cell (Clark-MXR, TRA-1000). The stretched pulse picked up by the Pockels cell gains energy inside the amplifier through approximately 20 round trips. When the energy of the amplified pulse reaches its maximum, the high voltage applied at the Pockels cell is switched off and the amplified pulse is ejected out of the amplifier. At this point, the amplified pulse energy is more than 1 mJ and the pulsewidth is longer than 100 psec. The amplified pulses are spaced 1 msec apart from each other. All the timings such as the firing of the Q-switched Nd:YAG laser and switching of the Pockels cell are derived from the pulse train of the oscillator through a separate timing electronics module (Clark-MXR, DT-505). The stretched amplified pulse is compressed to a femtosecond pulse through a separate compressor (Clark-MXR, PC-1000). The compressor has overall efficiency of greater than 60 %. At the exit of the compressor, the final laser pulse has pulse energy greater than 0.5 mJ and the Full Width Half Maximum (FWHM) pulsewidth of 150 fsec can be achieved with a reasonable effort. The FWHM bandwidth of the pulse is typically 10 nm. The pulsewidth and spectral characteristics of the pulse are monitored using a home-built

Frequency-Resolved-Optical-Gating (FROG) [30] instrument in combination with a noncollinear second harmonic generation autocorrelator [31]. The retroreflector inside the compressor is translated to achieve the optimum pulsewidth and pulse shape.

The laser beam is transported to the experimental station using various optical components. The schematic of the optics layout is presented in Fig 2.2. It is based on a pump-and-probe scheme. A telescope comprised of two convex lenses is used to reduce the beam size by approximately three times to avoid the beam clipping by any of the downstream optics and to achieve reasonable conversion efficiency in the harmonic generator. A part of the optical beam scattered off the telescope lenses is detected by a fast photodiode (HP 5082-4220) biased to generate a fast negative pulse to be used as a trigger pulse in the data acquisition electronics which is discussed in subsection 2.3. A 50/50 beam splitter (BS1) splits the optical pulse into two pulses of equal energy. One pulse referred to as "pump beam" travels through the stepper motor-driven optical delay line with 1 micron step resolution and eventually it is delivered to the sample inside a vacuum chamber. The polarization of the pump beam can be varied by rotating the half waveplate (WP3) and its intensity can be varied by using a half waveplate (WP2) and a thin-film polarizer (POL) combination as shown in Fig 2.2. The second pulse is used to generate the third harmonic pulse (266 nm) through the harmonic generator. The generation of the third harmonic beam is explained in more detail in the section 3.1. The 266 nm pulse is called a "probe beam." The energy of the probe beam is less than 1 μJ and it can be varied by rotating the polarization of the seed pulse using a half waveplate (WP1) before the third harmonic generator. The overall third harmonic conversion efficiency is less than 1 %. However, the third harmonic intensity is more than

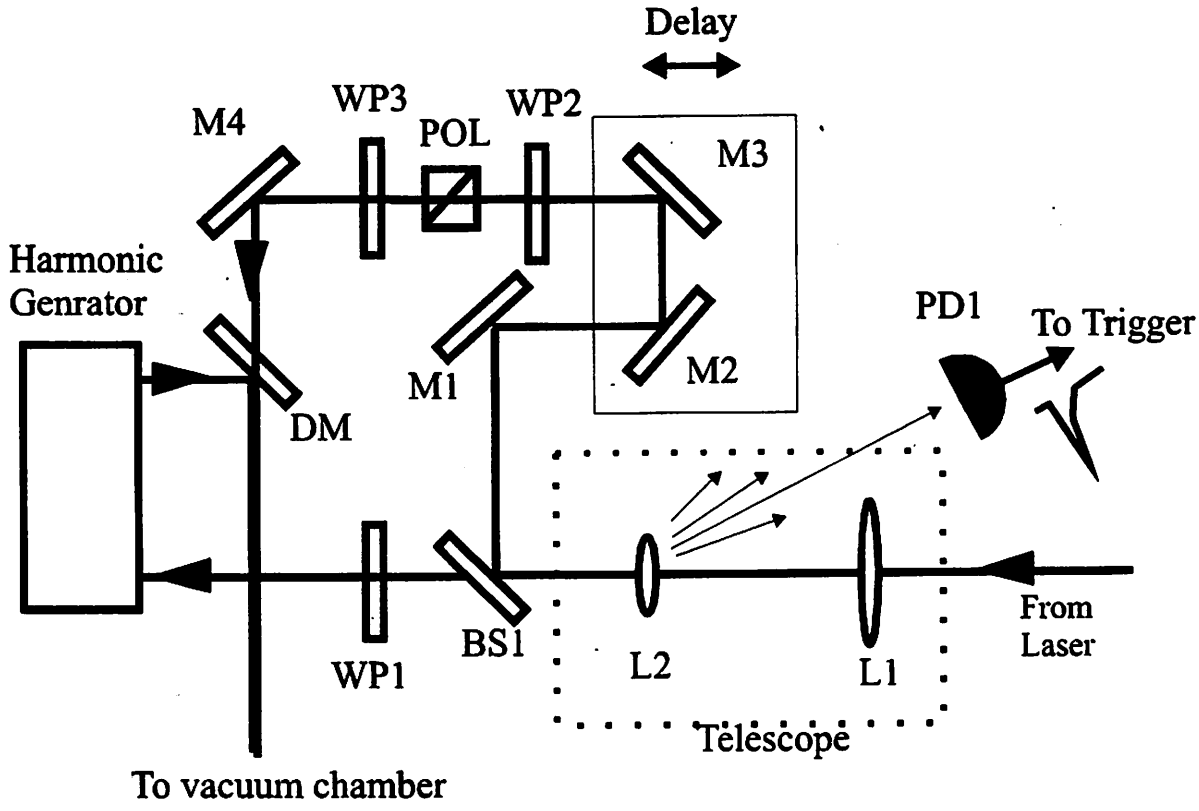

Fig 2-2. Optics layout before the vacuum chamber

enough for the experiments under discussion and no attempt is made to achieve the highest conversion efficiency possible. The probe pulse (266 nm) and pump pulse (800 nm) are aligned to travel collinearly toward the sample inside the vacuum chamber using a dichroic mirror (DM).

The synchronization between the pump pulse and the probe pulse is achieved by mixing the two beams inside a $\beta - BaB_2O_4$ (BBO) crystal. It is cut 72 degrees for type I phase matching between the two beams to generate a 200 nm beam, as shown in Fig. 2-3. When the pump beam and the probe beam travel through a 1/4 inch thick quartz window of the vacuum chamber, the group velocity dispersion of the window at 800 nm and 266 nm introduces an additional time delay of approximately 2 psec between the pump beam and the probe beam. It can be compensated by giving an additional time delay to the pump beam. The time delay due to the group velocity dispersion is determined by putting a vacuum window of the same kind with the same thickness in front of the mixing crystal (NX). After two beams passing through the nonlinear crystal (NX), the three beams (800 nm, 266 nm, and 200 nm) are spatially separated by a quartz prism followed by a dichroic mirror. The probe beam pulsewidth can be estimated by measuring the fourth harmonic beam intensity as a function of the delay between the pump beam and probe beam (cross-correlation).

The stepper motor controller (CC.1.2, Newport) that adjusts the optical delay for the pump beam is controlled through a serial port of a computer. The software which controls the stepper motor controller is integrated with the data acquisition software (EG&G, Maestro for Windows), and the data acquisition process is completely automated. The automation of the data acquisition and control of the delay stage is an

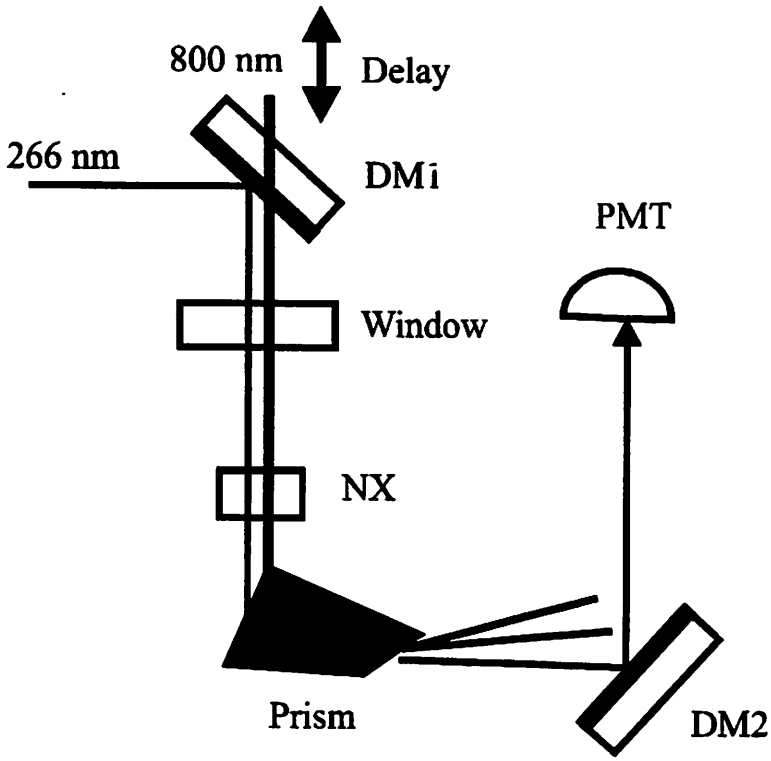

Fig 2-3. Timing between the pump beam and probe beam by cross-correlation

DM1, DM2 : dichroic mirror, NX : nonlinear crystal, PMT : Photomultiplier tube

integral element of the data acquisition system. It enables fast data acquisition, which is important for achieving higher signal to noise ratio.

2.2 Vacuum chamber

The vacuum chamber schematic is shown in Fig 2-4. It's a stainless steel chamber and the inner wall of the chamber is lined with sheets of the mu metal shield to shield out stray magnetic field and earth's magnetic field. The chamber consists of two compartments: the upper compartment and the lower compartment. The upper compartment houses a Low-Energy-Electron-Diffraction (LEED) spectrometer, a time-of-flight electron energy spectrometer, a quadrupole mass spectrometer, an argon ion sputter gun and the sample manipulator. The lower compartment houses a titanium sublimation pump and an ion pump. The two compartments can be isolated by closing a gate valve between them. A metallic isolation valve connects the upper compartment to a turbomolecular pump backed by a mechanical pump. When exposure to an atmospheric pressure is necessary for service or replacement of the sample, the lower compartment is isolated by closing the gate valve and it is maintained in an ultrahigh vacuum condition with the ion pump. The upper compartment is filled with flowing dry nitrogen to minimize water adsorption on the chamber wall. It helps to reduce the pump-down time. When the chamber is ready for the pump-down, the pressure of the upper compartment is reduced by a turbomolecular pump to a pressure range of high 10^{-6} Torr. After reaching the pressure range of high 10^{-6} Torr, the chamber is isolated from the turbomolecular pump by closing the metallic valve and the gate valve is opened to pump down the upper compartment using the ion pump. Before moving to the next step of pumping down,

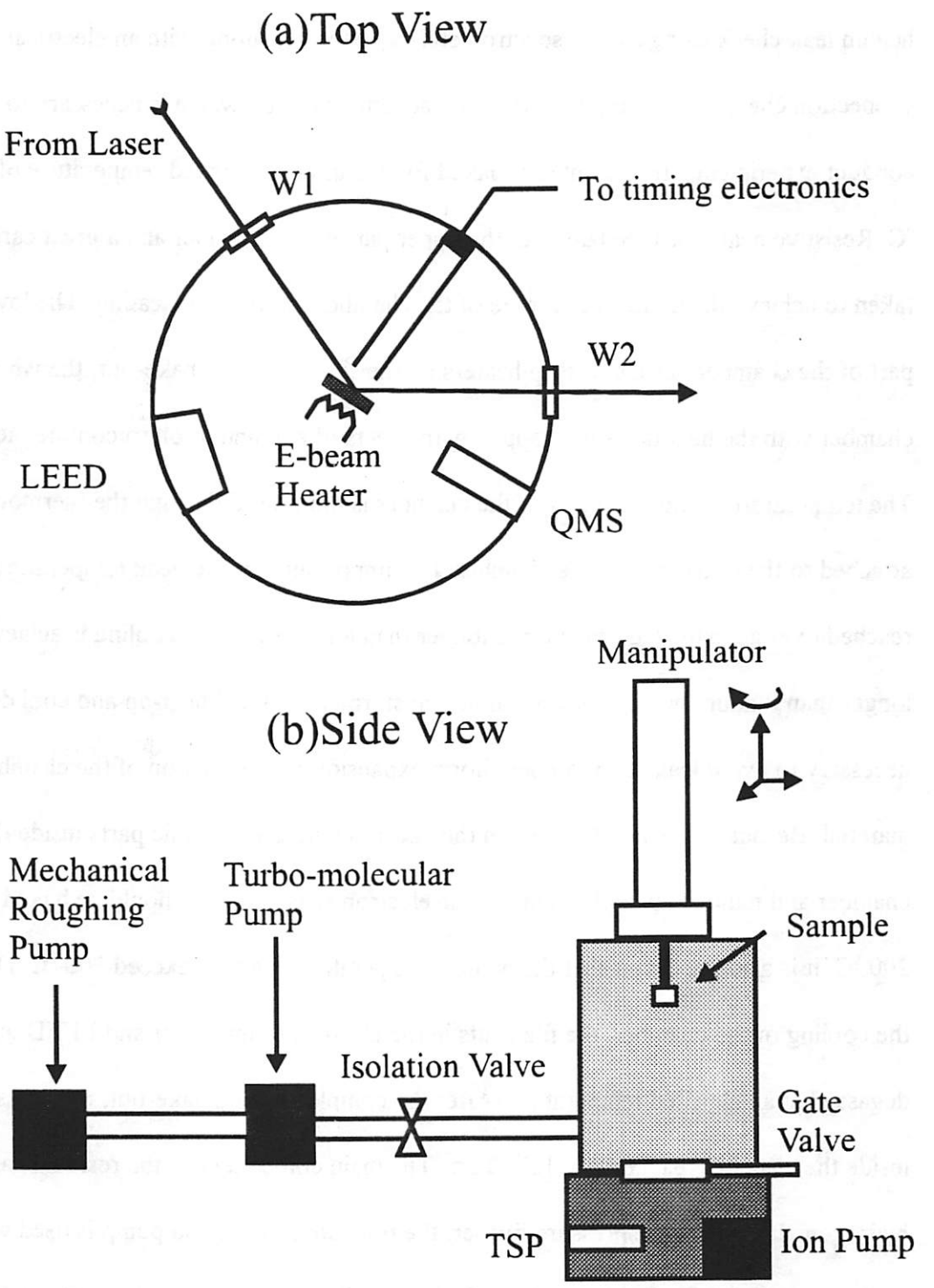

Fig 2-4. Schematic of the vacuum system. (a) Top View (b) Side View

W1 : entrance window, W2: exit window, QMS : Quadrupole Mass Spectrometer

TSP : Ti sublimation pump

helium leak check using a mass spectrometer is performed along with an electrical connection check. To obtain the ultrahigh vacuum condition which is necessary to conduct experiments, the chamber is baked for 1-2 days at elevated temperature of 170 °C. Resistive heat tapes are laid over the upper part of the chamber and a great care is taken to achieve the uniform coverage of the chamber for uniform heating. The lower part of the chamber has metal strip heaters on the side. During a bake-out, the whole chamber with the heat tapes is wrapped with sheets of aluminum foil to confine the heat. The temperature of various parts of the chamber is monitored through the thermocouples attached to the outer wall of the chamber. It is important that the peak temperature is reached over an extended time period longer than 8 hours and the cooling is achieved longer than 8 hours by adjusting a Variac transformer. Gradual heat-up and cool down is necessary to avoid leaks due to nonuniform expansion or contraction of the chamber material. Because the silver brazing on the vacuum window, ceramic parts inside the chamber and multichannel plates inside the electron spectrometer should be baked below 200 °C, it is also important that the highest temperature is not to exceed 200 °C. During the cooling of the chamber, the filaments in the electron beam heater and LEED gun are degassed at an elevated temperature. After the completion of a bake-out, the pressure inside the chamber reaches low 10^{-10} Torr. The main component of the residual gas is hydrogen. To reduce the pressure further, the titanium sublimation pump is used with its wall cooled by liquid nitrogen. After a flash of sublimation pump for 1 minute at 45 A current, the pressure reading on the ion gauge reaches below 5×10^{-11} Torr and stays at that pressure for an extended period of time.

2.3 Electron spectrometer

The energy of the photoemitted electrons is measured using the time-of-flight technique. The flight tube is made out of oxygen-free high conductivity copper tubing. The length of the tube is 25 cm and its diameter is 2.54 cm. The outer wall of the flight tube is surrounded by a mu metal shield. The inside of the tube is coated with graphite (Aquadag) to prevent inhomogeneity in the work function in the inner wall of the flight tube. The flight tube is electrically grounded to the chamber wall. The entrance of the tube is covered with a thin copper mesh with 90% transmission. Placing the entrance of the flight tube as close to the sample as possible is crucial in overcoming the static charging effect which arises from the static charge on the insulating materials inside the vacuum chamber. In the current experiment, the distance between the sample and the tube entrance is 2.5 cm.

At the end of the flight tube is situated the electron detector [32]. The schematic of the electron detector is shown in Fig. 2-5. It consists of a pair of multichannel plates of diameter 2.54 cm. A multichannel plate (Varian) is a doped glass composed of parallel microchannels [33]. The resistance of an individual multichannel plate is approximately 300 MΩ acting as part of the voltage divider. A high voltage of 2 kV is applied across the multichannel plates and resistors in series. The DC current flowing through the voltage divider is monitored with a current meter as a way of ensuring the proper bias on the multichannel plates. The exit aperture of the flight tube is also covered with a high transmission copper mesh. The electrons passing through the copper mesh are accelerated to approximately 120 eV by the bias between the flight tube

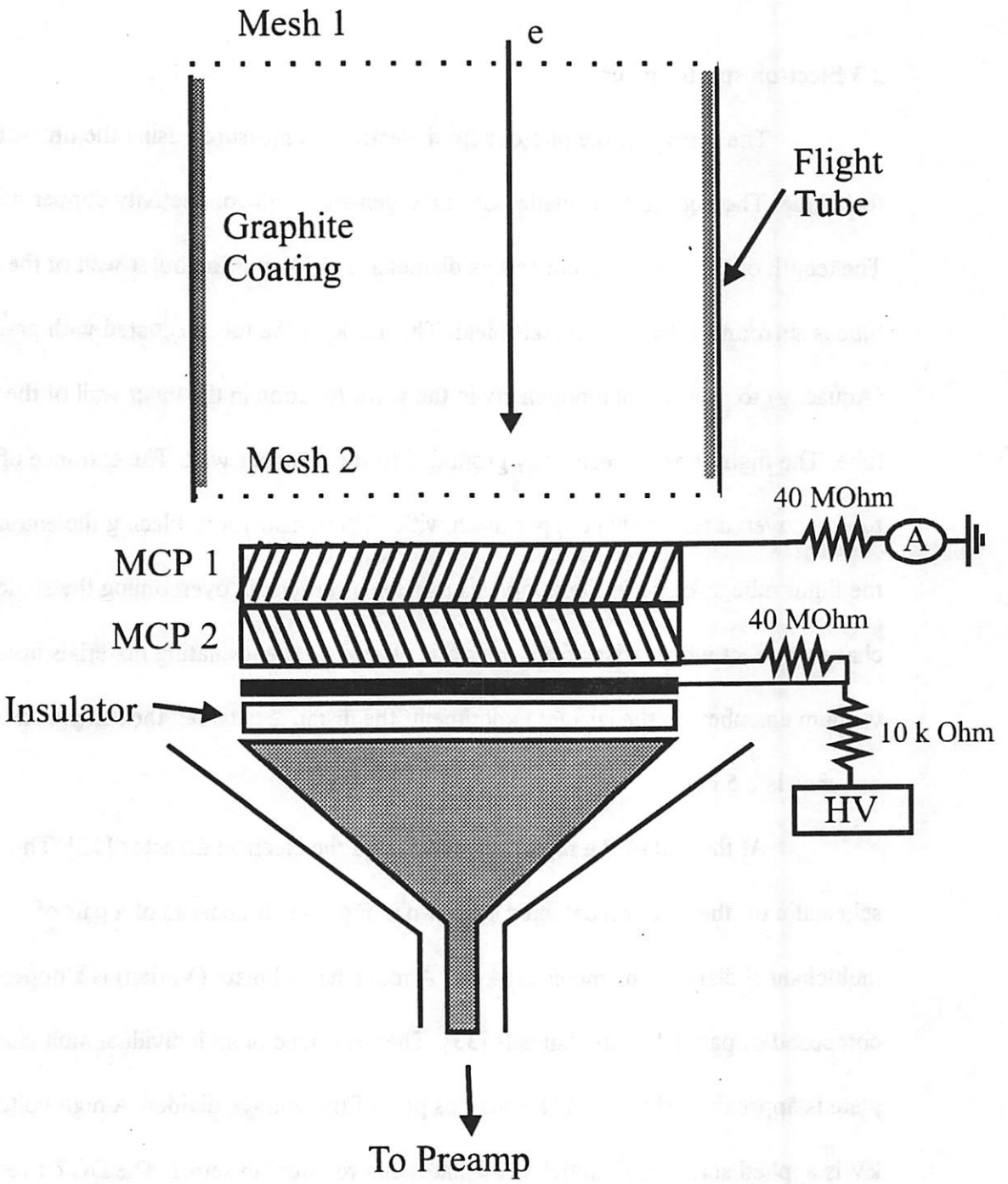

Fig 2-5. Electron detector schematic

and the first multichannel plate. The electron hitting the channel wall of the first plate generates secondary electrons through the microchannel and those secondary electrons are further multiplied while they travel and hit the channel. Further amplification is achieved through the second multichannel plate. The overall gain of the pair of the multichannel plates is approximately 10^6. The electrons hitting the last metal plate induce a transient current in the metal plate which is capacitively coupled to the anode. The capacitive coupling is required because the output end of the electron multiplier is held at high voltage. The shape of the conical anode is designed in such a way that its impedance is 50 Ω to minimize spurious reflections. The signal is further multiplied through a high speed pre-amplifier (Miteq, AU-4A-0150) by a factor of 1000. These pulses carry the timing information about the arrival of the electrons at the detector and these timing pulses are processed through the timing electronics.

The schematic of the timing electronics is shown in Fig.2-6. The electrical pulses after the preamplifier are negative-going pulses with 20 nsec FWHM. Their amplitudes vary from 60 mV to 500 mV due to the stochastic nature of electron multiplication through the electron multiplier. A 24 m cable provides an electronic time delay of 130 nsec so that the start pulse and stop pulses for the Time-to-Amplitude Converter have an appropriate temporal spacing. The electrical pulses are fed into the constant fraction discriminator (Tennelec, TC 454) which converts incoming pulses greater than a certain level into ECL pulses. These ECL pulses go through a routing logic circuit which routes the ECL pulses into different Time-to-Amplitude Converters according to the order of arrival of the pulses. Each channel of the routing logic is connected to the "stop" input of the time-to-amplitude converter (TAC, EG&G, 566)

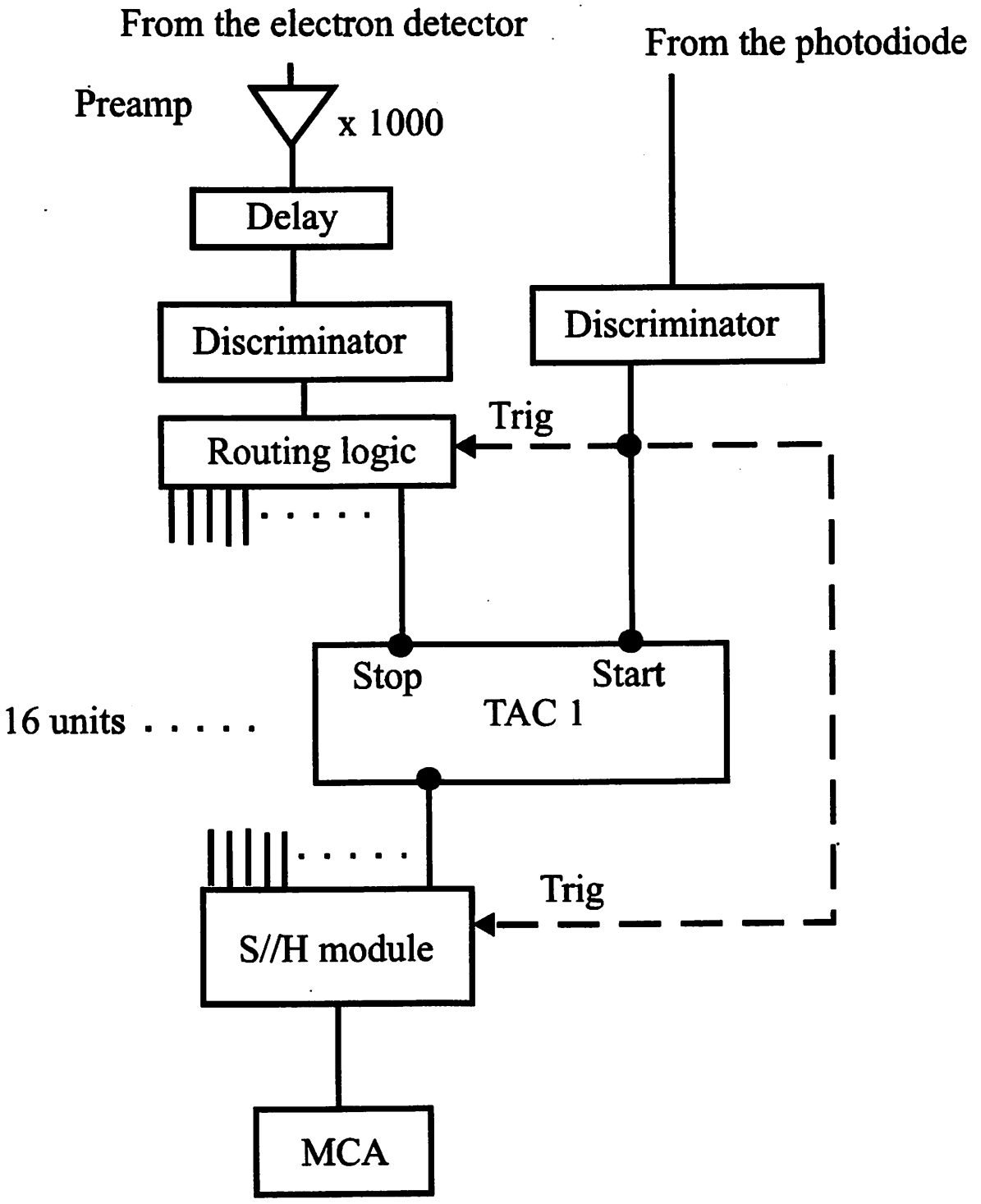

Fig 2-6 Schematic of the timing electronics

whose start pulse is provided by the fast photodiode mentioned in 2.1. The output voltage of each TAC is proportional to the timing between the "start" pulse and the "stop" pulse. The calibration of the TAC is achieved by generating "start" and "stop" pulses at a prescribed time interval and measuring the output voltage of each TAC with a multichannel analyzer. The parallel output of the sixteen TACs is multiplexed through a sample-and-hold module. The height of the pulse is read by a multichannel analyzer plug-in board (EG&G, 916A) inside a personal computer. The pc plug-in board is controlled by a vendor-provided software (EG&G, Maestro for Windows).

The electron spectrometer system can record time-of-flights of sixteen electrons per laser shot but the number of electrons per laser shot is usually limited by the consideration of space charge effect, which is discussed in section 3.2. The time-of-flight method is a multichannel detection scheme which is suitable for a low-repetition rate pulsed laser system. In the time-of-flight scheme, the spacing between the laser pulses should be longer than the sum of the flight time of electrons, electronic delay of the timing electronics and the conversion time of the analog-to-digital converter in the multichannel analyzer. The conversion time, or dead time, is generally longer than 25 microseconds, which puts the maximum repetition rate of the whole system lower than 20 kHz. The advantage of the time-of-flight scheme is the suppression of the background electrons or dark counts through a time-gating. It is worth mentioning that there are other schemes to detect the energy of photoemitted electrons. Electrostatic analyzers such as the cylindrical mirror analyzer and hemispherical analyzer are used mostly for a single channel detection scheme where a certain energy window is defined and the number of

electrons within that energy window is counted for a certain amount of time. The single channel detection scheme is suitable for a high-repetition rate laser system in which time-of-flight method cannot be applied and the electron count per laser shot is low.

The time-of-flight of an electron, which is the time that it takes for an electron to traverse the distance between the sample and the electron detector, is calculated by referencing the arrival time of an electron to that of the so-called photon peak. Part of the 266 nm beam is scattered off the sample surface due to the microroughness of the sample surface and it is registered in the electron multiplier because the multichannel plate is also sensitive to ultraviolet radiation. Because the time-of-flight for the photon through 27.5 cm distance is approximately 1 nsec which is negligible compared to that of electron with 1 eV kinetic energy, the arrival time of the photon peak can be considered as the time at which the electrons leave the sample. Fig. 2-7 shows an electron time-of-flight spectrum which shows a photon peak due to 266 nm and a smooth electron spectrum.

To convert the time of flight counts (dN/dt) into an electron energy spectrum (dN/dE) the following formula is used.

$$\frac{dN}{dE} = \frac{dN}{dT} \cdot \frac{dT}{dE}$$

Because $E = \frac{1}{2} m \left(\frac{L}{T} \right)^2$ where L is the flight tube length and the T is the flight time,

$$\frac{dT}{dE} = \frac{1}{2} \left(\frac{T}{E} \right).$$

Hence, $\frac{dN}{dE} = \frac{dN}{dT} \cdot \frac{T}{2E}$.

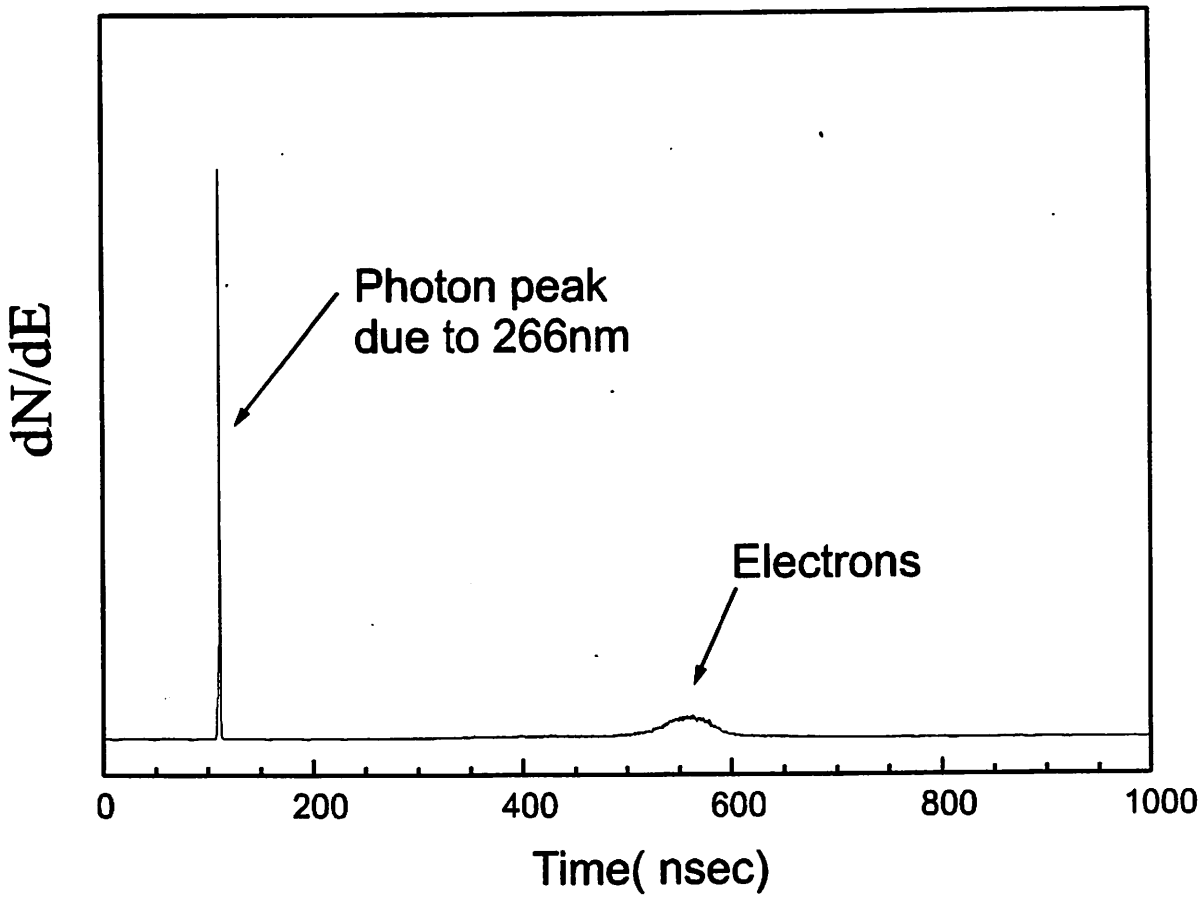

Fig 2-7. Sample time-of-flight spectrum

This method results in large noise and unnecessarily fine energy spacing at low kinetic energy (long flight time). To circumvent these difficulties, an averaging is performed over neighboring bins in flight time. An alternative approach to convert the dN/dT data to an energy spectrum is to subdivide the energy region of interest into intervals of equal magnitude and to count the number of electrons for each energy interval from the time-of-flight spectrum. These two methods result in essentially the same result.

Fig. 2-8 shows the magnified view of the photon peak. The full-width at half maximum of the photon peak is less than 1 nsec. It can be taken as the overall time resolution of the detector including the multichannel plate , the preamplifier, the discriminator, and electronics thereafter. It is worth mentioning that the height of the photon peak can serve as a reasonable *in situ* measure of the pulse energy of the probe beam. Because the scattering of a 266 nm photon is due to the sample roughness on a microscopic scale, it is found that the photon peak height depends on the sample preparation, cleaning procedure, and the experimental geometry. Hence, the photon peak height cannot serve as an absolute measure of the intensity of the 266 nm probe beam but it can be a convenient relative measure within the same run of experiment as long as the geometry among the sample , incoming light and the detector is not changed. One caution is that when the scattering of 266 nm photons is too strong, the photon peak height cannot serve as the relative measure of the third harmonic intensity. When the probability of scattering of photons into the flight tube is bigger than one per laser shot, there is a greater chance of having two photons arriving at the detector simultaneously. Even with two photons arriving at the same time, the electron detector registers only one peak and it

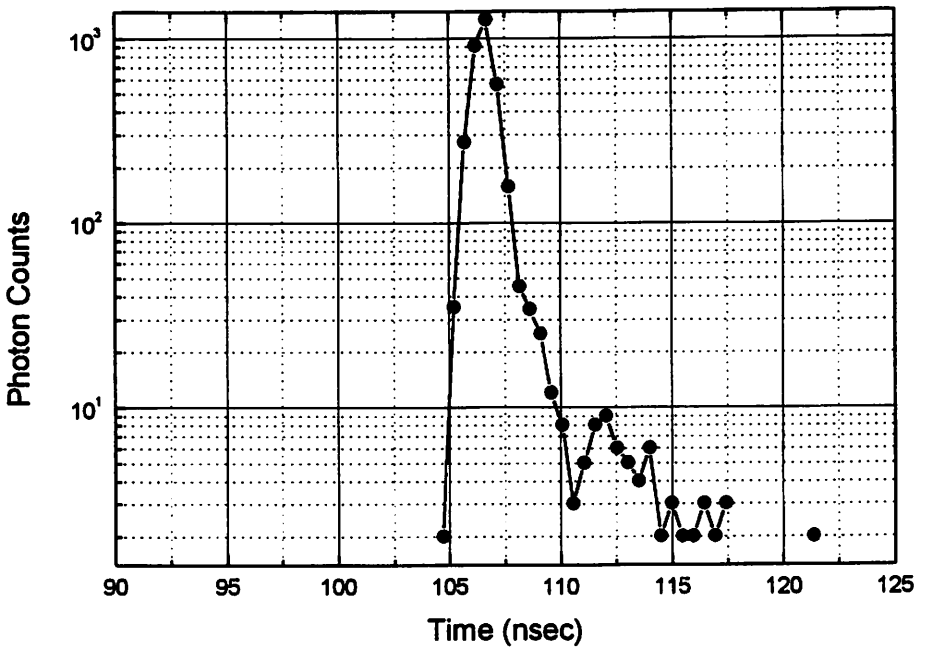

Fig. 2-8 Photon peak spread

is treated as one count. Therefore, an appropriate caution should be exercised when the photon peak height is used as a measure of the third harmonic intensity.

2.4 Sample preparation.

For the experiments described in this thesis, three different Si(100) samples are used to satisfy certain experimental requirements. The table 2-1 shows the doping density, resistivity and crystal face of the three samples. For each of the samples, the resistivity, dopant and the miscut are specified from the wafer manufacturer. From the given resistivity, the doping density is calculated by using mobility values given in reference [11].

Sample #	**Crystal Face**	**miscut (degree)**	**dopant**	**doping density (cm^{-3})**	**resistivity ($\Omega \cdot cm$)**
Sample 1	100	$< \pm 0.5$	B(p-type)	10^{15}	15 ~30
Sample 2	100	9	P(n-type)	1.2×10^{13}	350
Sample 3	100	$< \pm 0.5$	Sb(n-type)	$> 2 \times 10^{18}$	0 ~ 0.02

Table 2-1. Sample specifications

Samples are cleaned in acetone and methanol for approximately ten minutes in order to remove particle contaminants and grease. Before introduction into the chamber, the native oxide on the surface of the sample is removed by dipping into a buffered HF solution. After an HF dip, the surface of the sample is terminated with hydrogen, which is

evidenced by the de-wetting of the surface. The hydrogen termination of the silicon surface is known to be stable for approximately two hours in the air [34]. The sample is mounted on the XYZ sample manipulator immediately after HF cleaning and deionized water rinsing. As a next step, the manipulator is installed in the vacuum chamber for the pump-down. After the baking cycle is completed, the sample can produce a weak LEED pattern. But more frequently, the sample surface is not clean enough to produce a well-ordered LEED pattern. It is suspected that the oxygen ions produced by hot filaments such as ion gauge filaments inside the chamber oxidize the sample surface [35]. Prior to the sample cleaning, the electron beam heater filament and its housing are thoroughly degassed by a successive heating to 600 °C and they are cooled down overnight. The temperature of the sample plate is monitored through the thermocouples attached onto the specimen plate which is in thermal contact with the sample. Before cleaning of the sample, the titanium sublimation pump is turned on for one minute with its wall cooled with liquid nitrogen to reduce the pressure inside the chamber. The sample is cleaned by heating to 1300 K for two minutes using the electron beam heater. At the highest temperature, the pressure inside the chamber usually surges to the low 10^{-9} Torr range. Approximately at 1100 K, the sample starts glowing faint red and as the temperature becomes higher, the sample glow becomes brighter. After slowly cooling the sample to room temperature at a rate of 20 K per minute, a very sharp 2x1 LEED pattern is observed. The LEED pattern survives a few weeks but the sharpness of the pattern degrades with time. The LEED pattern becomes sharp again after annealing the sample at 1000 K. The LEED pattern is monitored after each run of the experiment.

Chapter 3.

Harmonic Generation and Space charge effect

This chapter is devoted to the discussion of experimental concerns regarding the third harmonic generator and the space charge broadening of the electron energy spectrum. The efficient generation of third harmonic pulses without any temporal broadening is important to achieve the best possible time resolution. The space charge broadening of the electron energy spectrum limits the number of electrons that can be detected per laser shot and the energy resolution of the detector.

3.1 Harmonic generator

In this section, a detailed account of the third harmonic generator is given. The third harmonic generator schematic is shown in Fig 3-1. It consists of two Beta-Barium Borate ($\beta - BaB_2O_4$ or BBO) crystals which are known to have the highest second order susceptibility [36]. The first crystal that generates the second harmonic beam, is 1 mm thick and it is cut 30 degrees with respect to the optic axis for the type I phase matching between the 800 nm beam and 400 nm beam. Because the second order nonlinear susceptibility is orders of magnitude greater than that of the third order, employing two second-order processes (second harmonic generation and sum frequency generation) is more efficient than using only one third order process (third harmonic generation). The second crystal that mixes the 800 nm beam and 400 nm beam, is 0.3 mm

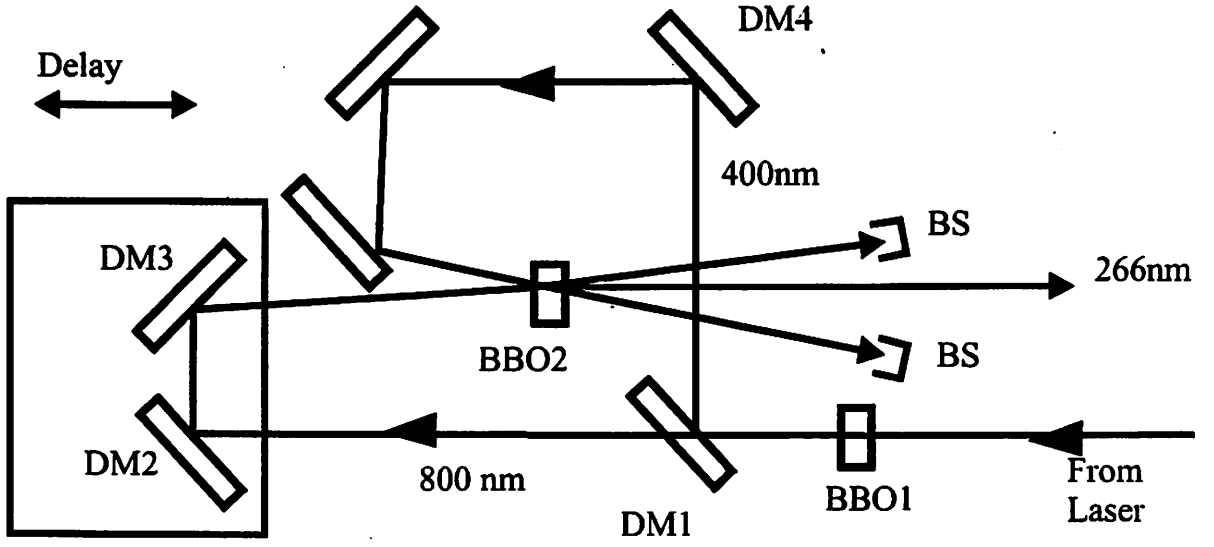

Fig 3-1. Schematic of the harmonic generator

DM : Dichroic mirror BS : Beam stop

thick and it is cut 58 degrees for the type II phase matching between the 800 nm beam, 400 nm beam, and 266 nm beam .

The angles of the crystals are chosen from the phase-matching conditions. The type I phase matching condition for second harmonic generation is [37]

$$n(2\omega) = n(\omega) \quad \text{(Eq.3-1)}$$

Due to the material dispersion, it's impossible to satisfy the above condition when the two beams are the same type, i.e. when both are ordinary rays or both are extraordinary rays. However, the condition (Eq. 3-1) can be achieved by taking advantage of the fact that the index of refraction of a uniaxial crystal for an extraordinary wave depends on its direction of the propagation with respect to the optic axis of the crystal. The index of refraction for an ordinary ray remains the same without regard to its direction of propagation. The index of refraction of an extra-ordinary ray is given by the formula [2]

$$\frac{1}{n_e^2(\theta)} = \frac{\cos^2\theta}{n_o^2} + \frac{\sin^2\theta}{n_e^2} \quad \text{(Eq. 3-2)}$$

where θ is the angle between the optic axis and the propagation direction. Eq. 3-2 can be solved for the crystal angle cut θ.

$$\sin^2\theta_m = \frac{n_e^{-2}(\theta) - n_o^{-2}}{n_e^{-2} - n_o^{-2}} \quad \text{(Eq. 3-3).}$$

Table 3-1 lists the index of refraction of the BBO crystal for ordinary ray and extraordinary ray at harmonics of the 800 nm beam. This table is compiled by employing the Sellmeir equations for BBO crystals given below [38].

wavelength	*ordinary*	*extraordinary*
800 nm	1.66055	1.54442
400 nm	1.69298	1.56789
266 nm	1.75853	1.61262
200 nm	1.89674	1.70274

Table 3-1. Indices of refraction of BBO crystals at 800, 400, 266 and 200 nm

$$n_o^2(\lambda) = 2.7359 + 0.01878/(\lambda^2 - 0.01822) - 0.01354\lambda^2 \quad \text{(Eq. 3-4)}$$

$$n_e^2(\lambda) = 2.3753 + 0.01224/(\lambda^2 - 0.01667) - 0.01516\lambda^2 \quad \text{(Eq. 3-5)}$$

where λ is the wavelength in units of a micrometer. Following the method outlined above, the phase matching angle between 800 nm beam and 400 nm beam is calculated to be $29.2°$.

The phase matching condition for the sum frequency generation for ω_1 and ω_2 to produce ω_3 is $\omega_1[n(\omega_3) - n(\omega_1)] + \omega_2[n(\omega_3) - n(\omega_2)] = 0$ [40]. In a birefringent crystal, it's possible to satisfy the condition by choosing ω_3 to be an extraordinary wave. In type II phase matching, either ω_1 or ω_2 is ordinary. In the current set-up, the 800 nm beam is taken to be an extraordinary wave and the 400 nm beam is taken to be ordinary. Following the same recipe as was outlined for finding the phase-matching angle of the

second harmonic crystal, the type II phase matching angle for mixing the 800 nm beam and 400 nm beam to produce 266 nm beam is found to be $55.7°$.

For these choices of phase matching angles, the wave characteristic, index of refraction, group velocity and polarization of each beam are summarized in Table 3-2. The group velocity is calculated using the formula

$$v_g = \frac{d\omega}{dk} = \frac{c}{n}\left(1 + \frac{\lambda}{n^2}\frac{dn}{d\lambda}\right) \quad \text{(Eq. 3-6).}$$

Wavelength	wave	index	group velocity	polarization
800 nm	ordinary	1.66055	c/1.6751	p
400 nm	extra	1.66051	c/1.71143	s
800 nm	extra	1.57862	c/1.5918	p
400 nm	ordinary	1.69298	c/1.7476	s
266 nm	extra	1.65496	c/1.79133	p

Table 3-2 Indices of refraction and group velocities of 800, 400 and 266 nm.

c : speed of light in vacuum

The essential part of the third harmonic generator set-up is a separate delay line between the 800 nm beam and 400 nm beam. Authors of reference [39] pointed out that the group velocity mismatch between the fundamental and its harmonics inside the

nonlinear crystal causes the resultant sum frequency to have wider pulsewidth with low conversion efficiency. The harmonic generation scheme employing a second delay line has been used by the same authors to generate ultrashort 200 nm pulses.

To illustrate the necessity of having a delay line between the fundamental and the second harmonic beam for higher efficiency and for a shorter third harmonic beam, a numerical calculation is performed by solving traveling wave equations inside the nonlinear crystal given the group velocities [40]. The group velocity dispersion within the pulse is assumed to be negligible and perfect phase matching is assumed in the following analysis.

Within the first crystal, the traveling wave equations are

$$\left(\frac{\partial}{\partial z}+\frac{1}{u_{11}}\frac{\partial}{\partial t}\right)A_1=\sigma A_1 A_2 \qquad \text{(Eq. 3-7)}$$

$$\left(\frac{\partial}{\partial z}+\frac{1}{u_{12}}\frac{\partial}{\partial t}\right)A_2=-\sigma A_1 A_1 \qquad \text{(Eq. 3-8)}$$

where $\sigma=\frac{2\pi k_1}{n_1^2}d_1$ with d_1 effective nonlinear coefficient in the first crystal and $u_{11}=c/1.6751$ and $u_{12}=c/1.71143$ with c the velocity of light in vacuum. A_1 and A_2 are the envelopes of the electric field for the fundamental beam and second harmonic beam, respectively. d_1 can be calculated from the angles and the nonlinear optical coefficient of the BBO crystal by [41]

$$d_{ooe}=d_{31}\sin\theta-d_{22}\cos\theta\sin 3\varphi \qquad \text{(Eq. 3-9)}$$

where $d_{22} = 1.78 \times 10^{-12} m/V$ and $d_{31} = 0.12 \times 10^{-12} m/V$ [36]. With these values, σ is calculated to be $1.8 \times 10^{-5} V^{-1}$. The set of equations (Eq. 3-7 and Eq. 3-8) is solved using finite-difference method with $A_1(0,t) = E_1 \exp(-t^2 / \tau^2)$ and $A_2(0,t) = 0$ as boundary conditions.

Fig 3-2 shows the numerical solution to the equations with $E_1 = 0.5$ MV/cm and FWHM = 0.15 psec. The length of the crystal is taken to be 1 mm and the perfect phase matching is assumed. Fig 3-2 (b) shows the input fundamental pulse at the entrance of the crystal. Fig 3-2 (a) shows the intensity of the second harmonic beam (thicker line) and that of the fundamental beam (thinner line) at the exit of the crystal as a function of time. The second harmonic beam intensity has been multiplied by 5 for clarity. The second harmonic beam has a Gaussian temporal profile with its FWHM equal to 0.12 psec. It lags behind the fundamental pulse by 72 fsec. The group velocity mismatch between the 800 nm beam and 400 nm beam is 121 fsec/mm which is approximately twice the time delay observed in the simulation [42]. This difference arises because the second harmonic beam is generated *inside* the crystal, reducing the effective transit length for the second harmonic beam.

The fact that the second harmonic pulse lags behind the fundamental pulse has an important implication in the third harmonic generation. If the crystal for generating the third harmonic beam is placed right behind the first crystal, the overlap between the 800 nm beam and 400 nm beam is not optimized, reducing the efficiency of sum frequency generation and possibly lengthening the resultant 266 nm beam. To illustrate this point, a

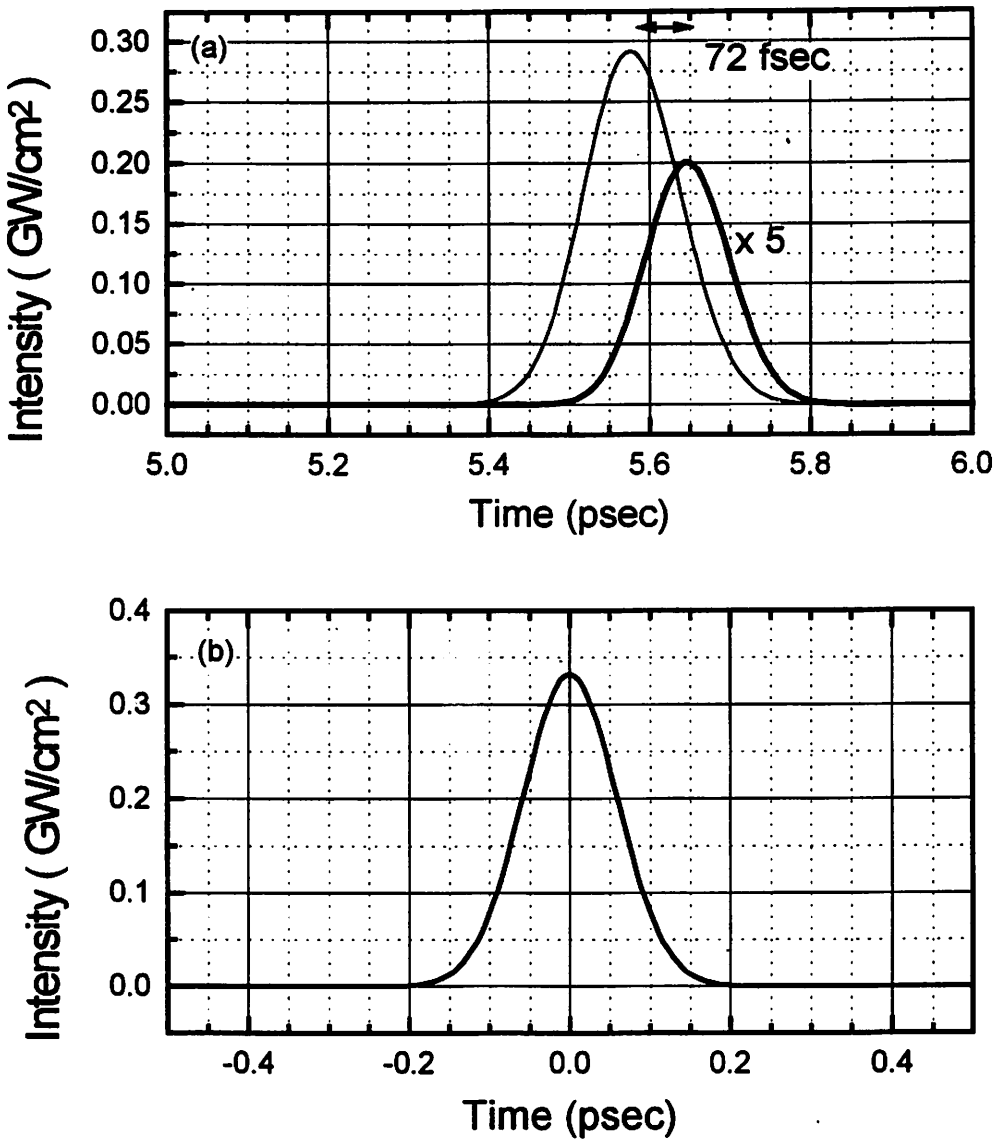

Fig 3-2. (a) The second harmonic beam and the fundamental beam at the end of the crystal.

(b) The input pulse at the start of the crystal.

set of coupled wave equations for three beams is numerically solved with parameters relevant to the second crystal that is used in the generator.

The coupled wave equations are

$$\left(\frac{\partial}{\partial z}+\frac{1}{u_{21}}\frac{\partial}{\partial t}\right)A_1 = -\sigma_1 A_2 A_3 \quad \text{(Eq. 3-10)}$$

$$\left(\frac{\partial}{\partial z}+\frac{1}{u_{22}}\frac{\partial}{\partial t}\right)A_2 = -\sigma_2 A_3 A_1 \quad \text{(Eq. 3-11)}$$

$$\left(\frac{\partial}{\partial z}+\frac{1}{u_{23}}\frac{\partial}{\partial t}\right)A_3 = \sigma_3 A_1 A_2 \quad \text{(Eq. 3-12)}$$

where $\sigma_1 = \frac{4\pi k_1}{n_1^2} d_2$, $\sigma_2 = \frac{4\pi k_2}{n_2^2} d_2$ and $\sigma_3 = \frac{2\pi k_3}{n_3^2} d_2$ with d_2 effective nonlinear coefficient in the second crystal. The set of coupled equations (Eq. 3-10), (Eq. 3-11), and (Eq. 3-12) can be numerically solved with the solution of the (Eq. 3-7) and (Eq. 3-8) as boundary conditions for A_1 and A_2. Temporal delays due to the delay line between the fundamental pulse and the second harmonic beam is incorporated in to the calculation. The length of the crystal is taken to be 0.3 mm.

The Fig. 3-3 shows the integrated energy of the third harmonic beam as a function of the temporal separation between the fundamental beam and the second harmonic beam at the entrance face of the crystal. It shows that the third harmonic intensity is optimized when the fundamental beam is delayed 70 fsec compared to the second harmonic beam. The group velocity mismatch between the fundamental beam and the second harmonic beam inside the second nonlinear crystal is 0.52 psec/mm. Therefore, the total delay between the fundamental and the second harmonic beam through 0.3 mm BBO crystal is 156 fsec, which is approximately twice the delay that is

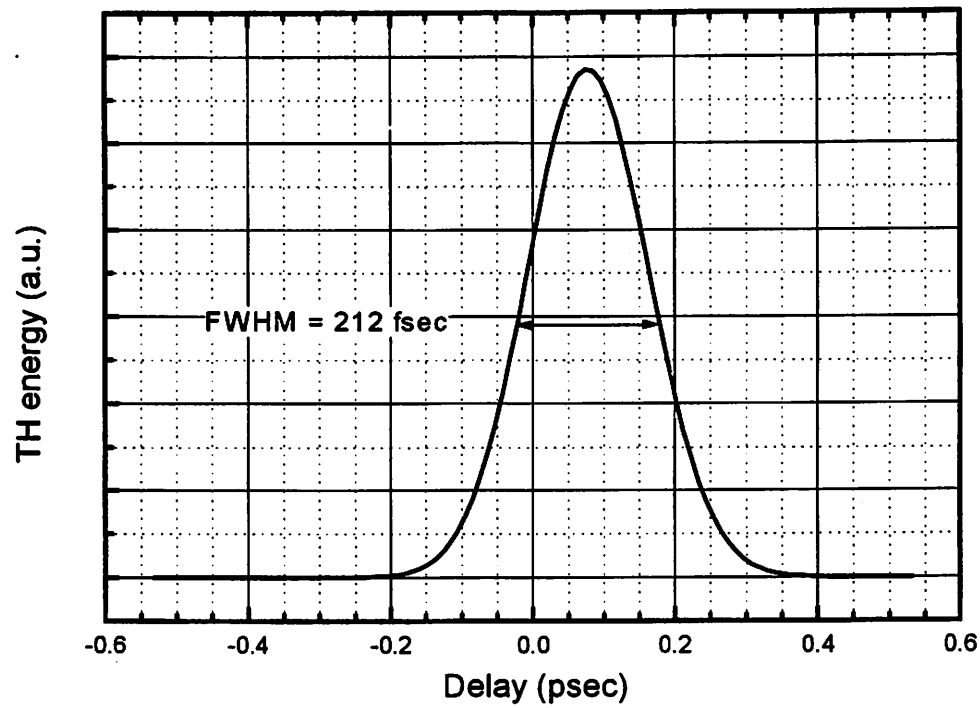

Fig3-3. Integrated energy of the third harmonic beam as a function of the temporal separation between fundamental beam and the second harmonic beam at the entrance of the crystal.

needed for the optimum third harmonic generation. The optimum third harmonic generation is achieved when the maximum overlap between the 800 nm beam and 400 nm beam is accomplished inside the crystal. Because the 800 nm beam travels faster than the 400 nm beam inside the crystal, it is expected that the optimum overlap is achieved when the peaks of the two pulses meet at the center of the crystal. According to Fig. 3-3, the conversion efficiency decreases approximately by six times when the two crystals are arranged in tandem for third harmonic generation without compensating the group velocity mismatch.

The group velocity mismatch inside the nonlinear crystal has an interesting implication with regard to the interpretation of the cross correlation. The cross correlation by nonlinear mixing of a pump beam and probe beam is a well-known method to establish the timing between the two pulses and to measure the pulsewidth of harmonics of a visible laser pulse. But, when the difference between group velocities of the pump and probe beam inside the mixing crystal is appreciable to the pulsewidth of the input beams, the *apparent* timing established by nonlinear mixing can be different from the *true* timing. For example, in Fig. 3-3, the integrated third harmonic intensity is peaked 75 fsec away from the true timing. This effect has to be taken into account when establishing the timing between the pump pulse and the probe pulses using cross correlation. The exact timing between the probe beam and pump beam has to be obtained from the experimental data itself rather than a cross-correlation.

Another effect resulting from the group velocity mismatch inside the nonlinear crystal is that the apparent pulsewidth might be different from the true pulsewidth in the

short pulse limit. For example, in Fig. 3-3, the FWHM of the total energy of the third harmonic as a function of the delay is 212 fsec. The input pulsewidth for the 800 nm beam and the 400 nm beam are 138 fsec, and 111 fsec respectively. Without accounting for the group velocity dispersion, the pulsewidth of the second harmonic beam which can be calculated from the pulsewidth of 800 nm and the measured energy of 266 nm as a function of delay to be

$$\tau_{SH} = \sqrt{\tau_{XC}^2 - \tau_F^2} = \sqrt{212^2 - 138^2} = 161 \text{ fsec}$$

while the true pulsewidth of the second harmonic beam is 111 fsec. This "apparent" broadening of the beam in cross-correlation measurement arises from the group velocity mismatch of the two beams inside the nonlinear crystal. It is more pronounced with a shorter pulse and a longer crystal in which the group velocity dispersion between two pulses is significant over the length of the nonlinear crystal. Because there is a practical lower limit to the thickness of the nonlinear crystal, the apparent broadening has to be taken into account to interpret the cross correlation.

3.2 Space charge effect

The space charge effect is a serious concern with photoemission studies with laser pulses with temporal duration of nanoseconds or less [43], [44]. The distance an electron with kinetic energy of several eV covers for the duration of such a short laser pulse is much smaller than the transverse beam dimension. For example, an electron with 1 eV kinetic energy traverses 0.6 micrometer during a free flight of 1 psec. Therefore, when the laser pulse ejects electrons in such a short time, the spatial distribution of

electrons is the shape of a thin disk. With its small thickness, the density of electrons inside a thin disk-shaped electron cloud becomes so large that the electron-electron interaction through the Coulomb force changes the kinetic energy of electrons during their free flight. For example, if two electrons having the same kinetic energy are ejected to vacuum within close proximity, one electron is pushed toward the sample by the other electron through Coulomb interaction while the other one is pushed away from the sample. Hence the kinetic energies of two electrons differ at the end of the flight and they have different flight times even though they started with the same kinetic energy. Such broadening of the electron energy spectrum is called space charge broadening and puts an upper limit on the number of electrons that can be collected per laser shot. Also it limits the maximum laser fluence we can apply to the sample.

The space charge broadening occurs due to the conversion of internal potential energy to internal kinetic energy. The magnitude of broadening of the electron energy distribution due to the conversion of potential energy can be estimated as follows. The motion of electrons in the cloud can be decomposed into the motion of the center of mass and the relative motion with respect to the center of mass. The velocity of the center of mass denoted as V_{CM} does not change without external force during the flight of the electron cloud. On the other hand, the relative motion of the electrons in the cloud can be described as a velocity distribution $f(v)$. For the sake of discussion, the distribution of internal velocity is assumed to be Maxwellian, i.e.

$$f(v) = \left(\frac{\beta m}{2\pi}\right)^{3/2} \exp\left[\frac{-\beta m v^2}{2}\right] \quad \text{(Eq. 3-13)}$$

where β is related to the width of the distribution. The internal kinetic energy is related to the parameter by $\left\langle \frac{mv^2}{2} \right\rangle = \frac{3}{2\beta}$ where <> denotes the average. The energy distribution viewed from laboratory frame can be characterized by its mean kinetic energy and the width of the distribution which is defined as the standard deviation of the energy distribution. The average kinetic energy and the width of the kinetic energy distribution are

$$\frac{1}{2}mV_{CM}^2 + \left\langle \frac{mv^2}{2} \right\rangle = \frac{1}{2}mV_{CM}^2 + \frac{3}{2\beta} \qquad \text{(Eq. 3-14)}$$

$$\sqrt{\frac{3}{2\beta^2} + \frac{mV_{CM}^2}{\beta}} = \left(\sqrt{\frac{3}{2}}\frac{1}{\beta}\right)\sqrt{1 + \frac{2}{3}mV_{CM}^2\beta} \qquad \text{(Eq. 3-15)}$$

respectively. Eq. 3-15 shows that the width of the energy distribution increases as the internal kinetic energy becomes greater due to the conversion of the potential energy.

The magnitude of the space charge broadening can be estimated by computing the potential energy of electron cloud in front of the sample. The initial electron cloud of a thin-disk shape with radius R and surface charge density σ is considered. Immediately after the electron cloud is generated in front of the sample, the total potential energy for this system is given by

$$E_{pot} = \frac{\sigma^2 e^2 R^3 \pi}{\varepsilon_0}\frac{p}{4} = N^2\left(\frac{d}{R}\right)(p)\,(1eV) \qquad \text{(Eq. 3-16)}$$

where p = 1.22 d = 1.44 nm and N is the number of electrons in the cloud. (See Appendix 2 for the derivation.). When the electrons move away from one another during

their free flight, the potential energy is converted into internal kinetic energy while the velocity of the center of mass of the electron cloud remains the same. The additional kinetic energy "gain" per electron scales as Nd/R. It appears as increase of the internal energy of the same magnitude i.e. $1/\beta' = 1/\beta + \frac{2}{3} pNd/R$. For this effect to be significant, the additional broadening has to be comparable to the energy resolution of the system.

$$Nd/R \approx \Delta E\,(\text{eV}). \quad \text{(Eq. 3-17)}$$

In other words, when the condition $N << \Delta E(R/d)$ is met, the space charge broadening is negligible. In the experiment under discussion in this thesis, the probe beam size is 0.5 mm and the desired energy resolution is 50 meV. For the space charge broadening to be negligible, the number of electrons extracted per laser shot has to be much smaller than 17000, according to the above criteria. Because the solid angle subtended by the detector of area 5 cm^2 with respect to the sample is 6.6×10^{-3}, the fraction of electrons that are accepted into the detector is approximately 1.0×10^{-3}, assuming an isotropic distribution. Therefore, when the electron count rate stays below several electrons per shot, the space charge broadening is negligible in the current experiment.

To verify the criteria (Eq. 3-17) for the space charge broadening, a simulation of free flight of electrons is performed and the energy distribution has been monitored at the start of the flight and at the end of the flight. The simulation consists of simulating the trajectories and velocities of 1024 electrons. The initial mean kinetic energy is 0.80 eV

and the standard deviation of the energy spread is equal to 0.413 eV. The velocity of electrons is assigned using a random number generator. The spatial distribution of electrons is determined by generating random numbers so that the uniform distribution within the region of a thin-disk shape is achieved. The thickness of the disk is mainly determined by the laser temporal pulsewidth, and it is taken to be 0.1 micrometer which is the distance that an electron with kinetic energy of 0.8 eV travels for 0.2 psec. The radius of the disk can be varied from 10 micron to higher values.

Fig. 3-4 shows the initial spatial distribution (Fig. 3-4 (a)) and energy distribution (Fig. 3-4(b)) for a disk of 10 micrometer radius. The potential energy is 0.122 eV , the center of mass kinetic energy is 0.446 eV and the internal kinetic energy is 0.380 eV. The spatial distribution of electrons and the energy distribution of electrons after 10 nanoseconds of free flight are displayed in Fig.3-5. The initial electron energy distribution is superimposed for comparison. The mean kinetic energy changes from 0.826 eV to 0.953 eV, which indicates that most of the potential energy has been converted into the internal kinetic energy. The electron energy distribution is broadened as indicated by the change in standard deviation from 0.4125 eV to 0.5363 eV. The space charge broadening is conspicuous at the high energy side of the spectrum where the distribution cut-off occurs approximately 0.5 eV higher than the initial distribution. To compare the simulation to the simple estimate given above, the radius of electron cloud has been varied while keeping the number of electrons in the cloud the same. The change in the mean kinetic energy, and the change in the standard deviation have been compared with the simple estimate given above. The result is tabulated in the table 3-2. From the table, the final mean kinetic energy is the sum of the initial kinetic energy and the potential

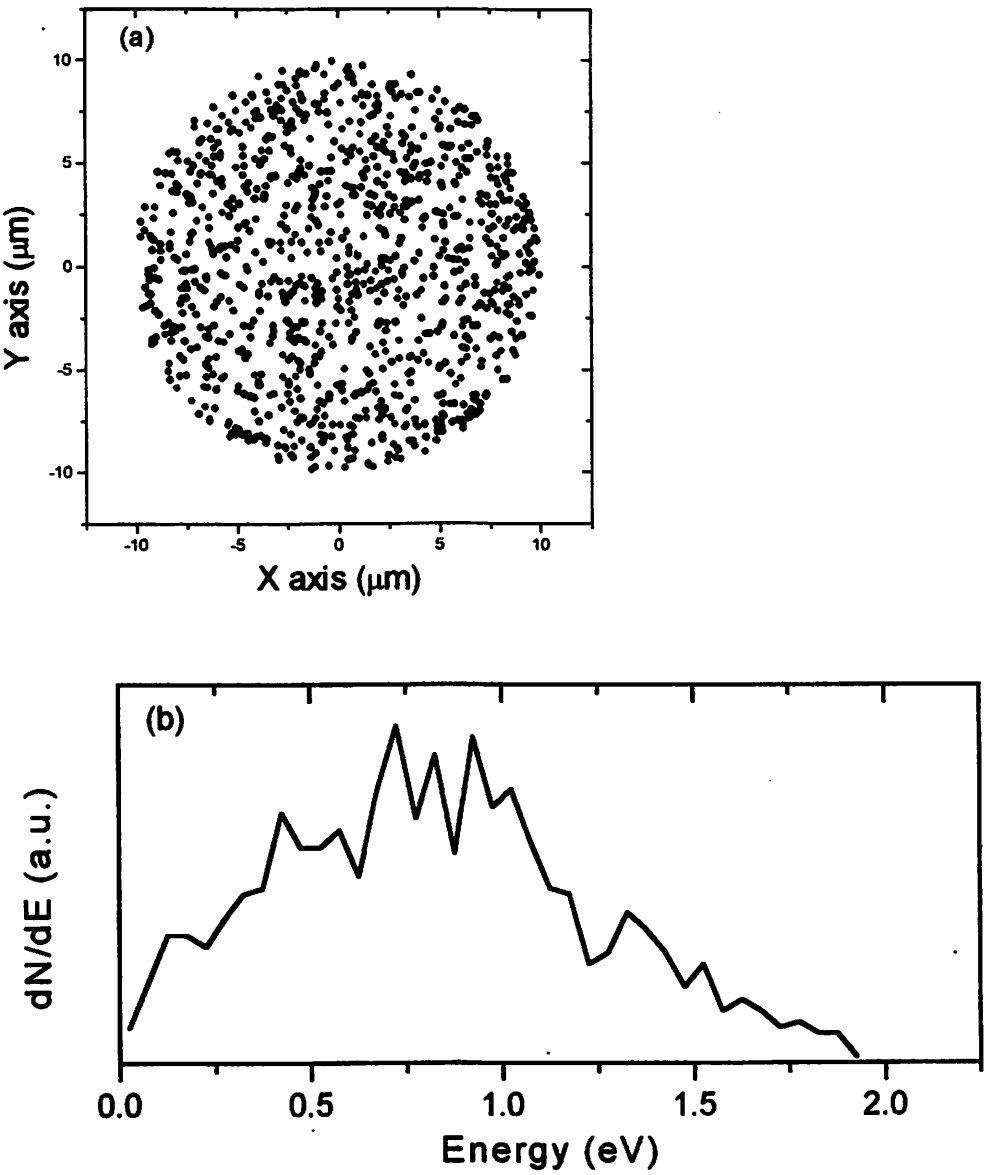

Fig 3-4. Spatial and kinetic energy distribution of electrons at the start of the simulation

(a) Spatial distribution of electrons

(b) Initial kinetic energy distribution

energy and the energy distribution broadens inversely proportional to the radius of the electron cloud. The potential energy estimated by assuming that the disk is infinitely thin is approximately 50% greater than what's measured in the simulation. The factor of 1.5 difference in estimating the potential energy from a simple model can be considered reasonable and the simple model can be used to assess the space charge broadening effect with a given number of electrons and radius of the electron cloud. This model is valid as long as the thickness of the disk is much smaller than the radius, which is the case for photoemitted electrons with short pulse laser illumination.

Another noteworthy result of this estimate is that the space charge broadening is reduced as the radius of the electron cloud becomes smaller while the density of electrons remains the same. This is because the total potential energy per electron in the cloud scales linearly with N. Because the areal density of photoemitted electrons is determined by the fluence, assuming other parameters are fixed, the space charge broadening can be overcome by decreasing the beam spot size while keeping the fluence at the same level.

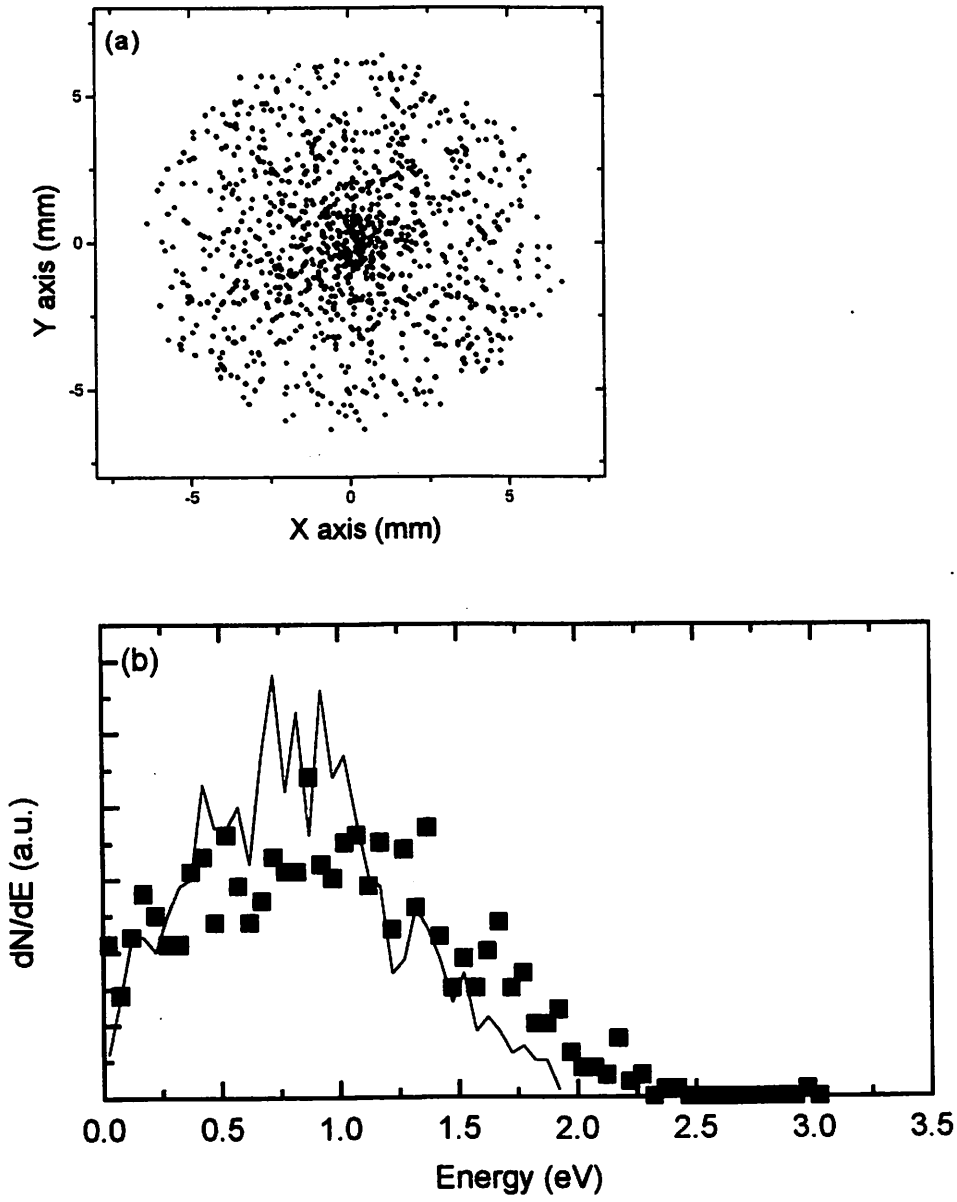

Fig 3-5. Spatial and kinetic energy distribution of electrons at the end of the simulation

(a) Spatial distribution (b) Kinetic energy distribution

Radius micron	*Ef (eV)*	*sf (eV)*	*Epot (eV) simulation*	*Epot (eV) estimate*
10	0.953	0.536	0.122	0.180
15	0.918	0.531	0.0812	0.120
20	0.887	0.474	0.0610	0.09
25	0.875	0.463	0.0488	0.072
30	0.866	0.453	0.04065	0.060
40	0.856	0.444	0.03050	0.045

Table 3-2 : Change in the electron kinetci energy distribution as a function of the radius of the electron cloud. The initial kinetic energy Ei = 0.8259 and the initial standard deviation σ_i = 0.4125

Ef : final mean kinetic energy , sf : final standard deviation of kimetic energy of electrons

Chapter 4. Experimental Results

In this chapter, the experimental results of the time-resolved two-photon photoemission on silicon surfaces are discussed. It is found that the electron energy distribution changes on a subpicosecond time scale near the surface. Especially at time delays near T = 0.0 psec, a nonthermal energy distribution is observed and its subsequent thermalization due to the carrier-carrier scattering is discussed. The electron temperature is extracted from the photoemission spectrum at each time delay and it is found to change on a subpicosecond time scale. The electron temperature also depends on the pump beam fluence, which indicates that two-photon absorption should be included in describing the ultrafast dynamics on silicon surfaces. By use of a simple and qualitative model based on the two temperature model, the carrier-phonon scattering time is determined.

4.1 Ultrafast carrier energy relaxation processes in silicon after pulsed laser excitation.

When laser pulses with subpicosecond temporal duration are incident on the silicon surface, carriers (electrons and holes) are generated by interband absorption of photons. The absorption of a photon occurs on a very short time scale limited only by the Heisenberg uncertainty principle. When the carrier recombination lifetime or trapping time is significantly longer than the laser pulsewidth, the density of photo-generated carriers can be estimated as

$$n = \frac{(1-R)\alpha J}{\hbar\omega}.$$

R : reflectivity of the sample

J : fluence of the incident radiation (J/m^2)

α : linear absorption coefficient of the sample : $10^3 cm^{-1}$ at 800 nm for Si

$\hbar\omega$: pump beam photon energy : 1.55 eV for 800 nm.

Part of the energy in the incident radiation is used for overcoming the bandgap, E_g, and the excess energy, $\hbar\omega - E_g$, is deposited as the kinetic energy of the electron-hole pair. Because the heat capacity of the carriers is much lower than that of the lattice, the carrier temperature can be considerably higher than that of the lattice. For example, when an 800 nm laser pulse with 100 fsec pulsewidth and 1 mJ/cm^2 fluence is incident on the silicon surface, the photogenerated electron density is 2.8×10^{18} cm^{-3}, with the same hole density. In a non-degenerate regime, the heat capacity of the electrons and holes is approximately $\frac{3}{2}Nk_B$ by equipartition of energy where N is the density of the free carriers. Because the excess kinetic energy per electron-hole pair is $\hbar\omega - E_g$, the temperature of the carriers can be estimated by

$$2 \times \frac{3}{2} k_B \Delta T = \hbar\omega - E_g$$

where the factor of 2 accounts for the fact that the density of the electrons is the same as that of the holes. The resultant temperature (ΔT) can be as high as 1670 K.

While the carrier temperature can reach as high as 1670 K with ultrafast laser pulse irradiation, the electrons (holes) lose their kinetic energy to the lattice through carrier-phonon interactions and they accumulate at the bottom (top) of the conduction

(valence) band. There are two phonon branches in silicon: acoustic phonon and optic phonon. Among these, the emission of a longitudinal optic phonon (LO phonon) is the main energy loss mechanism of high energy carriers due to its large energy [45]. After several picoseconds, LO phonons finally break up into acoustic phonons , inducing a lattice temperature rise. Because the lattice heat capacity is much greater than that of the carriers, the lattice temperature rise is minimal. For example, the heat capacity of Si is $C_L = 2.07 \times 10^6$ J/m^{3}K [46], and the temperature rise for incident optical energy of 1 mJ/cm^2 is 0.093 K. Therefore, the lattice remains relatively cool, while the carrier energy distribution can achieve much higher temperature for a short period with the ultrafast laser pulse irradiation. The relaxed electrons and holes eventually recombine. Generally, recombination occurs on a time scale longer than hundreds of nanoseconds and it can be neglected in this study of carrier dynamics occurring on a subpicosecond time scale.

Although the lattice temperature rise per laser pulse is small, the accumulated optical pulse irradiation may raise the lattice temperature considerably if the heat extraction is not efficient. In fact, when the pump beam is incident on the sample with an average power of 200 mW, a 10 - 20 K rise in the sample temperature is observed through the thermocouples attached onto the sample holder plate. Because the thermal conductivity of silicon is 142 $W/K \cdot m$, comparable to that of some metals, the temperature of the front surface is expected to be equilibrated with that of the back surface. Therefore, the maximum temperature rise of the sample is approximately 20 K , which is negligible compared to the carrier temperature.

4.2 Studies of the Si(100) surface electronic structure

Due to the short penetration depth of the 266 nm probe beam (~ 5 nm [11]) and short electron inelastic mean free path (~ 10 nm) for electrons with kinetic energy on the order of 1 eV [10], the photoemission with a 266 nm beam is surface-sensitive. Most of the photoemission signal arises from the region near the surface of the sample within the penetration depth of the probe beam. Therefore, knowledge of the electronic structure of the Si(100) surface is crucial for correct interpretation of the experimental results. In this section, experimental and theoretical studies of the surface electronic structure of the Si(100) surface are reviewed.

On an ideally terminated Si(100) surface as shown in Fig. 4-1(a), each surface Si atom has two dangling bonds. In general, an atomically clean semiconductor surface undergoes a reconstruction and/or relaxation, to reduce the surface electronic energy [47]. Through Low Energy Electron Diffraction (LEED) studies [48], it is well-known that a clean Si(100) surface undergoes a 2x1 reconstruction. As shown in Fig. 4-1(b), two neighboring surface silicon atoms form a dimer, accounting for the 2x1 LEED pattern. The dimerization reduces the number of dangling bonds of the surface stoms by half. However, it is not clear whether the surface dimer configuration is symmetric or asymmetric. The majority of the studies favor the asymmetric dimer model. Chadi [49] performed an energy-minimization calculation for many possible structural models of the Si(100) 2x1 surface and he found that the most favorable configuration is that of the asymmetric dimers. He also showed that the asymmetric dimer gives rise to a semiconducting surface, which agrees with the ultraviolet photoemission study [50].

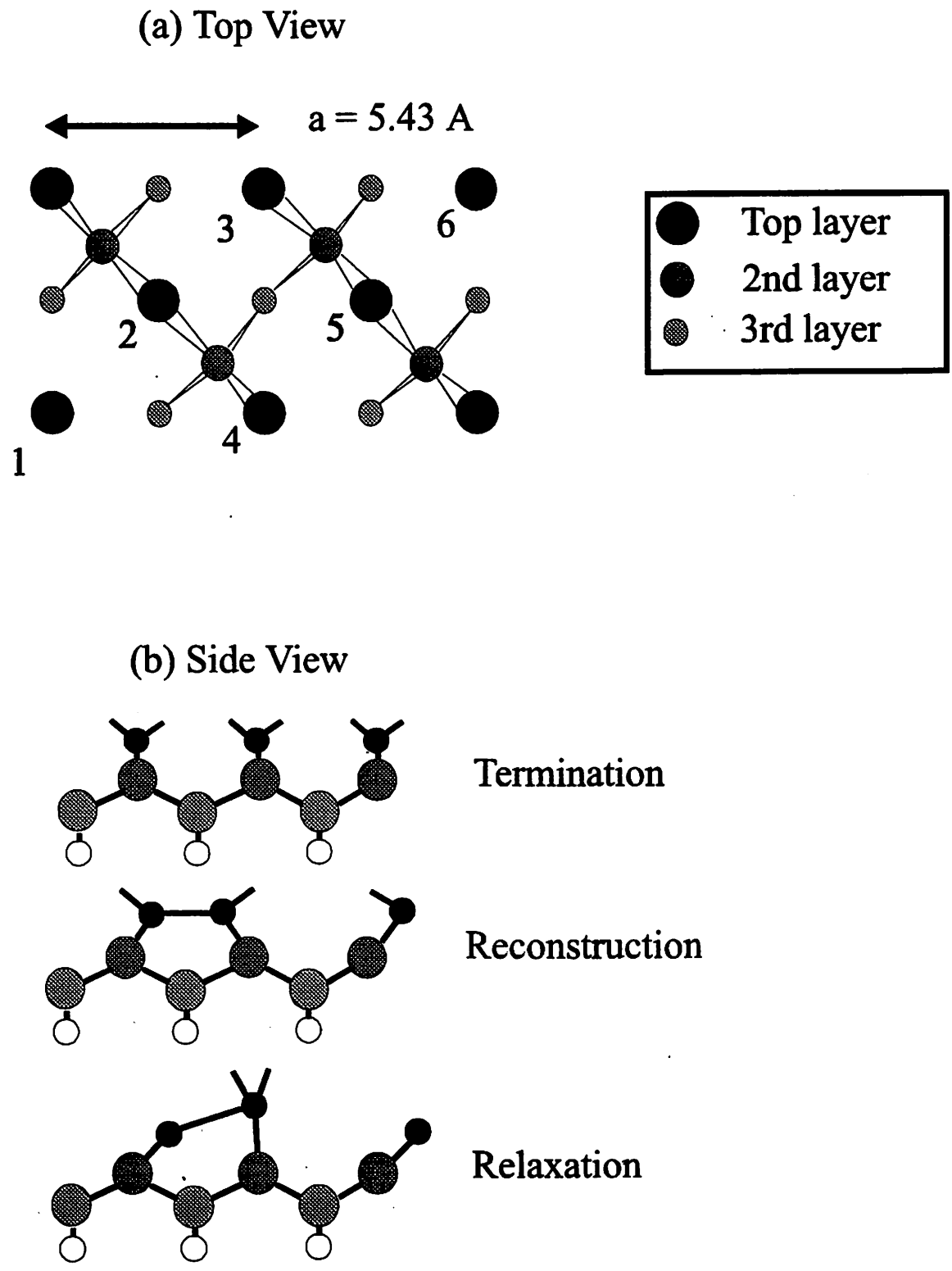

Fig. 4-1 Surface reconstruction of the Si(100) surface

Chadi's model can also explain the occurrence of c(4x2) and p(2x2) reconstruction elements found in the LEED studies [51], [52], [53], [54]. However, Pandey [55] found a considerable decrease in the surface total energy when the missing dimer defect is introduced. Artacho and Yndurain [56] proposed that the configuration of symmetric dimers has the lowest total energy due to an antiferromagnetic spin arrangement within the dimers. According to real space topographic studies by scanning tunneling microscopy, the Si(100)2x1 surface has a high density of point defects and the dimers are observed to be symmetric on most of the surfaces with domains of asymmetric dimers around a point defect [57].

Fig. 4-2 shows the surface Brillouin zone (SBZ) of the Si(100)2x1 surface. In a tight-binding description of electronic states, the two remaining dangling bonds per Si dimer give rise to two separate electronic states. The state with lower energy has a bonding character with an antinode at the midpoint of the dimer. The other state with higher energy has an anti-bonding character with a node at the midpoint of the dimer. The lower surface states are situated below the valence band maximum and they are usually occupied. The occupied surface states have been studied with ultraviolet photoemission spectroscopy[58]. The agreement between the theory [59] and the experiment is excellent except a peak which cannot be explained by any of the surface band calculations. Authors of reference [58] ascribed this peak to a defect-related state on the surface.

There are only a few experimental studies of the upper surface state that is usually empty. Furthermore, the calculated surface band structure for the upper surface states varies considerably. An ultraviolet photoemission spectroscopic study on a heavily

doped n-type Si(100) surface in which part of the upper surface state is occupied has been reported [58]. An inverse photoemission study has been carried out on the Si(100)2x1 surface[60]. In both studies, a surface state has been observed at the Γ point of the surface Brillouin zone as well as the J' point. Most of the band structure calculations predict that the minimum of the upper surface state occurs at the J' point of the surface Brillouin zone while the state at the Γ point has higher energy. The peak at the Γ point of the SBZ has been ascribed to a defect related structure by the authors of [58] and [60].

The STM topographic study on a Si(100)2x1 surface shows a large density of missing dimer defects. The density of the defect is approximately 5 % [61]. Also, on a nominally flat surface, the density of 2x1 domains is equal to that of 1x2 domains whose dimer row is rotated by 90 degrees with respect to that of 2x1 domain. Two domains are joined together by a single atomic step of height a/4 (1.358 A). There are two types of single atomic height steps depending on the relative direction between the step and the dimer row as depicted in Fig. 4-3. For the step denoted as Sa (Sb), the dimer row in the upper terrace runs parallel (perpendicular) to the step edge and that of the low terrace runs perpendicular (parallel) to the step edge. It has also been found that the steps of Sb type have much higher density of kinks than those of type Sa [62]. When the terrace width becomes smaller than a certain length, the Sa step and Sb merge together, forming a double atomic height step, which can be expressed as a "reaction", Sa + Sb = DB. In this case, the Si(100)2x1 surface consists of single domains of Si dimers with parallel orientation. Authors of reference [62] showed that the relative population of 1x2 domain is below 10% of the total area on a Si(100) 2x1 surface with a miscut greater than 4

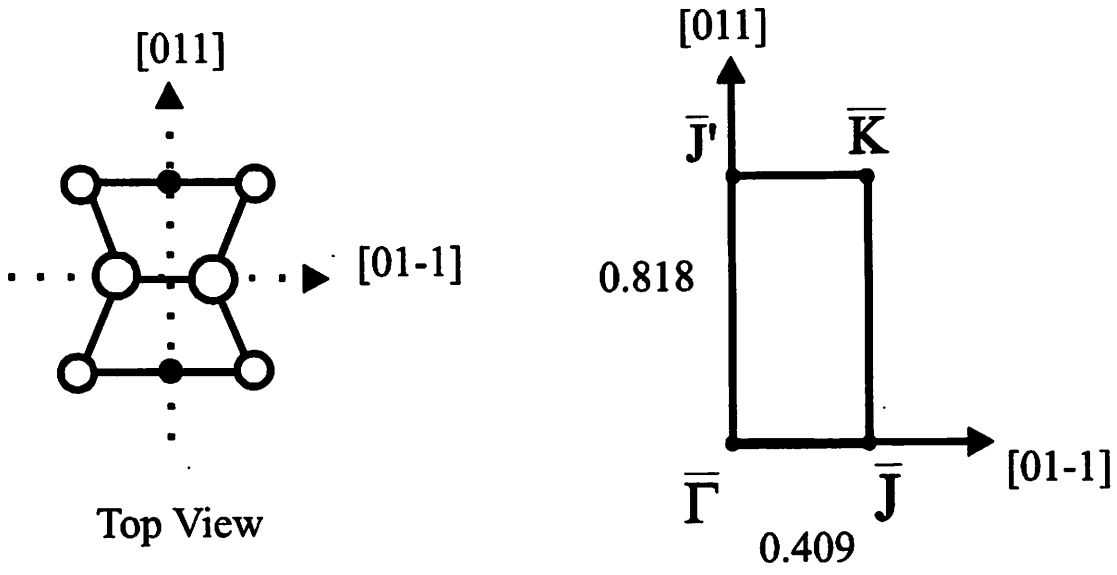

Fig. 4-2 Surface Brillouin zone of the Si(100)2x1 surface

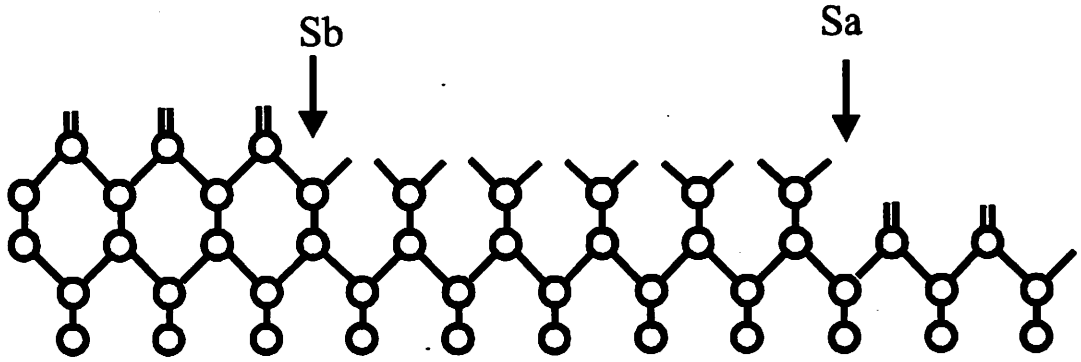

Fig. 4-3 Step structure of the Si(100) surface

degrees. A single-domain Si(100)2x1 surface obtained from the wafers with a miscut angle greater than 4 degrees has an advantage for studying the surface band structure over a double domain surface where the angle-resolved photoemission data mixes up emissions from two different points in the surface Brillouin zone.

4.3 Position of the bulk band edge.

In photoemission spectroscopy, identifying the position of the bulk band edge is crucial in interpreting the experimental results. The energy level of the initial state is related to kinetic energy of a photoemitted electron by the following relation (Fig. 4-4).

$$E_k = n\,\hbar\omega - (\chi - E) + \phi_d = n\hbar\omega + E - (\chi - \phi_d) \quad (1)$$

where $\hbar\omega$ is the photon energy, n is the number of photons absorbed for photoemission, E is the energy inside the sample measured from the conduction band minimum (CBM), χ is the electron affinity, and ϕ_d is the contact potential that arises from the difference in the work functions of the sample and the detector.

In general, identifying the energy position of the initial states for the photoemitted electrons is achieved by taking a spectrum from a reference metal sample in contact with the sample under investigation [63]. The Fermi level of the sample is aligned with that of the reference metal, when they are brought into an electronic contact. The Fermi level of the reference metal can be easily identified from the photoemission spectrum as a sharp onset of the emission. However, this method cannot be employed in the experiments discussed in this thesis, because the probe-beam photon energy (4.65 eV) is smaller than work functions of most metals [47]. The current section discusses a method to identify the position of the bulk band edge, making use of a multiphoton

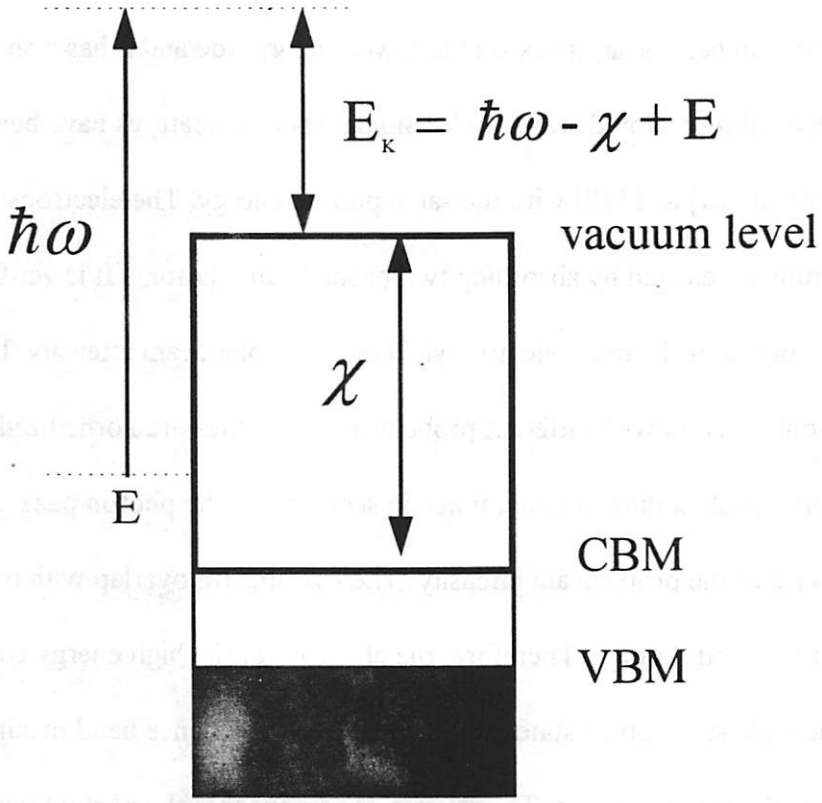

Fig. 4-4 Kinetic energy of photoemitted electrons

photoemission spectrum with a 266 nm beam.

Fig. 4-5 (a) shows five photoemitted electron spectra from a clean Si(100) 2x1 surface (Sample 1 : p-type) when the probe beam with p-polarization is incident on the sample. The spectra are taken with -1.66 V bias on the sample. The probe-only photoelectron spectrum has a sharp peak on the lower energy side and it has a sharp cut-off at 5.0 eV with an abrupt shoulder at 4.4 eV. Similar spectral features have been reported by authors of [15] and [17] with the same photon energy. The electrons in the probe-only spectrum are ejected by absorbing two probe beam photons. It is verified by studying the dependence of the photoelectron yield on the probe beam intensity. In Fig. 4-5 (b), five probe-only spectra with different probe beam intensities are normalized by the square of the photon peak counts. As mentioned in section 2.3, the photon peak count is an excellent measure of the probe beam intensity. The five spectra overlap with one another in the entire spectral range: Therefore, the electrons at the high energy cutoff originate from the highest occupied state which is close to the valence band maximum (VBM) in the case of a p-type sample. The relation (1) shows that the contact potential and the electron affinity of the sample must be known in order to relate the kinetic energy in vacuum to the energy of the initial states inside the sample. From the measurement of the kinetic energy of the electrons emitted from the VBM into vacuum via two photon absorption of 4.65 eV photons, the quantity $\chi - \phi_d$ can be determined. With E_k = 5.0 eV and E = -1.12 eV, $\chi - \phi_d$ is 3.18 eV. Hence the conduction band minimum is located at 1.47 eV in Fig. 4-5.

This method of identifying the band edge states has been used throughout this thesis. The conduction band minimum determined by Eq. 1 agrees well with the onset of

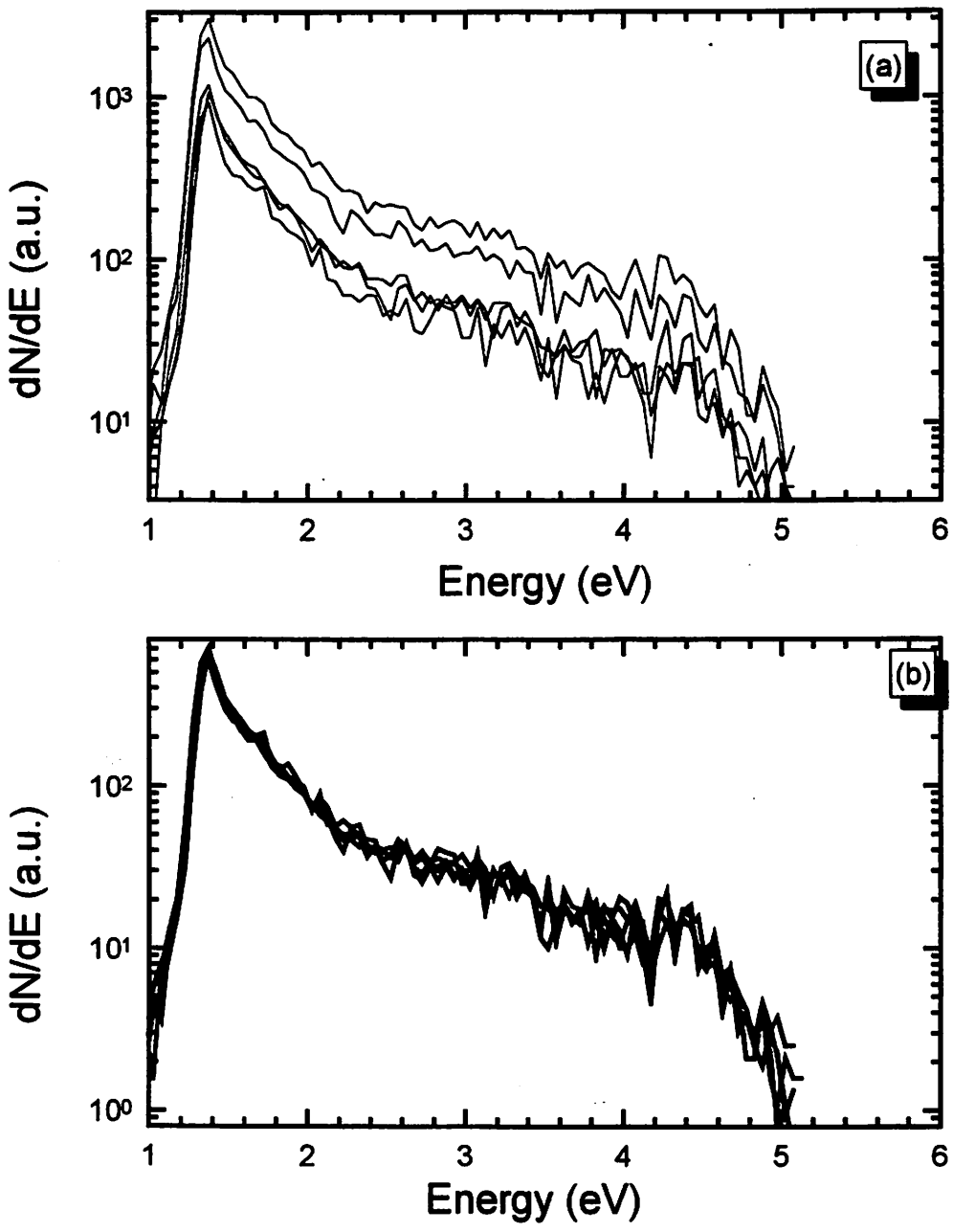

Fig. 4-5 Probe only spectra

(a) Raw probe-only spectra (b) Normalized Probe-only spectra

the two photon absorption of the pump beam by the carriers, which is discussed later in section 4.9.

While the multiphoton photoemission spectra can be used to identify the bulk bandedge position, the photovoltage shift in the spectrum can make it complicated to determine the position of the bulk bandedge of semiconductors in laser photoemission experiments. The photovoltage shift occurs due to the band flattening at the semiconductor surface under light irradiation [64]. It manifests itself as a finite shift between the probe-only spectrum and the pump-and-probe spectrum. In the current experiment, no noticeable shift has been observed between the probe-only spectrum and a pump-and-probe spectrum. The absence of the photovoltage shift on Si(100)2x1 is in good agreement with the results of reference [17] and [18].

When the sample is irradiated with the 800 nm beam, a finite number of electrons are generated through a multiphoton photoemission process of the pump beam. But, in general, the number of electrons generated via multiphoton photoemission of the pump beam from a clean Si(100) surface is much lower than that of the probe beam.

4.4 Pump-and-probe time-resolved spectrum

The present section discusses the time-resolved spectra taken from a clean p-type Si(100)2x1 surface (sample #1). The electron yield per laser pulse increases with the pump beam fluence due to an increased optical pumping of the carriers above the bandgap. The space charge broadening of the electron energy spectrum sets an upper limit to the pump beam fluence and probe beam fluence. As shown in section 3.2, space

charge broadening manifests itself as a shift or broadening of the energy spectrum especially towards the high energy tail of the spectrum as the number of electrons collected per shot is increased. Therefore, the absence of the space charge broadening is experimentally verified by taking spectra at several probe beam intensities and comparing corresponding spectral features. The space charge broadening depends on the beam spot size and on the number of electrons extracted. With the probe beam diameter of 1 mm and collection efficiency of 3 counts per laser shot, the estimated amount of the space charge broadening is not greater than 50 meV as shown in section 3.2. In actual experiments, the pump fluence level is kept below a few mJ/cm^2 to avoid space charge broadening while keeping a reasonable signal-to-noise level.

Fig. 4-6 (a)-(f) shows the time-resolved spectra at six different time delays: -1.8 psec, -0.47 psec , -0.2 psec , 0.0 psec , 0.4 psec, and 3.2 psec. The bias on the sample is -1.73 V. Both the pump beam and the probe beam are p-polarized. The position of the conduction band minimum is determined by the method mentioned in 4.3. The energy scale is referenced to the bulk conduction band minimum. Negative time delays mean the probe beam is incident on the sample earlier than the pump beam. At a sufficient negative time delay, for example, T = - 1.8 psec in Fig. 4-6, the probe beam probes the sample in its ground state. The photoemission spectrum at T = -1.8 psec is the sum of the probe-only spectrum and pump-only spectrum. It can be considered as a constant background and it must be subtracted from the spectra taken at different time delays to extract the "two-color" signal. The subtraction procedure puts a severe limit on the signal-to-noise ratio in the experimental data due to long-term drifts in the laser power or pulsewidth. If the background spectrum is taken only at the start or at the end of the run,

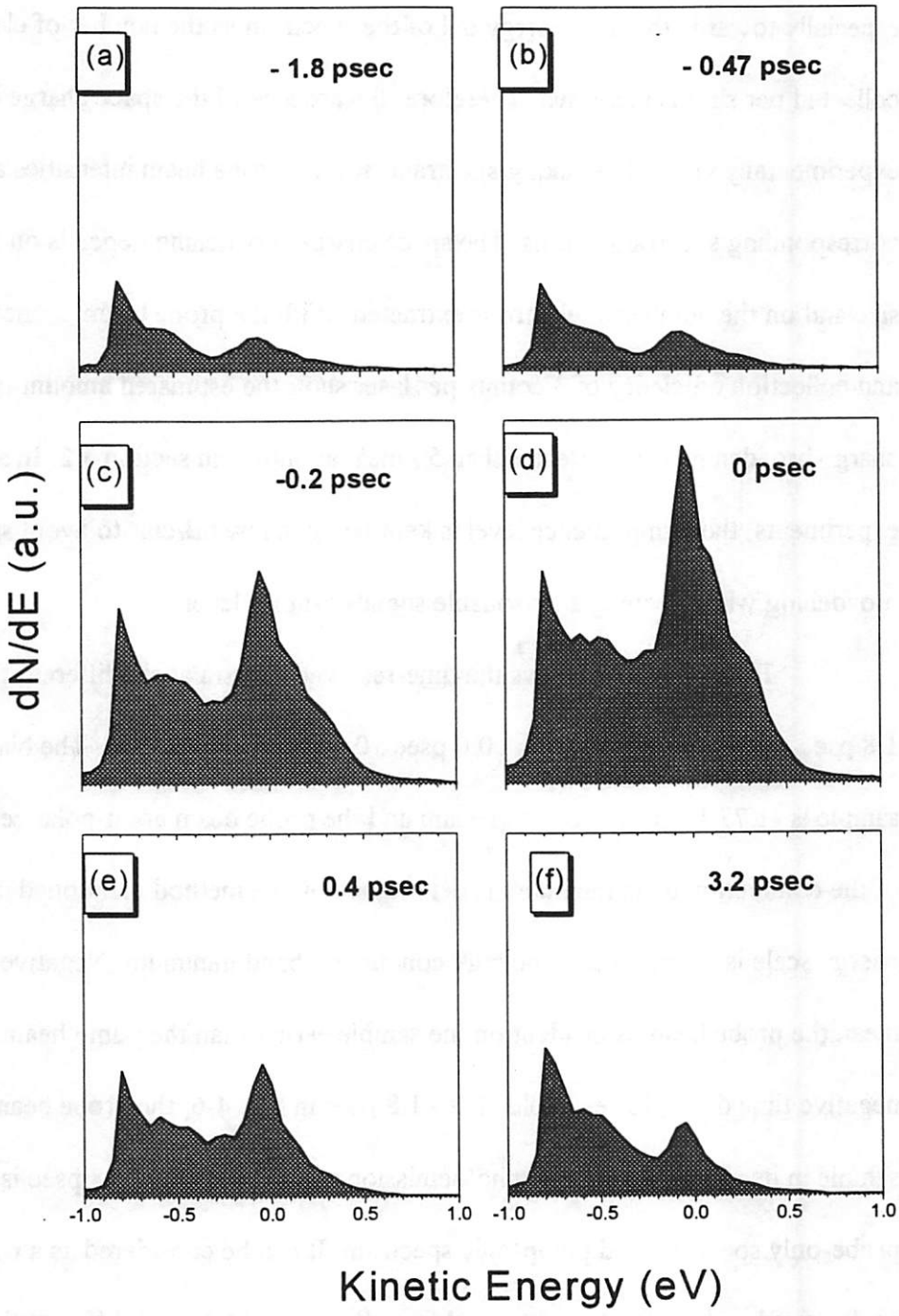

Fig. 4-6 Time-resolved spectra

the subtraction procedure may result in a poor signal-to-noise ratio and sometimes negative counts. Therefore, the background spectrum is taken several times in the course of the actual experiment and it is averaged together to obtain a reasonable background spectrum to be subtracted.

Fig. 4-7 shows the difference spectra where the background spectrum is subtracted from the corresponding spectrum at each time delay. The energy scale is referenced to the conduction band minimum. At T = 0.0 psec at which the probe beam temporally overlaps with the pump beam, there is an appreciable yield increase especially at kinetic energies from - 0.8 eV to 0.5 eV. Particularly noteworthy is that there are strong emissions from the states inside the bulk bandgap as observed by other researchers [17], [18]. This is due to the surface sensitivity of the photoemission process. Furthermore, there is another effect which makes the surface state more visible than the bulk states [17]. From the bulk band structure of silicon as shown in Fig. 4-8 [65] , there is no state above the vacuum level that can be connected from the states at the conduction band minimum of silicon (X valley) by a direct transition involving a 4.66 eV photon. In other words, if the electrons in X conduction valley are to be observed in photoemission, the transition has to be an indirect transition involving a phonon for crystal momentum conservation. On the other hand, the crystal momentum conservation condition is relaxed for the surface states in the direction normal to the sample. The transitions from surface states do not necessarily involve phonons, which enhances the transition probability.

In Fig. 4-9, the electron yields at selected energy positions are displayed in a logarithmic scale as a function of the time delay to show the dynamic feature more

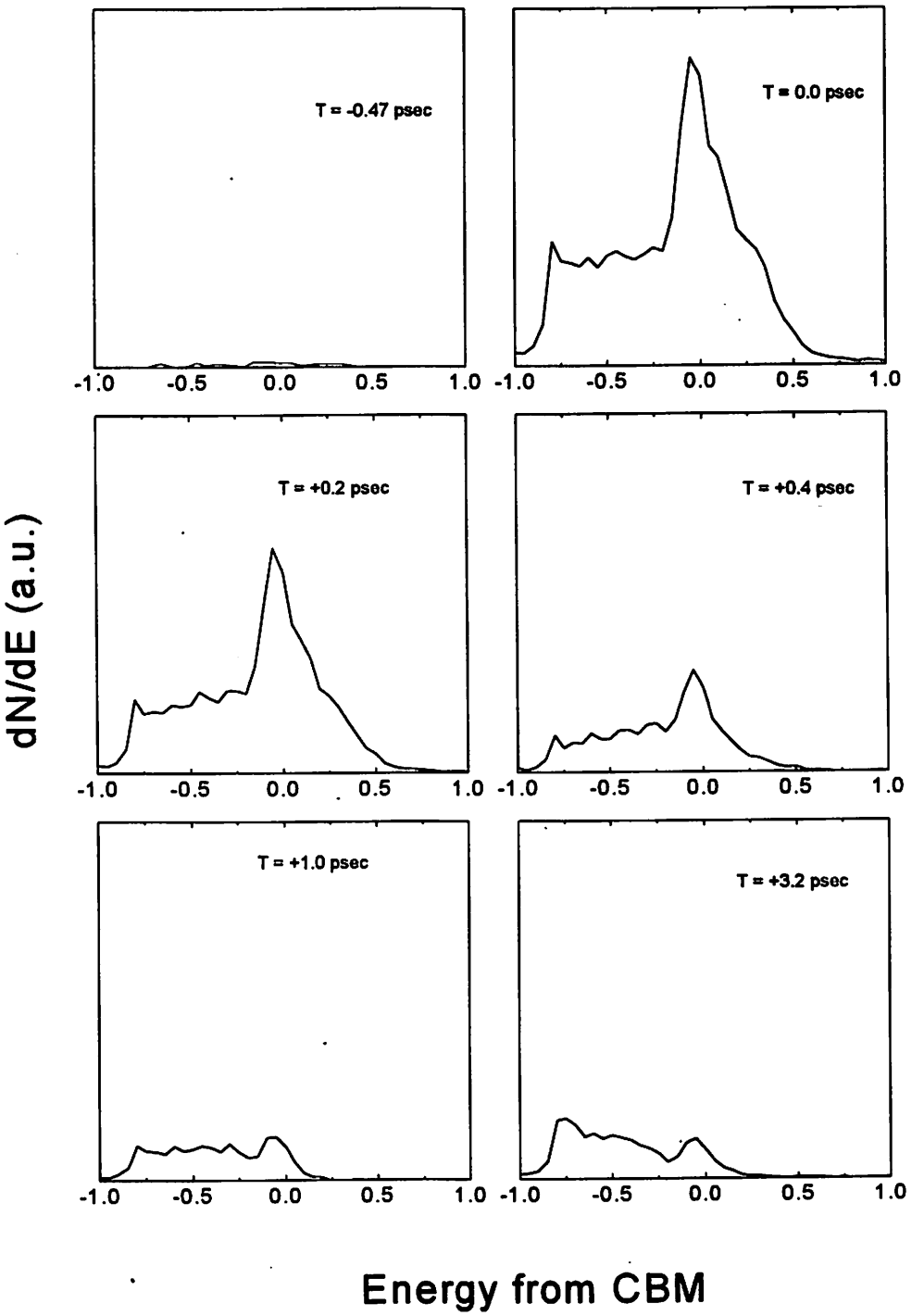

Fig. 4-7 Difference spectra

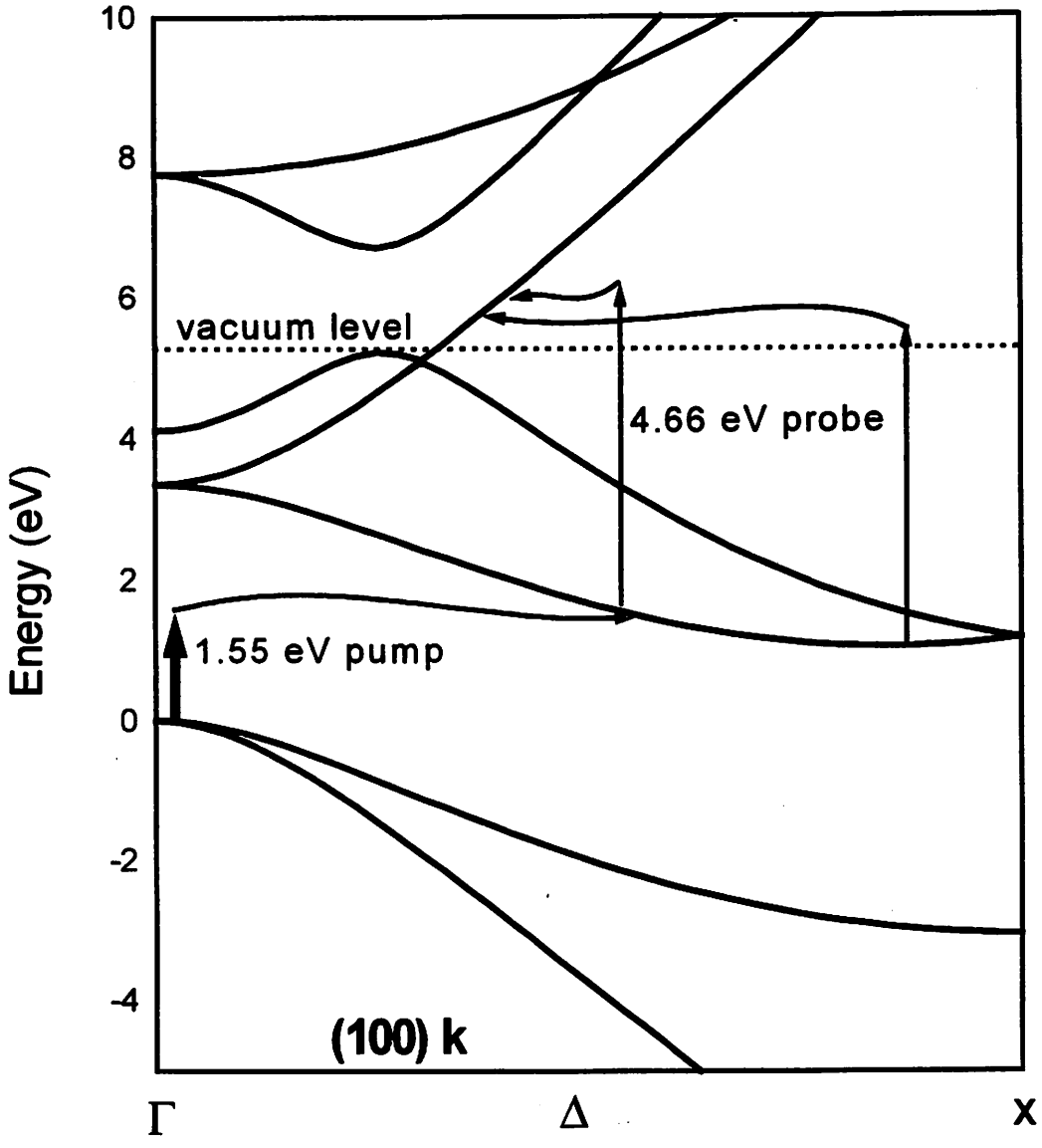

Fig. 4-8 Bulk bandstructure of silicon

clearly. The energy position is referenced to the bulk conduction band minimum. The background spectrum has already been subtracted. At 0.5 eV above the conduction band minimum, the yield follows the laser temporal profile because the relaxation time is short for those states due to a large phase space for relaxation [66]. For states around and below the conduction band minimum, there is also a rapid rise following the laser profile. There is a rapid decrease in yield after T = 0.0 psec, and this rapid decrease is followed by a slow decrease in yield at longer time delays. At 0.8 eV below the conduction band minimum, the yield starts increasing after T = 1 psec, due to the accumulation of electrons into these states.

A rapid decay in electron yield followed by a slow decrease has also been observed by authors of reference [17] on a Si(100)2x1 surface. The fast decay was attributed to a fast relaxation inside the upper intrinsic surface states by authors of reference [17]. To interpret the observed fast decay around the conduction band minimum, identifying the nature of the states that are observed in the time-resolved photoemission spectra is crucial. Especially, the nature of the peak just below the conduction band minimum and that of the states above the conduction band minimum have to be identified. For this purpose, experiments are designed involving varieties of Si samples and they are discussed in the next two sections.

4.5 Spectrum from a single domain Si surface

In the previous section, the pump-and-probe spectra showed a pronounced peak just below the conduction band minimum. Assuming that the electron affinity of Si(100) surface is 4.0 eV [17], the maximum transverse momentum that can be probed

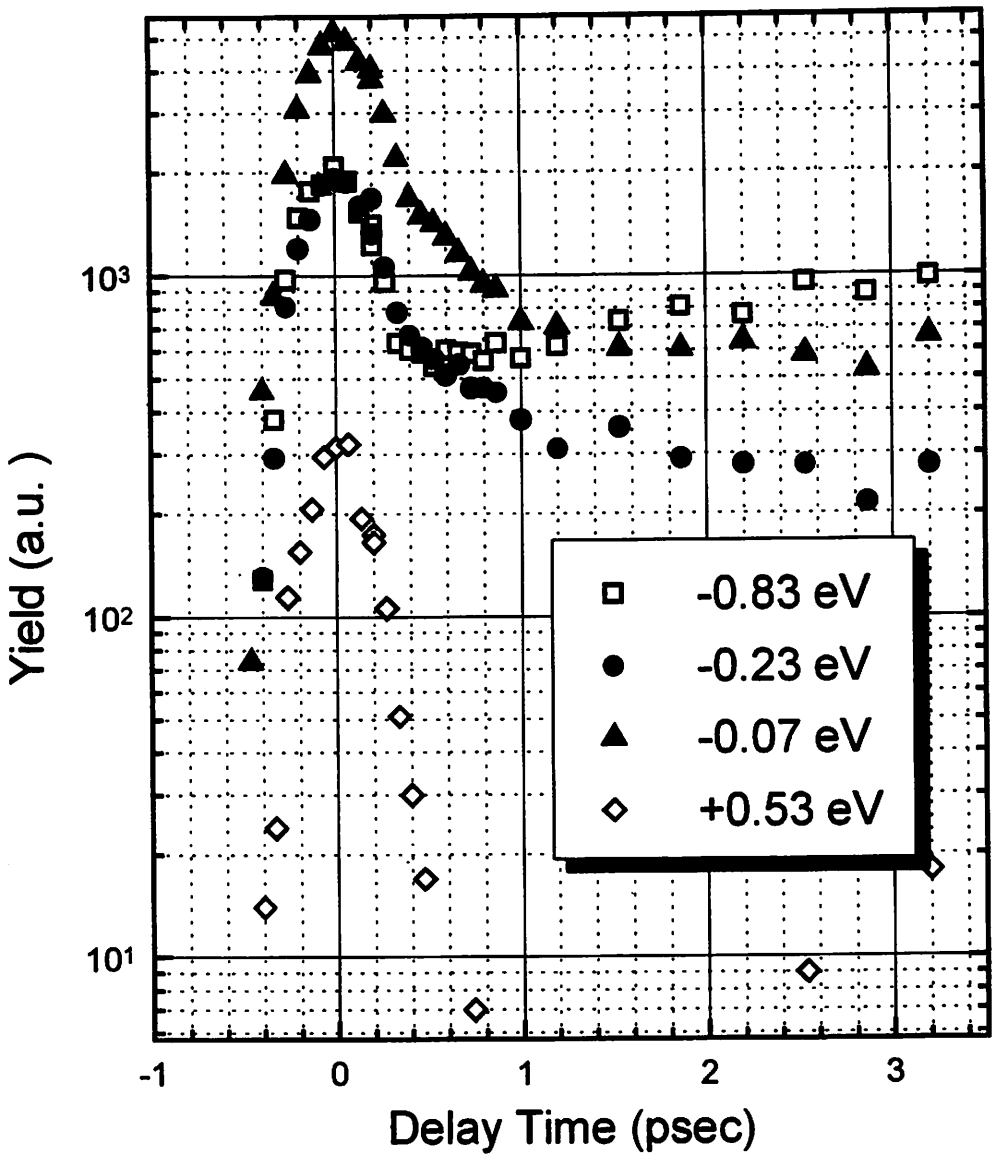

Fig. 4-9 Yield vs time delay

with a 4.66 eV photon is estimated to be 0.36 $Å^{-1}$ for the energy position of the observed peak. It is not large enough to reach the J' point of the surface Brillouin zone of the Si(100)2x1 surface where the band dispersion is greatest [59]. Therefore, the experimentally observed peak is located near the Γ point of the surface Brillouin zone. It is quite possible that the peak that is being observed in time-resolved spectrum is the same state observed by authors of reference [58] at the Γ point of the surface Brillouin zone of the Si(100)2x1 surface in their photoemission and inverse photoemission study. They attributed the peak to the states associated with defects on the Si(100)2x1 surface.

Whether the peak is an intrinsic surface state associated with 2x1 reconstruction or a state associated with a defect can be resolved by studying the symmetry property of the state. Photoemission spectroscopy is a powerful technique for studying the symmetry properties of surface states or adsorbate-induced states [10]. The principle of symmetry requires that the matrix element for the transition probability in photoemission should remain invariant under the symmetry operations of the system under investigation. For example, suppose Si dimers have been formed in such a way that the dimer row is parallel to the optical table, as depicted in Fig. 4-10. The Si dimer itself is perpendicular to the optical table. The plane which bisects the dimer becomes a mirror symmetry plane and it is parallel to the optical table. The transition probability can be written as

$$P \propto \left| \langle \psi_i | \vec{p} \bullet \hat{e} | \psi_f \rangle \right|^2 .$$

From the symmetry principle, the matrix element has to remain invariant under the reflection with respect to the mirror plane. For a photoelectron to be detected in the

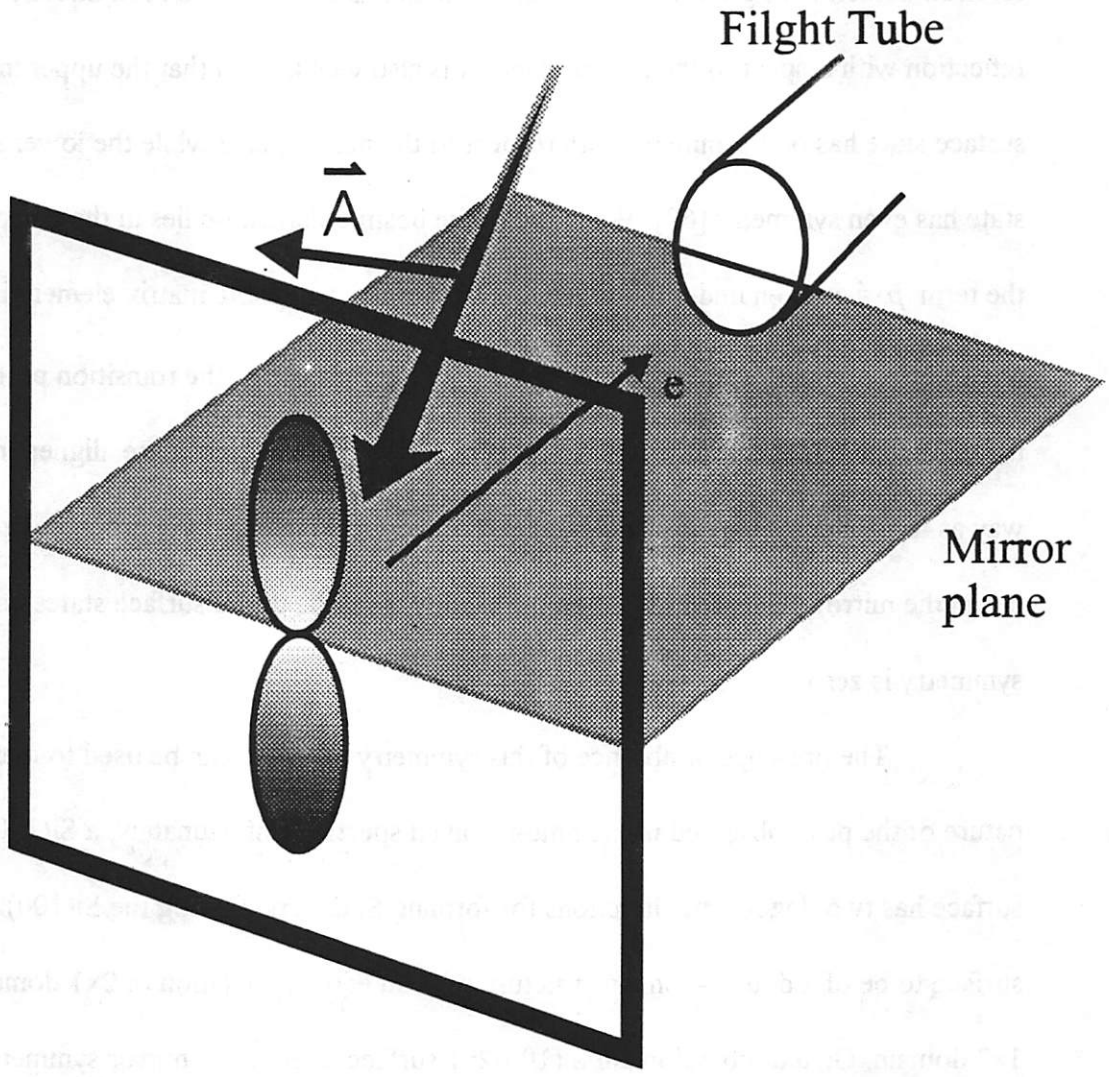

Fig. 4-10 Symmetry property in photoemission

electron detector lying on the mirror plane, the final state has to be even under the reflection with respect to the mirror plane. It is also well known that the upper intrinsic surface state has odd symmetry with respect to the mirror plane while the lower surface state has even symmetry [67]. When the probe beam polarization lies in the mirror plane, the term $\vec{p} \cdot \hat{e}$ is even under the reflection. Therefore, the whole matrix element is odd under reflection with respect to the mirror plane. It means that the transition probability for this process is identically zero. In other words, when the dimers are aligned in such a way as to produce a mirror plane parallel to the optical table and the probe polarization lies in the mirror plane, the transition probability from the upper surface states with odd symmetry is zero.

The presence or absence of this symmetry property can be used to identify the nature of the peak observed in the time-resolved spectra. Unfortunately, a Si(100)2x1 surface has two degenerate directions for forming Si dimers, forcing the Si(100)2x1 surface to be of a double-domain structure with an equal population of 2x1 domain and 1x2 domain. On a double-domain Si(100)2x1 surface, there is no mirror symmetry plane because the dimer direction is perpendicular to each other in different domains.

One way to overcome the difficulty is to use a single-domain Si(100)2x1 sample. As explained in section 4.2, a single domain 2x1 surface can be made from a Si wafer with a miscut greater than 4 degrees with respect to the (100) direction. For the experiment, a single domain surface has been prepared from a low doped n-type sample with 9 degrees miscut by the standard cleaning method discussed in 2.3. After the cleaning, the Si dimers are formed with their axis perpendicular to the optical table. The

fact that the sample is composed of a single domain is verified by the LEED patterns *with missing half integral spots in one direction*. In the time-resolved pump-and-probe photoemission experiment, the probe beam polarization is made to lie on the plane parallel to the optical table which serves also as a mirror plane. Even with p-polarization of the probe beam, the peak below the conduction band minimum is observed in the time-resolved spectra. In fact, the shape of the spectrum and its dynamics are the same as observed in the double domain surface. It leads to the conclusion that the states just below the conduction band minimum cannot be the intrinsic surface states that arise from the 2x1 reconstruction. It corroborates the assignment of the peak at the Γ point of SBZ around the conduction band minimum to a surface defect state as in UPS and IPS study on a Si(100) 2x1 surface performed by authors of [58] and [60].

4.6 Spectrum from a heavily doped n-type sample

The assignment of the peak below the CBM to a defect related structure on the Si(100)2x1 surface can be given further support by showing that this state can be observed via one photon photoemission from a heavily doped n-type sample as was done in reference [58]. In a heavily doped n-type type sample, the bulk Fermi level moves close to the conduction band minimum. The surface states close to the conduction band minimum are occupied with electrons, if there is no strong surface Fermi level pinning, which is the case for Si(100) sample as confirmed by the absence of the photovoltage shift. When the state is occupied by electrons, it can be observed with one photon photoemission with a 4.66 eV probe beam.

In this section, the time-resolved two photon photoemission experiment on a heavily doped n type sample (sample 3) is discussed. The resistivity of the sample provided by the manufacturer is less than 0.02 $\Omega \cdot cm$ with Sb as dopants. The doping density estimated from the manufacturer-provided resistivity data is greater than $2 \times 10^{18} cm^{-3}$.

Fourteen spectra are taken from the sample with different intensities of the 4.66 eV beam. The photon peak count is assumed to be proportional to the intensity of the 4.66 eV beam. Fig. 4-11(a) shows the spectrum with the highest photon peak count (917 counts) and the spectrum with the lowest photon peak count (151 counts). The ratio of the photon peak count is 6.1. The bias on the sample is -1.842 V and the energy scale is referenced to the conduction band minimum. At each energy position, the electron yield can be plotted with the photon peak counts and the relation of yield vs photon peak height can be fitted with a power law. The optimum exponent at each energy position is shown in Fig. 4-11 (b). Clearly, the electrons at high energy are generated from the two photon absorption of the probe beam. The yield around the conduction band minimum shows less than quadratic dependence on the probe beam intensity. It shows that the electron yield around the peak is a mixture of one-photon photoemission and two-photon photoemission.

To determine the relative strength of the one-photon photoemission process and the two-photon photoemission process around the peak region, the electron yield at each energy position is fitted with respect to the probe beam intensity with the following relation

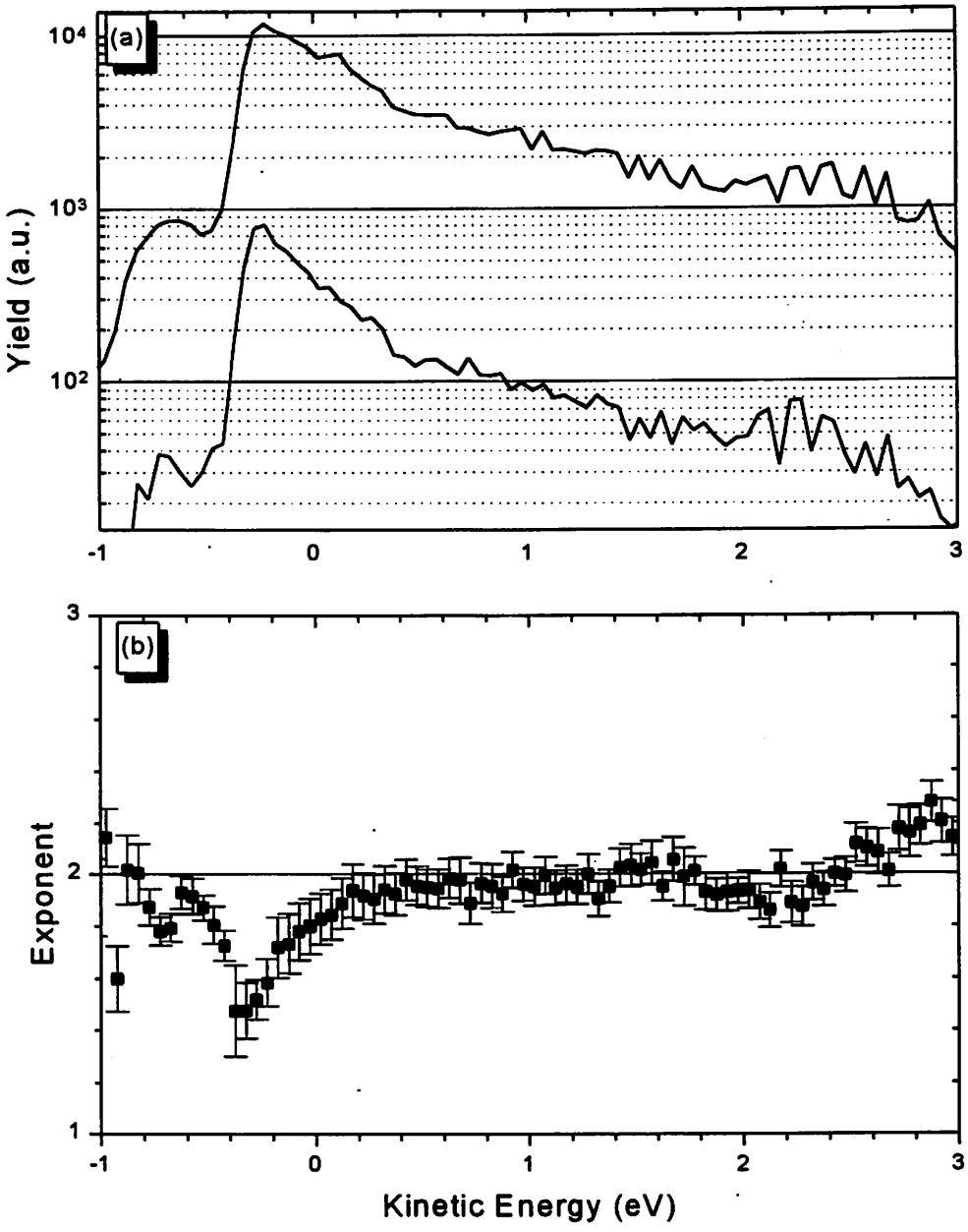

Fig. 4-11 (a) Spectra with 266 nm only from n+ sample with two different laser intensity

(b) Optimum exponent at each energy position

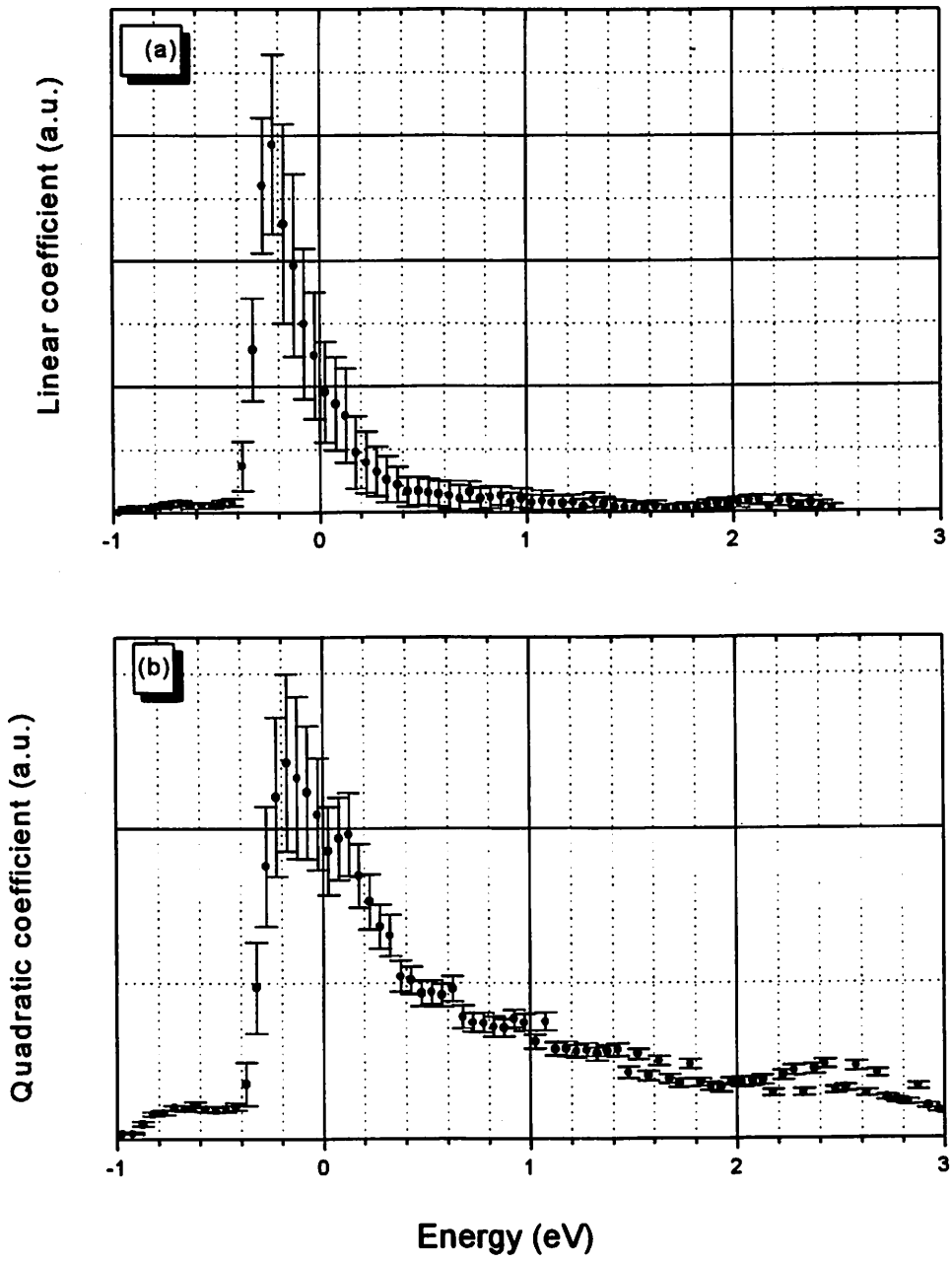

Fig. 4-12 (a) One-photon photoemission coefficient (b) two-photon photoemission coefficient

$$Y = AI + BI^2.$$

A is the one-photon photoemission coefficient and B is the two-photon photoemission coefficient. The best-fit values of coefficients A and B at each energy position are displayed in Fig. 4-12. The yield around the peak cannot be well fitted with the above expression, which is manifested by the relatively large size of the error bars. The reason is because one-photon photoemission and two-photon photoemission occur at the same time, giving rise to complications due to the simultaneous population change.

Fig. 4-13 shows the pump and probe spectra taken from the heavily doped n-type sample at T= 0.0 psec and T = - 4.0 psec. The spectrum at T = 0.0 psec has a contribution from optically generated carriers plus the free carriers due to the bulk doping of $2 \times 10^{18} cm^{-3}$ or greater. However, the spectrum at T= -4.0 psec has the contribution only from the bulk doping. The two spectra merge approximately at 0.9 eV. The two-color signal occurs only at energy positions of 0.9 eV or below. At the energy position of - 0.3 eV where the peak occurs, the two photon photoemission yield at T = 0.0 psec is about 13 times greater than that of T = - 4.0 psec spectrum. The photogenerated carrier density with an irradiation of an 800 nm beam with the fluence level of 1 mJ/cm^2 is approximately $3 \times 10^{18} cm^{-3}$, which is comparable to the bulk doping level of the sample. The fact that the spectrum at T = 0.0 psec shows 13 times greater peak strength than that of T= -4.0 psec can be interpreted as a strong enhancement of the optical absorption at the defect site compared with the bulk. This kind of optical enhancement is not unreasonable at all because the atomic arrangement at the surface is different from that of the bulk and the optical and electrical property of the surface can be significantly different

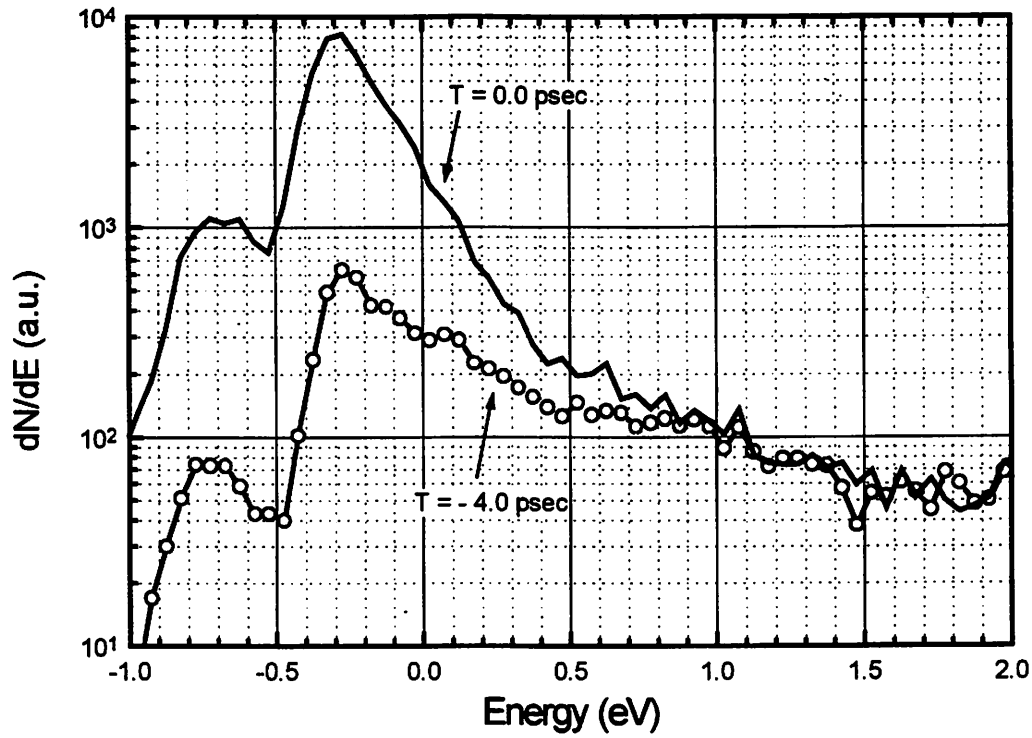

Fig. 4-13 Time-resolved spectra from n+ sample.

from those of the bulk. Surface-state induced optical anisotropy on the Si(100)2x1 surface is a well-known example [68].

4.7 Substrate temperature dependence

The nature of the optical transition involved in the photoemission process and the role of phonons in the carrier dynamics can be studied by investigating the photoemission spectra taken at different substrate temperatures [69]. Because the typical phonon energy is less than 50 meV [70], the change in substrate temperature modifies the equilibrium population of the phonon significantly. Therefore, any change in the photoemission spectra due to the phonon manifest itself as the substrate temperature is changed.

In this section, time-resolved photoemission experiments are performed on a clean silicon sample held at two different temperatures. The temperature of the sample is maintained at a constant level by flowing an appropriate amount of DC current through the electron-beam heater filament without applying any bias between the specimen plate and the electron-beam heater. The sample specimen plate is heated due to the radiation from the electron-beam heater filament. The voltage drop between the two ends of the filament is measured to be 5 V with the current of 1.8 A. It gives rise to a static electric field but it is shielded out by the sample specimen plate. By this method, the temperature of the sample can be varied from 300 K to 600 K.

Time-resolved photoemission spectra are taken at 600 K and 300 K from a sample of light n-type (sample #2). Fig. 4-14 (a) shows the spectra at T = - 4.0 psec and Fig.4-14(b) shows the two-color signal at T = 0.0 psec for two different substrate

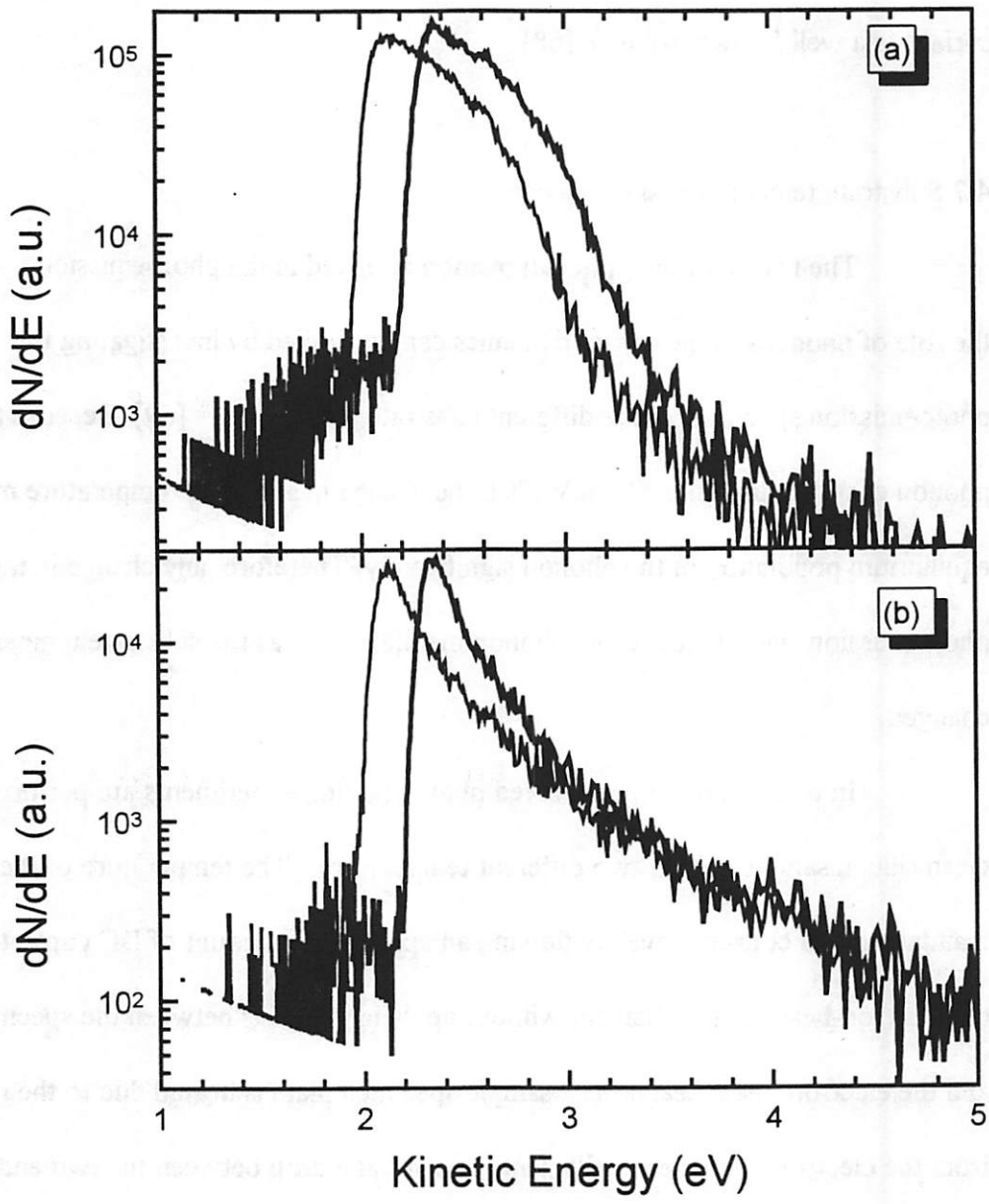

Fig. 4-14 Spectrum at two different temperature (a) T = 0 psec (b) T = -4.0 psec

Thick line : 600 K Thin Line : 300 K

temperatures. A uniform horizontal shift of magnitude 200 meV is observed between spectra taken at two different substrate temperatures for both time delays. The uniform energy shift is due to the Fermi level shift of the sample at two different temperatures. The Fermi level of the sample at 300 K is estimated to be located at 0.37 eV below the conduction band minimum for the given doping level [70]. When the sample is heated to 600K, thermally generated intrinsic carriers dominate the carrier statistics and the bulk Fermi level is placed approximately at the mid-gap region. Because the Fermi level of the sample is aligned with that of the sample specimen plate, the band edge is shifted upward, resulting in upward shift of the spectra at high temperatures. The amount of the shift agrees well with the estimate of the Fermi level shift at two different temperatures.

The spectra at negative time delays and T = 0.0 psec are similar in their magnitude and spectral shape. Fig. 4-15 shows the magnitude of two-color signal as a function of the time delay between the pump and probe for the two temperatures. The magnitude of two-color signal is defined as the total number of electrons at each time delay minus the number of background electrons. The magnitude of two-color signal is almost the same for early time delays regardless of the substrate temperature, while it shows an appreciable difference at longer time delays. The fact that the T = 0.0 psec spectrum is independent of the substrate temperature suggests that the phonon is not involved either in the carrier generation process or the photoemission process itself.

In Fig. 4-15, the electron yield at 600 K is higher than that at 300 K at time delays longer than 0.5 psec. It can be explained by a coupling between the bulk states and the defect states that is being observed. It is well known that the optical absorption

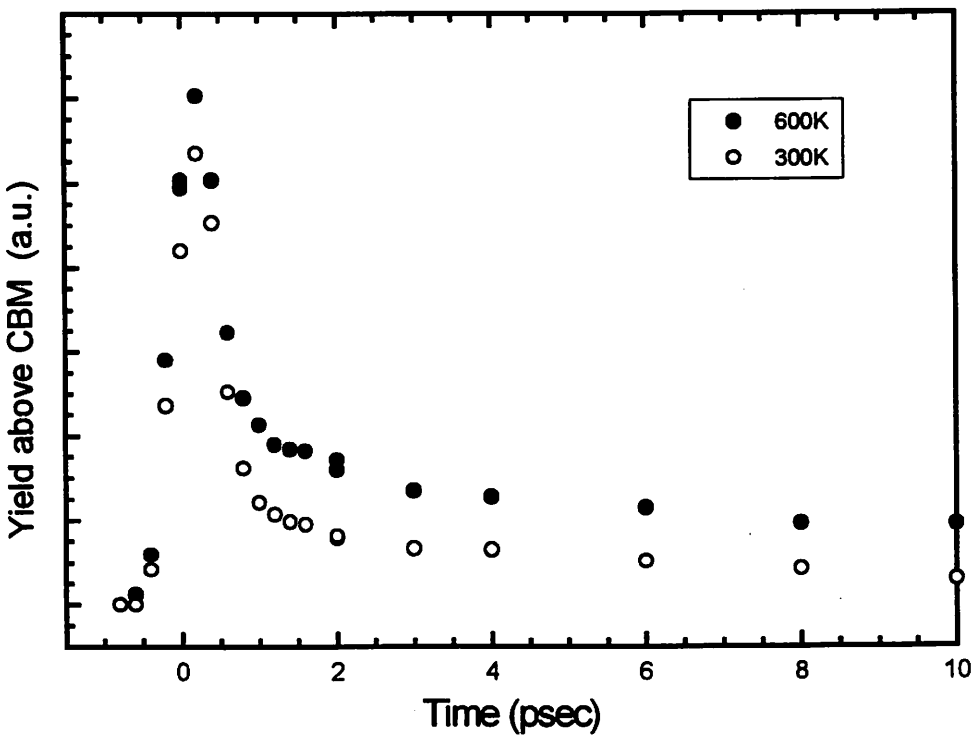

Fig. 4-15 Magnitude of the two-color signal

coefficient increases as the substrate temperature is increased [71]. There is little doubt that the density of carriers generated in the bulk at the substrate temperature of 600 K is approximately twice as large as that of 300K. The coupling between the defect states and the bulk states should establish a balance of the carrier density between those two states at sufficiently long time delays. Therefore, the carrier density at the defect site will be balanced at the level proportional to that of the bulk carrier density at sufficiently long time delays.

4.8 Electron temperature

In the previous sections, it was pointed out that the pronounced peak just below the conduction band minimum is a defect-related state and that there is a strong optical enhancement at that state. From the comparison of the spectra taken at two different substrate temperatures, it was also shown that there exists a coupling between these defect-related states and the bulk states. Due to the optical enhancement at the defect site, the carrier density generated at that site is much higher than that of neighboring sites or that of the bulk. The excess carriers at the defect site transport to neighboring sites or into the bulk of silicon. The transport of carriers appears as the fast decay of the two-color signal after T = 0.0 psec and it continues until the carrier density at the defect site becomes comparable to the bulk carrier density, resulting in the plateau of the carrier density at time delays longer than 0.7 psec. The plateau of the carrier density is achieved through the carrier exchange process between the bulk and the defect states as shown in section 4.7.

Along with a fast carrier transport out of the defect states into neighboring sites, the shape of the electron energy distribution also changes on a very short time scale. Fig. 4-16 displays the carrier distribution above the conduction band minimum for six different time delays (- 0.2 psec, 0.0 psec, 0.2 psec, 0.4 psec, 0.6 psec, and 3.2 psec). To quantify the change in the shape of the electron energy distribution, the electron energy distribution can be fitted with the expression

$$f(E) = A^* \exp\left(-\frac{E}{k_B T^*}\right)\sqrt{E}.$$

with A and T as fitting parameters. E is the kinetic energy of electrons referenced to the conduction band minimum and the density of states is assumed to be proportional to the square root of the energy.

The best fit electron temperatures are shown in each of the graph. The corresponding Maxwell-Boltzmann distributions are shown with solid lines while the experimental data are shown as discrete points. At T = - 0.2 psec and T = 0.0 psec delay, the experimental data do not exactly fall on the solid lines: there are excess electrons below 0.5 eV and fewer electrons above 0.5 eV. This is because 0.5 eV is the one photon absorption cut-off. In other words, 0.5 eV is the maximum kinetic energy an electron can acquire when an electron-hole pair is generated by absorption of a single 800 nm photon. Fig 4-16 (a) and (b) show that the electron energy distribution is not a thermal one at T = 0.0 psec or earlier. At positive time delays, the carrier-carrier scattering starts distributing the kinetic energy among carriers and the nonthermal feature smoothes out. After T = 0.4 psec, the dots fall on the best-fit Maxwell-Boltzmann energy distribution except a few

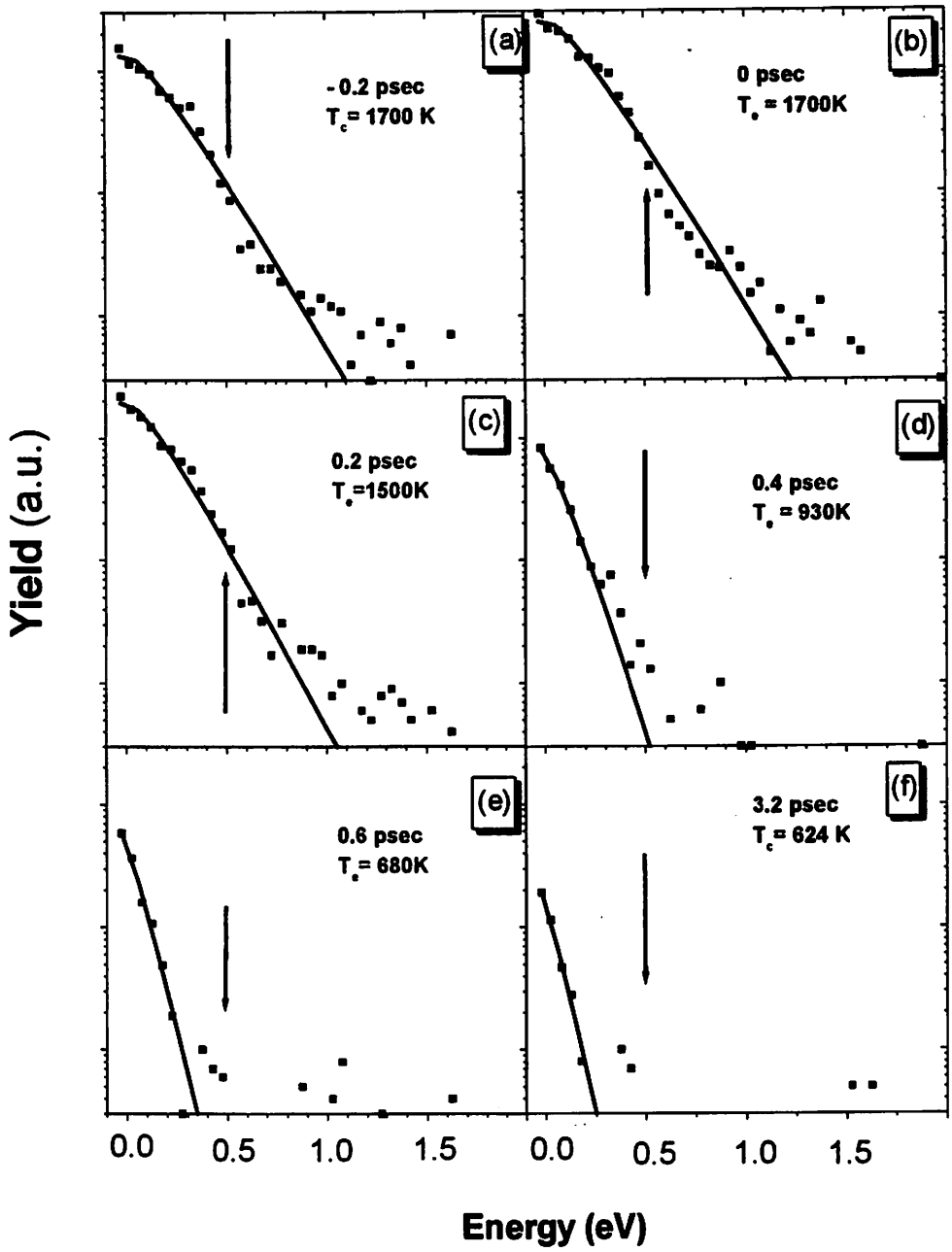

Fig. 4-16 Electronic distribution function above the conduction band minimum

noisy points at high kinetic energies.

The fact that carrier-carrier scattering smoothes out a non-thermal distribution by distributing kinetic energy among carriers can also be seen in a Monte-Carlo simulation of carrier dynamics in Si [72]. However, authors of reference [18] observed only thermal distributions inside the silicon sample, even though their time resolution was better than that of the current experiment. One possible reason is that their pump photon energy was 2.0 eV. A 2.0 eV photon generates electron hole pairs with excess kinetic energy as large as 0.9 eV. The relaxation time for high kinetic energy carriers is extremely short, making it impossible to observe the one-photon absorption cut-off.

Aside from smoothening of the electron energy distribution , the electron temperature also changes as the time delay is increased. The electron temperatures extracted from the fit to the experimental data are displayed as a function of the time delay in Fig. 4-17. The peak temperature reaches 1700 K at T = 0.0 psec , which is in good agreement with the simple estimate based on the average kinetic energy of the photogenerated carriers. The electron temperatures at negative time delays are comparable to that of T = 0.0 psec. At negative time delays, the photogeneration is the dominant process, and the average kinetic energy of an electron is close to the value of $\hbar\omega - E_g$. Therefore, the electron temperature remains close to 1700 K at T < 0.0 psec. The electron temperature becomes stabilized at 600 K at time delays later than 0.7 psec. The reason why the steady state temperature is higher than 300 K is because the energy resolution of the detector is finite and the data spacing of kinetic energy in the experiment is 50 meV.

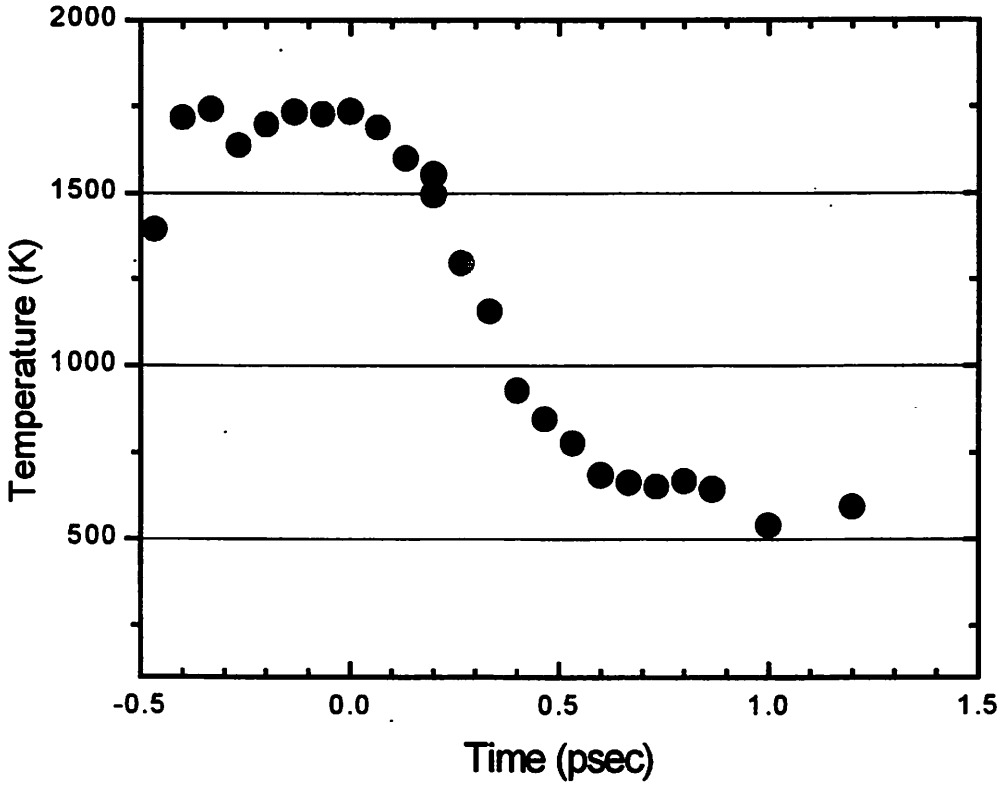

Fig. 4-17 Electron temperature as a function of delay time.

4.9 Various pump beam intensity spectrum

The electron energy distribution and the electron temperature can depend on the pump fluence incident on the sample. The relationship between pump fluence and the electron temperature can reveal the mechanism how the energy of the optical beam is transferred to the electrons. The current section discusses the time-resolved photoemission spectra taken at four different pump fluences : 0.44 mJ/cm^2, 0.6 mJ/cm^2, 0.74 mJ/cm^2, and 0.86 mJ/cm^2. The pump fluence is varied by a combination of a half wave plate and a polarizer as described in the section 2.1. The incident fluence is estimated from the total energy of the beam and the beam size. The beam size is determined by measuring the optical power as the size of the variable aperture is changed. The half-wave plate and polarizer combination is calibrated by measuring the transmitted power as the half-wave plate is rotated. Fig. 4-18 (a) shows the spectra at T = 0.0 psec for four different pump fluences in logarithmic vertical scale. For each spectrum, the corresponding background spectrum has already been subtracted. The horizontal energy scale is with respect to the conduction band minimum. At all pump fluences , the electron spectrum reaches far beyond the one-photon absorption cut-off which is 0.5 eV above the conduction band minimum.

At each energy position, the yield versus the pump fluence can be fitted with a power law dependence. The optimum exponent at each energy position is shown in the Fig. 4-18 (b). The error bar becomes greater at higher energy due to fewer electron counts. The yield depends linearly on the pump fluence at lower energies , which is indicated by the exponent close to 1.0. The yield varies quadratically with the pump

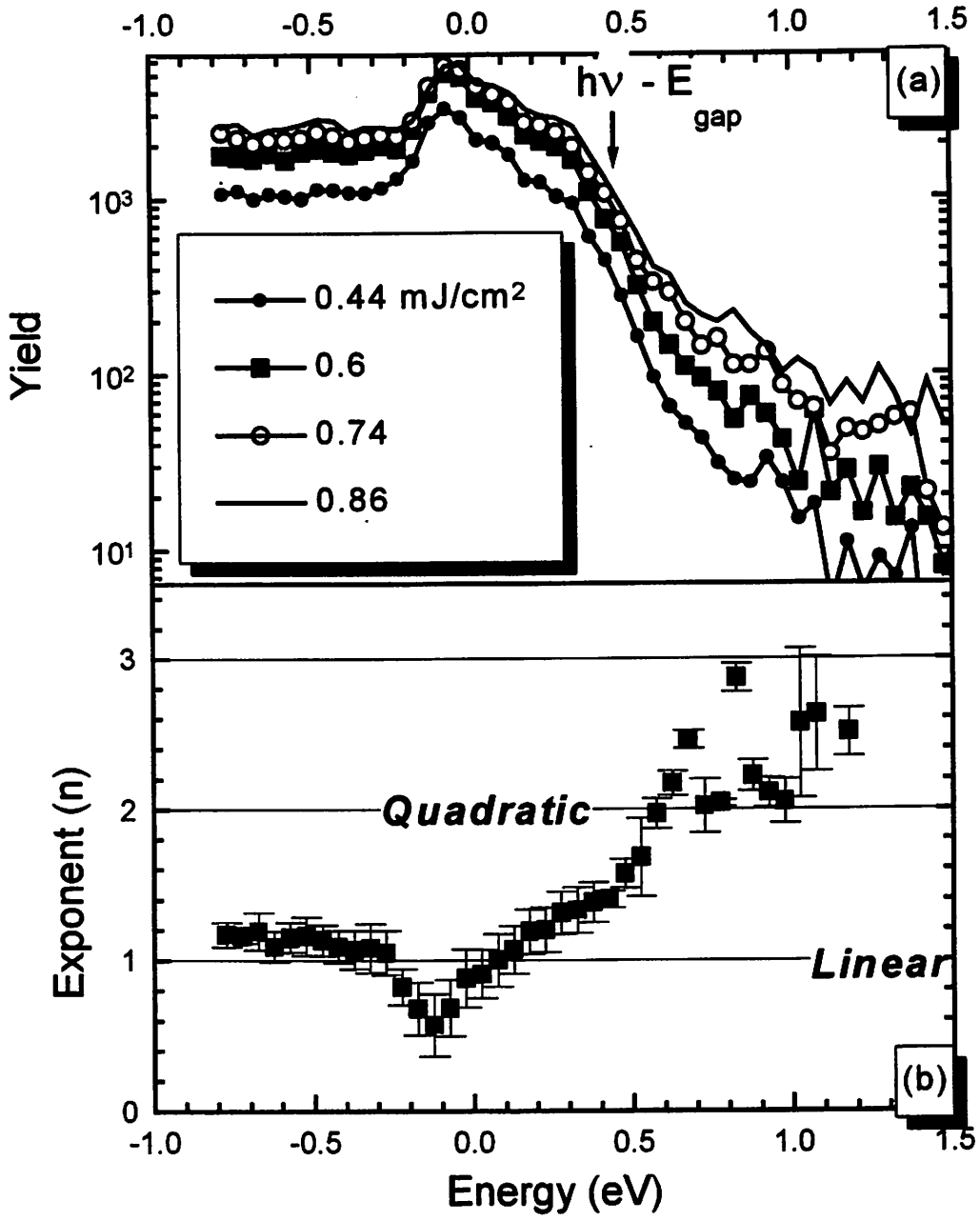

Fig. 4-18 (a) Electron distribution at T = 0.0 psec with four different pump fluence

(b) Optimum exponent at each energy position

fluence above 0.5 eV, which agrees well with the one-photon absorption cut-off. Therefore, the electrons with kinetic energy greater than 0.5 eV are generated with two photon absorption of the pump beam. The two photon absorption feature and the hot electron tail are clearly visible even at the lowest fluence 0.44 mJ/cm^2. The electrons with kinetic energy between 0.0 eV and 0.5 eV are generated partly via one-photon absorption and partly via two-photon absorption which is indicated by the exponent between 1.0 and 2.0.

Another interesting feature is a saturation below the conduction band minimum, which is indicated by the exponent less than one. The saturation occurs exactly where the electron energy distribution peaks. As a matter of fact, around the energy position of the peak, the data cannot be properly fitted with a power-law dependence. The saturation of the optical pumping at the peak of the distribution agrees well with the assertion that there is a strong optical enhancement into these states.

When two pump photons are absorbed for creating an electron hole pair, the excess kinetic energy imparted to the pair becomes as high as 2.0 eV per pair, compared to 0.5 eV for one-photon absorption process. Therefore, the electron temperature can reach appreciably higher temperature when two-photon absorption is included. The electron temperature also depends on the pump fluence if the two photon absorption is a dominant process. Fig. 4-19 shows the electron temperatures extracted from the experimental data at different pump fluences as a function of the time delay. The peak temperature occurs at T = 0.0 psec for all fluences and it depends on the pump fluence. It reaches 2100 K with the highest pump fluence (0.86 mJ/cm^2) while it is 1700 K for the

lowest fluence (0.44 mJ/cm^2). However, the temperature at T = - 0.5 psec does not depend on the pump fluence because the pump beam intensity at that time delay is so low that linear absorption is dominant. At all fluence levels, the electron temperature reaches a plateau in less than 0.5 psec.

4.10 Theoretical Model

Even though the density of photogenerated carriers undergoes a rapid change near the surface after T = 0.0 psec, the temporal change of the electronic temperature can be attributed to the energy transfer from the carriers to the lattice. The decay of electron temperature within 0.5 psec suggests that the carrier energy relaxation occurs on a time scale comparable to the pulsewidth of the incident laser.

In this section, a simple and illustrative theoretical model is presented to extract transport parameters such as electron energy relaxation time. The model should incorporate the electron temperature dependence on the pump fluence and the fast transport of carriers out of the defect state. The model is based on the two-temperature model which has been applied to explain the optical properties of silicon irradiated with picosecond laser pulses [73]. It consists of a set of balance equations: the continuity equation for the carrier transport, the laser beam attenuation, and energy balance equation for the carriers and the lattice. The equations used in reference [73] are displayed below for discussion.

$$\frac{\partial N}{\partial t} + \vec{\nabla} \cdot \vec{J} = G + R \quad \text{continuity equation}$$

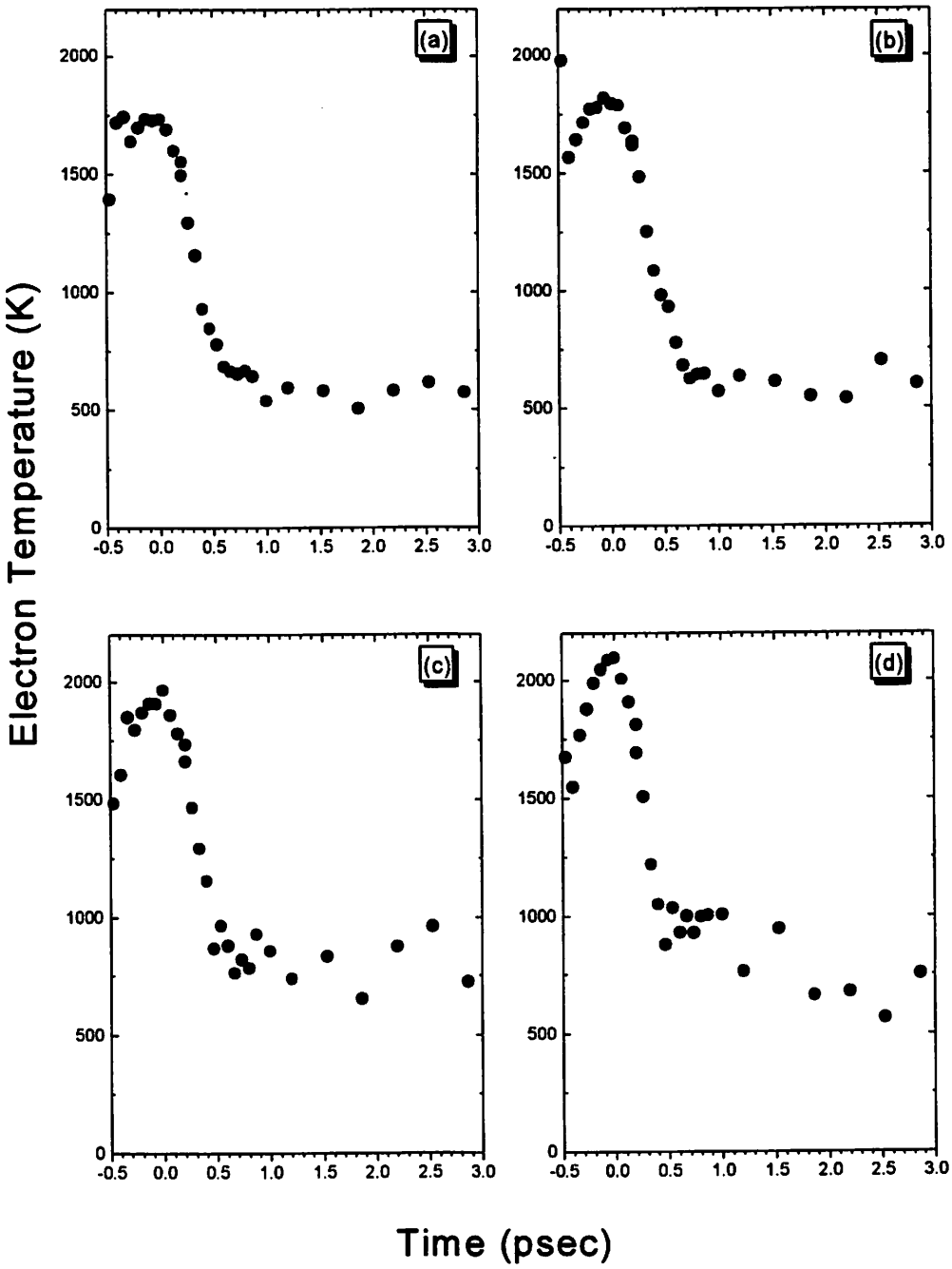

Fig. 4-19 Electron temperature at different pump fluence

$$\frac{dI}{dx} = -\alpha I - \beta I^2 - \Theta N I \quad \text{laser beam attenuation}$$

$$\frac{\partial}{\partial t} U + \vec{\nabla} \cdot \vec{W} = S_U - L_U \quad \text{carrier energy balance}$$

$$\frac{\partial T}{\partial t} = C_L \vec{\nabla} \cdot \kappa_L (\vec{\nabla} T) - L_U \quad \text{lattice heat diffusion}$$

N : carrier density , $\vec{J}$: current density, G : generation rate , R : recombination rate

I : intensity of the laser, α : linear absorption coefficient, β : two photon absorption coefficient, Θ : free carrier absorption cross section

U : carrier energy density, $\vec{W}$: ambipolar energy current

S_U : source of the total carrier energy from the laser beam

L_U : loss of carrier energy to the lattice

In reference [73] , it was assumed the carriers reach a quasi-equilibrium among themselves which is characterized by a single carrier temperature. This assumption is not strictly true for the time scale that is being discussed in this thesis because a nonthermal electron energy distribution is observed at time delays close to T = 0.0 psec. However, to provide a starting point for the theoretical modeling of the ultrafast carrier dynamics in silicon, it is assumed that the carrier distribution can be described by a single quasi-thermal electron temperature T_C. Based on this assumption, the carrier energy density and the loss rate of the carrier energy to the lattice can be expressed as

$$U_C = N(E_g + 3k_B T_C), \text{ and}$$

$$L_U = \frac{3Nk_B}{\tau_c}(T_C - T_L) \text{ respectively.}$$

τ_c is the carrier energy relaxation time. Furthermore, it is assumed that the lattice temperature change can be neglected on the time scale of interest and it can be taken to be 300 K. This assumption is valid as the lattice temperature rise is negligible compared to the electron temperature, as discussed in section 4.1 and Appendix 1. Because the absorption depth of the 800 nm pump beam is much greater than the probing depth of the 266 nm beam, the spatial dependence of the laser intensity due to photogeneration of carriers , the diffusion of carriers and the lattice heat diffusion are neglected.

Due to an optical enhancement and carrier transport to the neighboring sites or into the bulk states, the observed electron density decreases very fast. The electron transport is simulated by putting a term $-N/\tau_0$ in the continuity equation for the carrier density. The electron transports occurs with the transport of energy . To account for the energy loss accompanying the carrier transport, a term $-\frac{N}{\tau_0}(E_g + 3k_B T_C)$ is added to the energy balance equation. τ_0 is the time for the carrier transport and it can be determined from the plot of the density of the electrons above the conduction band minimum versus the time delay .

Based on these assumptions, the four partial differential equations used in reference [73] are reduced to two ordinary differential equations.

$$\frac{dN}{dt} = \frac{\alpha I + 0.5\beta I^2}{\hbar\omega} - \frac{N}{\tau_0}.$$

$$\frac{dU_C}{dt} = -\frac{3Nk_B}{\tau_C}(T_C - T_L) + \alpha I + \beta I^2 - \frac{N}{\tau_0}(E_g + 3k_B T_C).$$

These two ordinary differential equations are numerically solved to calculate the carrier density and the carrier temperature as a function of the time delay for different laser fluences. With an appropriate choice of the fitting parameters, reasonable fit with four different curves is achieved. The calculated electron temperature is displayed for four different fluences in Fig. 4-20 with the experimental data displayed for comparison. The fitting parameters for the solid lines in Fig. 4-20 are $\tau_C = 0.4$ psec , $\tau_0 = 0.2$ psec and $\beta = 120$ cm/GW. The value for β is approximately 3-5 times greater than the value expected based on the experimental data available at other wavelengths [74]. The difference might come from the uncertainty in the measurement of the laser fluence and the simplicity of the model itself. Considering the simplicity of the model, the value for τ_C is in reasonable agreement with the value of 0.27 psec obtained through a dc transport measurement on a short channel device[75] or with the value of 0.32 psec obtained with a Monte-Carlo simulator [75].

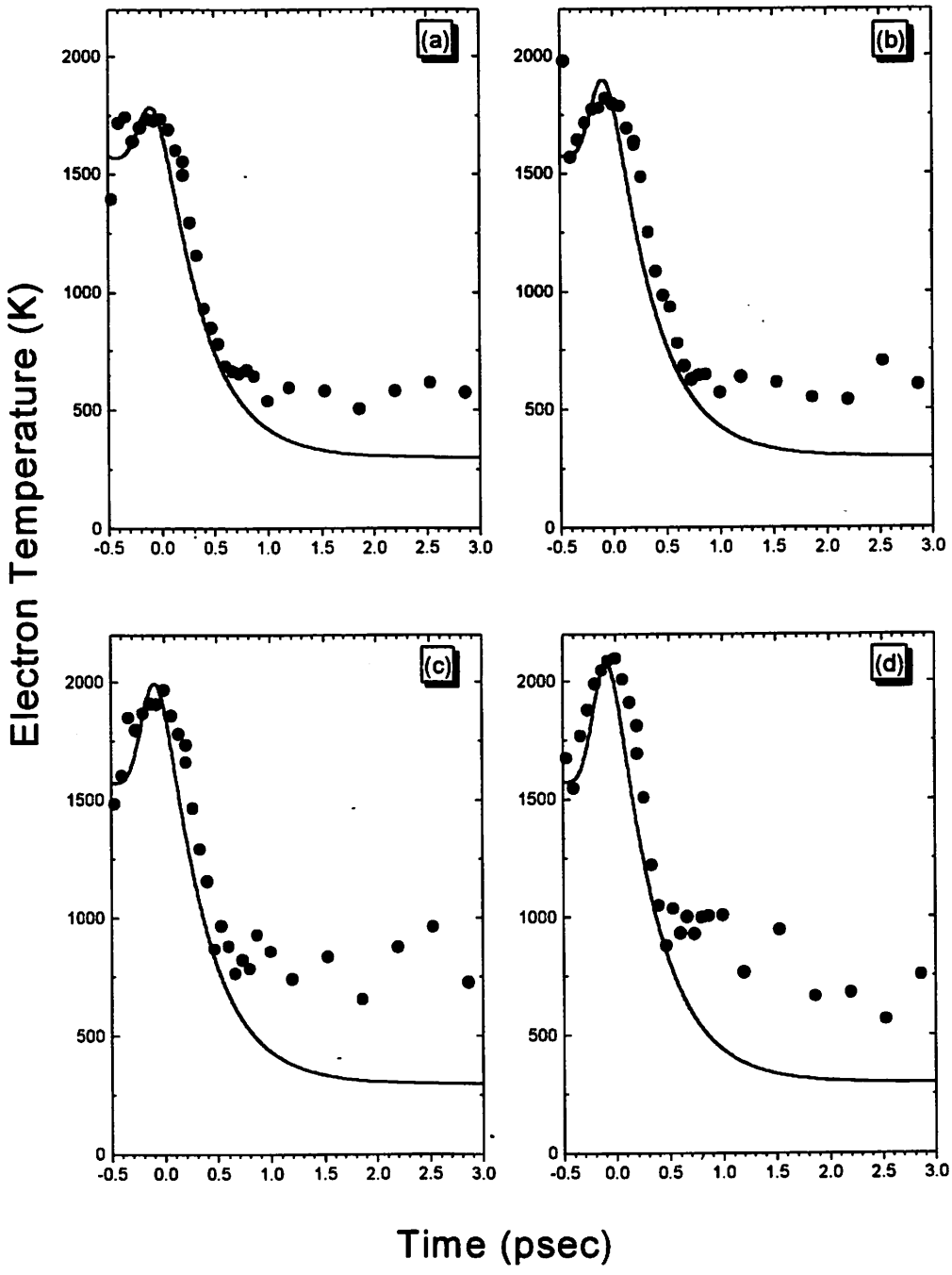

Fig. 4-20 Calculated electron temperature

Chapter 5. Conclusion

In previous chapters, the experimental study of hot electron dynamics in silicon using time-resolved two photon photoemission has been presented along with related experimental issues such as the third harmonic generation and space charge broadening. The group velocity dispersion inside the nonlinear crystal between the harmonics of the fundamental beam is the major limitation to the temporal resolution of the laser photoemission. A harmonic generator design involving a separate delay line to minimize the temporal broadening of the laser pulse was discussed. The space charge broadening of the electron energy spectrum is the major limitation to the energy resolution of the experiments at high pump fluences. An estimate of the average space charge broadening was made using a simple electrostatic argument.

With 266 nm as a probe beam, the photoemission spectrum from a clean Si(100)2x1 surface is dominated by emissions from the states lying inside the bulk bandgap. This is due to the finite probing depth (~ 5 nm), short electron inelastic mean free path and bulk electronic bandstructure of silicon. The electrons in the probe-only photoemission spectrum are generated via two-photon absorption of 266 nm photons, which can be verified experimentally by studying the probe beam fluence dependence of the electron yield. The two photon photoemission spectrum can be used to identify the position of bulk band edges.

With the sample excited by an intense pump beam (800 nm), the population of electrons and the shape of the electron energy distribution near the surface are shown to

change on a very short time scale. A pronounced peak has been observed near the bottom of the conduction band. The study of the symmetry properties of this peak revealed that it is associated with the surface defect states. From the study on a heavily doped n-type sample, it was shown that there is an enhanced optical transition into the defect state compared to the bulk optical transition. Also it was shown that the defect state exchanges carriers with bulk states on a very short time scale.

From the study of the carrier distribution at various pump beam fluences, it was shown that the pump beam photons are absorbed by carriers through one-photon absorption or two photon absorption. The two photon absorption is responsible for high kinetic energy electrons inside the conduction band. The energy relaxation time for these electrons is much shorter than the temporal resolution of the current experiment which is close to 100 fsec. The initial energy distribution of photogenerated carriers is observed to be nonthermal with the distribution cut-off at 0.5 eV above the conduction band minimum. It arises from the one-photon absorption cut-off. The carrier-carrier interaction smoothes out the one-photon absorption cut-off, bringing the nonthermal distribution to a thermal one. The thermalization occurs on a very short time scale comparable to the temporal resolution of the experiment.

The more gradual change in the shape of the electron energy distribution can be characterized by the change in its electron temperature, which can be determined by fitting the experimental data with a Maxwell-Boltzmann distribution. For all the experimental data presented in this thesis, the fit was reasonably good. The peak electron temperature occurs at zero time delay when the pump pulse overlaps with the probe pulse

and it is shown to be greater than 1700 K, depending on the pump fluence. The two photon absorption by photogenerated carriers makes the electron temperature fluence-dependent. The photogenerated carriers are shown to lose their kinetic energy to the lattice at subsequent time delays. The "relaxation" of the kinetic energy to the steady state value occurs on a time scale of 0.5 psec.

To extract the energy relaxation time from the experimental data, a simplified set of ordinary differential equations is developed. The model includes the two-photon absorption and carrier transport into neighboring sites or into the bulk states. The calculated electron temperatures for four different pump fluences are compared with experimental data and the best-fit parameters have reasonable values. The carrier energy relaxation time has been extracted from the fit and it is determined to be 0.4 psec.

For the future research effort, it would be interesting to explore more of the early-time dynamics. For example, even though the presence of the nonthermal distribution at early time delay has been shown through this study, the thermalization time couldn't be quantitatively determined due to the finite temporal resolution of the experiment. By improving the temporal resolution of the system, the thermalization time can be determined. Its pump beam fluence dependence would be of considerable interest in the light of fundamental carrier-carrier interaction in an indirect bandgap material such as silicon.

Another interesting area to be probed would be the electron temperature dependence on the background doping. The background doping provides a pool of cold carriers with which the photogenerated carriers equilibrate within a finite amount of time. To perform this experiment, the system has to be able to detect minute changes in the

electronic temperature, which necessitates the improvement of the resolution of the electron spectrometer. It also requires establishing a better way of determining the position of the bulk band edge states.

References

[1] For discussions of hot electron effects in the device , see M.V. Fischetti, S.E. Laux and D.J. DiMaria, *Applied Surface Science,* **39** , 578 (1989)

[2] M. V. Fischetti, and S. E. Laux, *Physical Review*, **B38**, 9721 (1988)

[3] C. M. Hu, S. C. Tam, F. C. Hsu, P. K. Ko, T. Y. Chan, and K. W. Terill, *IEEE Transactions on Electronic Devices*, **ED-32**, 375 (1985)

[4] J.A. Prybyla, H.W.K. Tom and G.D. Aumiller, *Physics Review Letters*, **68**, 503 (1992)

[5] L. Struck, L. J. Richter, S. A. Buntin, R.. R. Cavanagh, J. C. Stephenson, *Physical Review Letters*, 77, 4576 (1996)

[6] C. Trappe, M. Schuetze, M. Raff, R. Hannot and H. Kurz, *Fresenius Journal of Analytic Chemistry*, **346**, 368 (1993)

[7] N.C. Tien, S. Jeong, L.M. Phinney, K. Fushinobu and J. Bokor, *Appllied Physics Letters*, **68**, 197 (1996)

[8] *Semiconductors probed by Ultrafast Laser Spectroscopy* , edited by R. R. Alfano, Orlando , Academic Press, 1984.

[9] J. Bokor, R. Haight, R. H. Storz, and J. Stark, *Physical Review* **B32,** 3669 (1985)

[10] *Modern Techniques of Surface Science* , D. P. Woodruff and T. A. Delchar, 2nd ed. Cambridge ; New York : Cambridge University Press, 1994.

[11] *Physics of Semiconductor Devices*, 2nd Edition, S. M. Sze, John Wiley & Sons, New York, 1981

[12] R. Haight, and J. A. Silberman, *IEEE Journal of Quantum Electronics*, **QE-25** , 2556 (1989)

[13] M. Bensoussan and J.M. Moison, *Physical Review*, **B27**, 5192 (1983)

[14] T.L.F. Leung, H. M. van Driel, *Applied Physics Letters*, **45** , 683(1984)

[15] J.P. Long, R.T. Williams, J.C. Rife, M.N. Kabler, in *Energy Beam-Solid Interactions and Transient Thermal Processing*, edited by D. K. Biegelsen, G. A. Rozgonyi, and C. V. Shank, MRS Symposia Proceedings No. 35 (Materials Research Society, Pittsburgh, 1985), p81

[16] N.J. Halas and J. Bokor, *Physical Review Letters*, **62**, 1679 (1989)

[17] M.W. Rowe, H. Liu, G.P. Williams, Jr. and R.T. Williams, *Physical Review* **B47**, 2048 (1993)

[18] J.R. Goldman and J.A. Prybyla, *Physical Review Letters*, **72**, 1364 (1994)

[19] C. V. Shank, R. Yen, and C. Hirlimann, *Physical Review Letters*, **50** ,454 (1983)

[20] T. Suzuki, A. Mikami, K. Uehara, and M. Aono, *Surface Science*, **323** ,L293 (1995)

[21] M. Mauerer, I. L. Shumay, G. A. Schmitt, K. L. Kompa, U, Hofer, *Quantum Electronics and Laser Science Conference*, June 2-7, 1996, Anaheim, California, Paper QMA3.

[22] W.S. Fann , R. Storz , H. W. K. Tom , J. Bokor , *Physical Review Letters*, **68** , 2834 (1992)

[23] M. Baeumler, R. Haight, *Physical Review Letters*, **67** , 1153 (1991)

[24] R. Haight, J. A. Silberman, *Journal of Vacuum Science and Technology*, **B7**, 910 (1989)

[25] R. W. Schoenlein, J. G. Fujimoto, G. L. Eesley, T. W. Capehart, *Physical Review Letters*, **61**, 2596 (1988)

[26] C. A. Schmuttenmaer, M. Aeschlimann, H. E. Elsayed-Ali, R. J. D. Miller, D. A. Mantell, J. Cao, and Y. Gao, *Physical Review* **B50**, 8957 (1994)

[27] For the operating concept of the chirped pulse amplification system, see P. Maine, D. Strickland, P. Bado, M. Pessot, and G. Mourou, *IEEE Journal of Quantum Electronics*, **QE-24**, 398 (1988)

[28] J. A. Squier, PhD Thesis, University of Michigan, 1992

[29] D. E. Spence, P. N. Kean, W. Sibbet, *Optics Letters*, **16**, 42 (1991)

[30] K. W. Delong, D. N. Fittinghoff, R. Trebino, *IEEE Journal of Quantum Electronics*, **QE-32**, 1253 (1996)

[31] For general pulsewidth measurement technique, see *Laser Spectroscopy*, 2nd ed. , W. Demtröder, Springer, Berlin, 1996 and references therein

[32] M. G. White, R. A. Rosenberg, G. Gabor, E. D. Poliakoff, G. Thornton, S. H. Southworth, and D. A. Shirley, *Review of Scientific Instruments*, **50**, 1268 (1979)

[33] J. L. Wiza, *Nuclear Instruments and Methods*, **162** , 587 (1979)

[34] J. M. C. Thornton, and R. H. Williams, *Semiconductor Science and Technology*, 4 (1989) pp847-851

[35] D. S. Kim, private communication

[36]C. Chen, B. Wu, A. Jiang, and G. You, *Scientia Sinica* , **B28**, 235 (1985)

[37] *Quantum Electronics* , A. Yariv, 3rd Edition, John Wiley & Sons, New York, 1989

[38] *Handbook of nonlinear optical crystals* V.G. Dmitriev, G.G. Gurzadyan, D.N. Nikogosyan. Berlin ; New York : Springer-Verlag, c1991. Series title: Springer series in optical sciences ; v. 64.

[39] J. Ringling, O. Kittelmann, and F. Noack, G. Korn, and J. Squier, *Optics Letters*, **18**, 2035 (1993)

[40] *The Principles of Nonlinear Optics*, Y.R.Shen , New York, J. Wiley, 1984

[41] D. Eimerl, L. Davies, S. Velsco, E. K. Graham, A. Zalkin, *Journal of Applied Physics*, **62**, 1968 (1987)

[42] Various Schemes to match group velocities of the two beam as well as the phase velocities inside a BBO crustal has been devised. For example, see T. R. Zhang, H. R. Choo, M. C. Downer, *Applied Optics*, **29**, 3927 (1990)

[43] G. Petite, P. Agostini, R. Trainham, E. Mevel, and P. Martin, *Physical Review* **B45**, 12210 (1992)

[44] C. Girardeau-Montaut, and J. P. Girardeau-Montaut, *Physical Review* **B44** ,1409 (1991)

[45] *Fundamentals of Carrier Transport*, M. Lundstrom, Addison-Wesley Publishing Company, Reading, 1992

[46] D. Agassi, *Journal of Applied Physics*, **55**, 4376 (1984)

[47] *Introduction to Solid State Physics*, C. Kittel, 6th Ed. John Wiley & Sons, New York, 1986

[48] For example, see R. E. Schlier and H. E. Farnsworth, *Journal of Chemical Phyics* , **30**, 917 (1959)

[49] D. J. Chadi, *Journal of Vacuum Science and Technology*, **16**, 1290 (1979)

[50] F. J. Himpsel, and D. E. Easttman, *Journal of Vacuum Science and Technology* ,**16**, 1297 (1979)

[51] P. M. Gundry, R. Holtom, and V. Leverett, *Surface Science*, **43**, 647 (1974)

[52] A. Ignatiev, F. Jona, M. Debe, D. E. Johnson, S. J. Whie, and D. P. Woodruff, *Journal of Physics* **C 10**, 1109 (1977)

[53] T. D. Poppendieck, T. C. Ngoc, and M. B. Webb, *Surface Science* , **43**, 287 (1978)

[54] J. J. Lander, and J. Morrison, *Journal of Chemical Physics* **37**, 729 (1962)

[55] K. C. Pandey, in *Proceedings of the Seventeenth International Conference on the Physics of Semiconductors*, San Fransisco, 1984, edited by D. J. Chadi and W. A. Harrison (Springer-Verlag, Berlin, 1985), p55.

[56] E. Artacho and F. Yndurain, *Physical Review Letters*, **62**, 2491 (1989)

[57] R. J. Hamers, R. M. Tromp, and J. E. Demuth, *Physical Review* **B34**, pp5343 (1986)

[58] L.S.O. Johansson, R.I.G. Uhrberg, P. Martensson ,and G.V. Hansson, *Physical Review*, **B42** , 1305 (1990) ; P. Martensson, A. Cricenti and G. Hansson, *Physical Review* **B33**, 8855 (1986)

[59] M. Rohlfing, P. Krüger, and J. Pollmann, Physical Review **B52**, 1905 (1995) and references therein

[60] L.S.O. Johansson and B. Reihl, *Surface Science* **269/270** , 810 (1992)

[61] A. Samsavar, E. S. Hirschorn, F. M. Leibsle, and T. -C. Chiang, *Physical Review Letters*, 63, 2830 (1989)

[62] B. S. Swartzentruber, N. M. Kitamura, M. G. Lagally, and M. B. Webb, *Physical Review* **B47** , 13432 (1993)

[63] H.S. Karlsson , G. Chiaia , and U. O. Karlsson, *Review of Scientific Instruments*, **67** , 3610 (1996)

[64] C. A. Schmuttenmaer, C. C. Miller, J. W. Herman, J. Cao, and Y. Gao , *Chemical Physics*, **205** , 91 (1996)

[65] C. S. Wang, and B. M. Klein, *Physical Review* **B24**, 3393 (1981)

[66] P.D. Yoder, and K. Hess, *Semiconductor Science and Technology*, **9**, 852 (1994)

[67] R. J. Hamers, Ph. Avouris, and F. Bozso, *Physical Review Letters*, **59**, 2071 (1987)

[68] T.Yasuda , L. Mantese , U. Rossow , and D. E. Aspnes, *Physical Review Letters*, **74** , 3431 (1995)

[69] R. Haight, and M. Baeumler, *Physical Review* **B46**, 1543 (1992)

[70] *Physics of Semiconductors and Their Heterostructures,* J. Singh ,McGraw-Hill, New York, 1993

[71] E. H. Sin, C. K.Ong, and H. S. Tan, *Physica Status Solidi* **A85**, 199 (1984)

[72] C. Jacoboni, *Proceedings of 13th International Conference on Physics of Semiconductors*, edited by F. G. Fumi, Marves, Roma ,1976.

[73] H. M. van Driel, *Physical Review* **B35**, 8166 (1987)

[74] D. H. Reitze, T. R. Zhang , W. M. Wood , M. C. Downer , *Journal of the Optical Society of America B-Optical Physics*, **7**, 84 (1990)

[75] D. Sinitsky, F. Assaderaghi, H. Orshansky, J. Bokor, and C. Hu, *Solid-State Electronics*, **41**, 1119 (1997).

Appendix 1 : Estimate of the front surface temperature due to the accumulation of the heat.

When the pump beam is incident on the sample with an average power of 200 mW, a rise in the sample temperature is observed through the thermocouples attached onto the sample specimen plate. The observed temperature increase is approximately 10-20 K. Becuase the sample specimen is in thermal contact with the backside of the sample, the observed temperature increase is that of the sample back surface. However, due to the high thermal coductivity of the sample (c-Si) and the sample specimen plate (Mo) , the tempeature of the front surface is not expected to be appreciably different from that of the back surface. In this section, the front surface temperature due to the accumulated laser pulse deposition is estimated by sloving a simple heat diffusion equation for a sample of semi-infinite extent. Also considered is the case of a sample of finite extent and it is shown that the temperature of the back surface is almost equal to that of the front surface due to the high thermal conductivity of the sample.

The temperature distribution inside a semi-infinite sample irradiated by a pulsed laser beam can be calculated from the solution of the heat diffusion equation [1]. Assuming a Gaussian spatial and temporal profile of the laser pulse, the solution to the heat diffusion equation for a sample of semi-infinite extent with the boundary condition of no heat loss in the front surface is expressed by

$$\Delta T(r,z,t) = \int_{-\infty}^{t} dt' \frac{I_m(1-R)\alpha\kappa d^2}{2K} \exp\left[-\left(\frac{t'}{\tau}\right)^2\right] \frac{1}{4\kappa(t-t')+d^2} \exp\left[-\frac{r^2}{4\kappa(t-t')+d^2}\right]$$

$$\times\left[\exp\left[-\alpha z+\kappa\alpha^2(t-t')\right] erfc\left(\frac{-z+2\kappa\alpha(t-t')}{2\left[\kappa(t-t')\right]^{1/2}}\right) + \exp\left[\alpha z+\kappa\alpha^2(t-t')\right] erfc\left(\frac{z+2\kappa\alpha(t-t')}{2\left[\kappa(t-t')\right]^{1/2}}\right)\right]$$

I_m : maximum laser intensity

R : reflectivity of the sample

α : absorption coefficient of the sample

K : Thermal conductivity of the sample

κ : ratio of thermal conductivity to heat capacity per unit volume

d : pulse radius

τ : FWHM pulsewidth

erfc(x) : complementary error function.

It can be transformed into a nondimensional form by introducing following variables.

With $\Theta = \frac{2K\alpha\Delta T}{I_m(1-R)}$; $\theta = t/\tau$; $\gamma = \kappa\alpha^2\tau$; $\beta = \alpha z$; $\varsigma = \frac{r}{d}$; $\varepsilon = \alpha d$;

$$\Theta(\theta,\beta,\varsigma,\gamma,\varepsilon) = \int_0^{\infty} dy \frac{\varepsilon^2}{4y+\varepsilon^2} \exp\left(-\theta^2 + \frac{2y\theta}{\gamma} - \frac{y^2}{\gamma^2} - \frac{\varsigma^2\varepsilon^2}{4y+\varepsilon^2}\right)$$

$$\times\left[\exp(-\beta+y) erfc\left(\frac{-\beta+2y}{2\sqrt{y}}\right) + \exp(\beta+y) erfc\left(\frac{\beta+2y}{2\sqrt{y}}\right)\right]$$

The temperature at z = 0 and r = 0 i.e. at the center of the spot where the beam illuminates can be estimated by putting $\beta = 0$ and $\varsigma = 0$.

$$\Theta = \int_0^\infty dy \frac{2\varepsilon^2}{4y+\varepsilon^2} \exp\left(-\theta^2 + \frac{2y\theta}{\gamma} - \frac{y^2}{\gamma^2}\right) \exp(y) erfc\left(\sqrt{y}\right)$$

$$= \int_0^\infty dy \frac{2\varepsilon^2}{4y+\varepsilon^2} \exp\left(-\frac{(y-\gamma\theta)^2}{\gamma^2}\right) \exp(y) erfc\left(\sqrt{y}\right)$$

To estimate the temperature, the following parameters are provided for the experiment discussed in this thesis; $\alpha = 1000 cm^{-1}$, $K = 142\ \mathrm{W/m \cdot K}$, $\kappa = 6.86 \times 10^{-5}$, $d = 0.1\ cm$, $\tau = 0.1\ p\sec$, and I_m=7.6 x 10^{13} J/m^{2}sec. With these values, the non-dimensional parameters are calculated to be $\gamma = 6.86 \times 10^{-8}$ and $\varepsilon = 100$. Since the value of γ is so smaller than unity, the function $\exp\left(-\frac{(y-\gamma\theta)^2}{\gamma^2}\right)$ is sharply peaked around $y = \gamma\vartheta$ and it can be replaced with $\gamma\delta(\gamma\theta)$. With this substitution, the whole expression becomes

$$\Theta = \gamma \frac{2\varepsilon^2}{4\gamma\theta + \varepsilon^2} \exp(\gamma\theta) erfc\left(\sqrt{\gamma\theta}\right).$$

The temperature at the center of the beam spot is plotted in Fig A-1. It shows that the temperature at the front surface drops by more than two orders of magnitude after 0.1 msec due to the heat diffusion. Therefore, it is expected that the temperature rise due to the accumulated laser pulses does not play a major role in determining the steady-state sample temperature in a semi-infinite sample geometry.

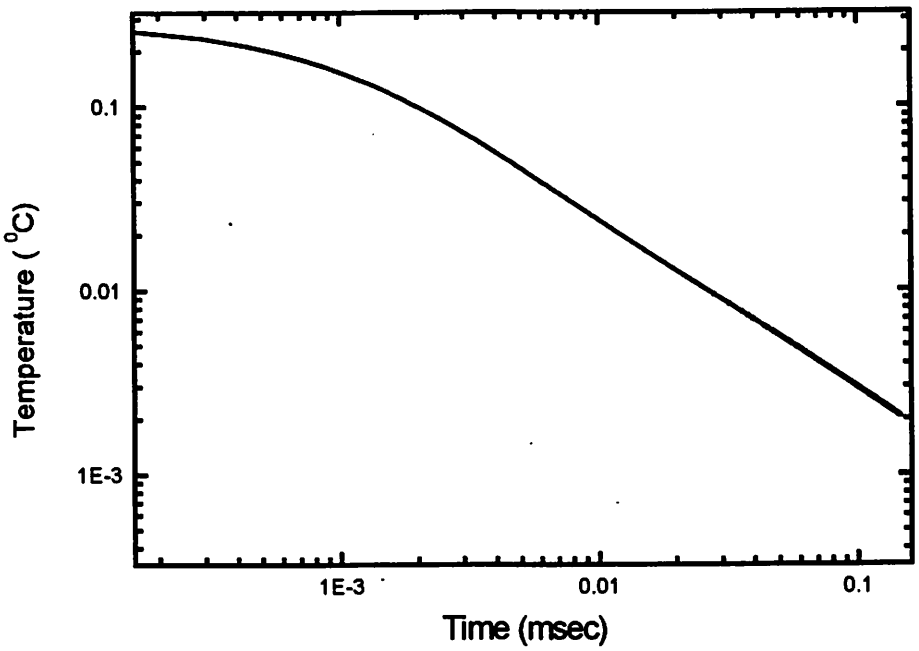

Fig A-1. The temperature variation with time at the center of the beam spot on the sample.

When a sample of finite size is considered, the temperature distribution inside the sample can be estimated by numerically solving the heat diffusion equation. The shape of the sample is assumed to be a thin disk with azimuthal symmetry. Its thickness is 0.5 mm and the radius is 5 mm. The heat diffusion equation is solved with boundary condition of no heat exchange across the boundary at each surface. The initial condition is taken in such a way that the instant temperaure rise of 1 K occurs within 10 micron from the front surface (the optical absorption depth of the laser beam) and the radius of the laser beam is taken to be 2 mm. Figure A-2 shows the temperature distribution inside the sample one second after the lease pulse illumination.

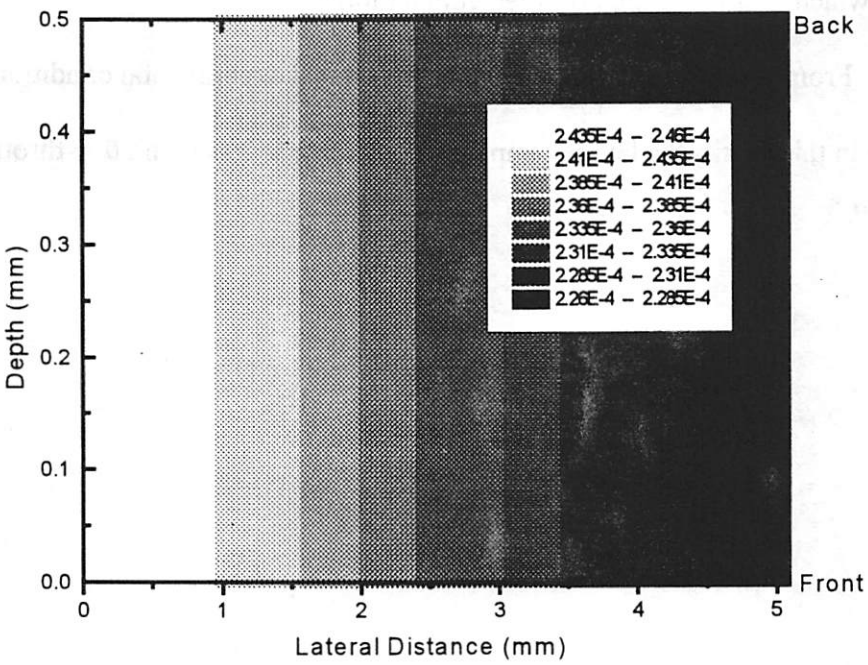

Fig. A-2. Temperature distribution in a thin-disk shaped silicon sample.

It shows that the heat generated in a localized region spreads to the sample, rasing the sample temperature to approximately 2.4×10^{-4} K. It is also shown that temperature is equlibrated throughout the sample within 10% within one second due to the high conductivity of the crystalline silicon. Therefore, it is a good assumption that the sample temperature reaches steady state within finite time, and at the steady state the temperture distribution is quite uniform throughout the sample. The observed temperature increase of 20 K is due to the accumultaed laser pulse deposition. The time it takes for the sample to reach the steady state at that temperature can be estmated by

(observed increase)/(increase per laser pulse) x (spacing between the laser pulse).

Assuming the the temperature increase per laser pulse is 0.3 K, above formula yields 270 seconds, which is close to the observed equilibration time.

From these considerations, under the typical experimental condition as described in this thesis, the lattice temperature increase is less than 20 K throughout the sample.

Appendix 2 : Calculation of the potential energy of an electron cloud of thin-disk shape

The spatial distribution of electrons generated in a pulsed laser photoemission is that of a thin-disk because the lateral dimension of the laser beam is much greater than the distance that an electron covers within the pulsewidth of the laser. To estimate the magnitude of the space charge broadening, the potential energy per electron in such a thin-disk shaped cloud can be calculated.

It is assumed that the electrons are uniformly distributed in a thin-disk with negligible thickness. The radius of the disk is taken to be R and the surface charge density is denoted as σ as shown in Fig. A-3. .

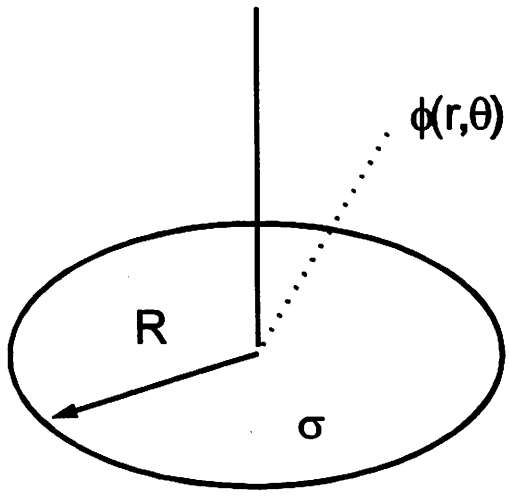

Fig. A-3 The potential distribution due to a uniform charge distribution of thin disk shape.

The potential energy of an arbitrary charge distribution can be calculated as

$$E_{pot} = \frac{1}{2}\int \rho(\vec{x})\phi(\vec{x})d^3x .$$

To calculated the potential due to the uniform charge distribution on a thin disk, the Laplace equation has to be solved. The solution to Laplace equation with azimuthal symmetry can be expressed as [2]

$$\phi(r,\theta) = \sum_{l=0}^{\infty}\left[A_l r^l + B_l r^{-l-1}\right]P_l(\cos\theta) .$$

where $P_l(x)$ is the Legendre polynomial of lth order. The coefficients A_l and B_l can be determined by matching the general solution to the known solution i.e. the potential on the z axis. The potential on the z-axis can be obtained with an elementary method ;

$$\phi(z) = \frac{1}{4\pi\varepsilon_0}\int_0^{2\pi} d\varphi \int_0^{R} \rho d\rho \frac{\sigma e}{\sqrt{\rho^2 + z^2}} = \frac{\sigma e}{2\varepsilon_0}\left(\sqrt{R^2 + z^2} - |z|\right)$$

In this section, the solution for r < R is desired. When z < R , $B_l = 0$ for l = 0,1,... for the solution to remain finite. The coefficients A_l can be determined by matching the general solution on the z-axis.

$$\phi(r = z,0) = \sum_{l=0}^{\infty} A_l z^l P_l(1) = \sum_{l=0}^{\infty} A_l z^l = \frac{\sigma e}{2\varepsilon_0}\left(\sqrt{R^2 + z^2} - |z|\right)$$

because $P_l(1) = 1$ for l = 0, 1,...

Because the right hand side only contains the even power of z except |z|, $A_l = 0$ for l = 3,5,7,... and $A_1 = -\frac{\sigma e}{2\varepsilon_0}$. To obtain the potential on the disk $\theta = \pi/2$ is substituted.

$P_l(0) = 1$ for even l and $P_l(0) = 0$ for odd l. Hence, the potential on the disk can be expressed as

$$\phi(r, \pi/2) = \frac{\sigma e}{2\varepsilon_0}\sqrt{R^2 + r^2}$$

Therefore the total potential energy is

$$E_{pot} = \frac{1}{2}\int_0^{2\pi} d\varphi \int_0^R e\sigma\, \rho d\rho \phi(\rho, \varphi) = \frac{N^2 e^2}{\pi\varepsilon_0 R}\frac{2\sqrt{2}-1}{6} = N^2 \frac{d}{R}\frac{2(2\sqrt{2}-1)}{3} = N^2 \frac{d}{R} p$$

.where p = 1.22 and d = 1.44 nm.

References for Appendices

[1] J. H. Bechtel, *Journal of Applied Physics*, **46**(4), 1585 (1975)

[2] J. D. Jackson , *Classical Electrodynamics*, 2nd Edition, McGraw-Hill Book Company, New York, 1975